RESONANTLY ENHANCED SAGNAC INTERFEROMETRY USING SURFACE PLASMON POLARITONS

by

BRIAN K. HAKE

A DISSERTATION

Presented to the Department of Physics
and the Graduate School of the University of Oregon
in partial fulfillment of the requirements
for the degree of
Doctor of Philosophy

September 2019

DISSERTATION APPROVAL PAGE

Student: Brian K. Hake

Title: Resonantly Enhanced Sagnac Interferometry Using Surface Plasmon Polaritons

This dissertation has been accepted and approved in partial fulfillment of the requirements for the Doctor of Philosophy degree in the Department of Physics by:

Dr. Benjamin McMorran	Chair
Dr. Miriam Deutsch	Advisor
Dr. Raymond Frey	Core Member
Dr. George Nazin	Institutional Representative

and

Janet Woodruff-Borden	Vice Provost and Dean of the Graduate School

Original approval signatures are on file with the University of Oregon Graduate School.

Degree awarded September 2019

DISSERTATION ABSTRACT

Brian K. Hake

Doctor of Philosophy

Department of Physics

September 2019

Title: Resonantly Enhanced Sagnac Interferometry Using Surface Plasmon Polaritons

We present a theoretical model and experimental results for a Sagnac ring interferometer resonantly enhanced via surface plasmon resonance (SPR). One defining characteristic of a resonance is the π change in phase that occurs across the resonance. For a narrow resonance, this results in a steep phase profile which proves advantageous when utilized within a phase-based detection scheme, providing a resonant enhancement that has the potential to greatly improve the sensitivity of Sagnac interferometers. Furthermore, surface plasmon resonance serves as the mechanism underlying surface plasmon sensing, one of the more commonly used techniques for detection and characterization of a variety of interfacial events. This method relies on the excitation of surface bound electromagnetic waves, known as surface plasmon polaritons (SPPs), which propagate along the interface of a metal and dielectric and exhibit a field profile that decays exponentially into both media. Excitation of SPPs within an interferometric environment provides an avenue for investigation into the potential benefits of this resonant enhancement. In addition, it carries the capacity for insight into applications of SPR sensors using interferometric techniques, some of which may be inaccessible to intensity based detection schemes.

We begin this dissertation by providing necessary background information, such as the interference equations describing the interferometer outputs and the SPP dispersion relation. We then detail the features of SPR and explore modifications to the resonance shape by variation of the system parameters. We fabricate and characterize thin silver films, suitable for supporting SPPs, to be used in sensing experiments. We design a theoretical model to compute the response of the resonantly enhanced interferometer to various perturbations and calculate the corresponding sensitivities. Finally, we construct a resonantly enhanced interferometer in the laboratory, analyze the optical data collected from both interferometer output ports, and comment on the promise of this and similar devices moving forward.

CURRICULUM VITAE

NAME OF AUTHOR: Brian K. Hake

GRADUATE AND UNDERGRADUATE SCHOOLS ATTENDED:

University of Oregon, Eugene, Oregon
Point Loma Nazarene University, San Diego, California

DEGREES AWARDED:

Doctor of Philosophy, Physics, 2019, University of Oregon
Bachelor of Science, Engineering Physics, 2011, Point Loma Nazarene University

PROFESSIONAL EXPERIENCE:

Graduate Teaching Fellow, Department of Physics, University of Oregon, Eugene, 2011-2013, 2015-2016, and 2018-2019

Graduate Research Assistant, Department of Physics, University of Oregon, Eugene, 2012-2019

Science Literacy Teaching Fellow, University of Oregon, Eugene, 2016

PUBLICATIONS:

H. Grotewohl, B. Hake, and M. Deutsch, "Intensity and phase sensitivities in metal/dielectric thin film systems exhibiting the coupling of surface plasmon and waveguide modes," Appl. Opt. **55**, 8564–8570 (2016).

ACKNOWLEDGEMENTS

I would like to start by thanking my advisor, Miriam Deutsch, for providing me with the opportunity and resources needed to perform this research and for the direction given and knowledge shared with me along the way. I would also like to thank my committee chair, Ben McMorran, for the assurance and guidance he provided to help me see this process through to completion, as well as the rest of my committee, Ray Frey and George Nazin, for their participation in this process. In addition, I would like to thank the many other professors and administrative staff with whom I have interacted, for sharing their passions and expertise and providing encouragement and assistance along the way.

I would also like to thank the students I have taken classes with or interacted with as a teaching assistant for making this a fun and enjoyable place of learning. Special thanks to my cohort of physics graduate students who were right there with me through trying graduate level coursework and to all my colleagues in the Deutsch Lab, especially Herbert Grotewohl and Andrea Goering, for the office camaraderie, the tools and information passed on to me, and the insights gleaned through helpful scientific discussions.

Thanks also are in order to my professors and fellow students from Point Loma Nazarene University for nurturing my interest in physics and preparing me for graduate school here at the University of Oregon.

I could not have accomplished this without the constant support and encouragement of countless friends and family members throughout these years. Thanks to my immediate and extended family in Phoenix, Arizona and around the globe; those from Point Loma with whom I have maintained lasting friendships;

and my faith family here at Eugene First Church of the Nazarene, among others, for providing camaraderie, welcome distractions, and for taking part in my many adventures both within and outside of physics. I could not possibly manage to list the contributions of each one individually but there are a few I would like to highlight. To the Smith-Gillespies, thank you for welcoming me as family and making the transition to life in Eugene that much easier. To the Strunks, thank you for your supportive friendship and for providing regular childcare to give me extra time to work. To my siblings; Camille, Monica, Michael, Nathan, and Jonathan; you were my first and best friends growing up and our visits together always give me something to look forward to. To my parents, you have loved and cared for me since day one and I aspire toward your example of joy, faithfulness, and humility. To Walter, you have changed my life immeasurably since your arrival into this world. It is truly an honor to be your dada and to have the privilege of watching you grow and learn; you have taught me so much already. Finally, Alison, where do I begin? You believed in me even when I expressed my doubts. You have been there with me at my best and at my worst, and you continue to love me and motivate me toward bettering myself. I am so blessed to be able to share this life with you. Thank you, and I love you.

To God be the glory.

This material is based upon work supported by the National Science Foundation under Grant Nos. ECCS-1202182 and DMR-1404676. Any opinions, findings, and conclusions or recommendations expressed in this material are those of the author and do not necessarily reflect the views of the National Science Foundation.

To my beloved grandparents, who I know are beaming with pride.

TABLE OF CONTENTS

Chapter Page

I. INTRODUCTION 1

Overview 1
Sagnac Interferometry 2
Surface Plasmon Resonance Sensors 5
Chapter Outline 7

II. SAGNAC INTERFEROMETRY 10

Overview 10
Configuration 10
Interference Equations 15
Summary 18

III. SURFACE PLASMON RESONANCE 20

Overview 20
Surface Plasmon Polariton Dispersion 20
Discussion of Materials 24
Coupling to Surface Plasmon Polaritons 27
Surface Plasmon Resonance Features 28

Chapter Page

Sample Preparation and Characterization 32

Summary 37

IV. RESONANTLY ENHANCED SAGNAC INTERFEROMETRY 39

Overview 39

Inclusion of a Resonance 40

Perturbation Detection 42

Dark Port Intensity 46

Dark Port Sensitivity 49

Bright Port Intensity 53

Bright Port Sensitivity 56

Angular Detuning 60

Summary 63

V. EXPERIMENTAL IMPLEMENTATION AND RESULTS 65

Overview 65

Configuration and Alignment 65

Perturbation Implementation 72

Reciprocal Ohmic Heating in the Bright Port 76

Nonreciprocal Plasmon Drag in the Dark Port 81

Simultaneous Detection 94

Summary 95

Chapter Page

VI. CONCLUSION 96

Future Directions 97

Closing Remarks 99

REFERENCES CITED 101

LIST OF FIGURES

Figure Page

1. The interferometer configuration used by Georges Sagnac. 3
2. Early surface plasmon sensing data. 6
3. Schematic of a Sagnac interferometer. 11
4. Schematic diagram of a field incident on an interface. 12
5. The reverse time picture of a field incident on an interface. 13
6. Illustration of the Stokes relations using time reversal invariance. 14
7. Impact of a beamsplitter split ratio imbalance. 18
8. Single interface schematic for calculation of SPP dispersion relation. . . . 22
9. Spectral permittivity of a few noble metals. 25
10. Electromagnetic field of SPPs. 26
11. Mode dispersion of SPPs. 27
12. Kretschmann configuration for coupling to SPPs. 28
13. SPR angular reflectance and phase. 29
14. SPR angular reflectance for varied silver film thicknesses. 30
15. Angular dependence of SPR phase with varied film thickness. 31
16. Schematic for angle conversion. 33
17. Angular reflectance experimental data with best fit functions. 34
18. Angular reflectance data with fit for a near-critical thickness film. 36
19. Visualization of silver film topography created from AFM data. 37
20. AFM step height analysis. 38
21. Resonantly enhanced Sagnac interferometer using SPPs. 41
22. Differential phase magnitude with variation in metal film thickness. . . . 42

Figure Page

23. SPR reflectance and phase in the refractive index domain. 43
24. Phase difference produced by a nonreciprocal perturbation. 45
25. Dark port response to nonreciprocal perturbations. 47
26. Dark port perturbation response. 48
27. Dark port response to small perturbations. 49
28. Nonreciprocal and reciprocal sensitivity in the dark port. 51
29. Dark port sensitivity for simultaneous detection. 52
30. Dark port sensitivity for supercritical thickness. 53
31. Bright port response to reciprocal perturbations. 54
32. Bright port perturbation response. 56
33. Bright port response to small perturbations. 57
34. Reciprocal and nonreciprocal sensitivity in the bright port. 58
35. Bright port sensitivity for simultaneous detection. 59
36. Bright port sensitivity for supercritical thickness. 60
37. Angle detuned bright port intensity. 61
38. Angle detuned dark port intensity. 62
39. Initial alignment of the interferometer 67
40. A symmetric configuration for alignment at the desired angle. 68
41. An asymmetric configuration for alignment at the desired angle. 69
42. Schematic of full experimental configuration. 72
43. Experimental configuration as constructed in the laboratory. 73
44. Diagram of the SPR prism mount used by L. J. Davis. 75
45. Angles of incidence used in bright port data collection. 77
46. Bright port response to reciprocal ohmic heating for θ =42.92°. 78
47. Bright port response to reciprocal ohmic heating for θ =43.12°. 80

Figure Page

48. Dark port response to nonreciprocal plasmon drag. 84

49. Dark port model of plasmon drag. 86

50. Dark port nonreciprocal response at the resonance minimum. 88

51. Dark port nonreciprocal response at an angle less than resonance. 90

52. Photo of apparatus with film oriented vertically. 91

53. Dark port response for varied current with vertically oriented film. 92

54. Scaling of modulation amplitude. 93

LIST OF TABLES

Table Page

1. Best fit parameter values from optical film characterization. 35
2. Interferometer response to reciprocal and nonreciprocal effects. 63
3. Decay constants of the dark port signal at the resonance minimum. 89
4. Decay constants for an angle less than the resonance minimum. 90

CHAPTER I

INTRODUCTION

Overview

This dissertation explores the functions and capabilities of a Sagnac ring interferometer resonantly enhanced via surface plasmon polaritons (SPPs). Both SPPs and Sagnac interferometers have undergone ample scientific investigation for their use in sensing applications. Sagnac interferometers are most ubiquitous in gyroscopes and for measurement of rotation; however, their sensing capabilities encompass a much broader class of phenomena which break the symmetry between the interferometer paths. In an effort to improve the detection limits achievable through these techniques, some within the field have begun to explore the inclusion of a resonance within the framework of this geometry with the intent to capitalize on the resonant phase behavior inherent to these systems. The second overarching topic of importance within this dissertation, surface plasmon sensing, is an established technique well suited for the investigation of interfacial phenomena across a variety of areas including biochemistry, biomedical, and environmental science applications. These sensors rely primarily on intensity-based detection techniques; however, with aspirations to lower the limit of detection, there has been increased interest within the field toward the employment of phase-based detection techniques. The efforts focused both toward resonance inclusion within the Sagnac interferometry community and concurrently toward phase based detection for surface plasmon sensing share an area of overlap and suggest that the marriage of Sagnac interferometry with surface plasmon sensing is an intersection worthy of exploration. Insights gleaned from

research in this domain have the potential to both provide insight to the broader field of resonantly enhanced Sagnac interferometry and expand upon the capabilities of traditional surface plasmon sensing techniques.

In this chapter, we provide a cursory overview of both Sagnac interferometry and surface plasmon sensors. This discussion will include aspects ranging from early historical details up to, and including, modern applications. In addition, we introduce the intention of utilizing the two in tandem which serves as the fundamental architecture employed throughout this dissertation. We begin now with further details regarding Sagnac interferometry.

Sagnac Interferometry

Interferometers come in a wide variety of shapes and sizes, but all rely on the singular phenomenon of interference. Two interfering waves are superimposed to form a resultant wave which can exhibit constructive or destructive interference depending on the alignment of the waves with respect to one another, referred to as the relative phase. In optical interferometry, the two are often electromagnetic waves which originated from the same source, were separated at a beamsplitter, and made to recombine at some later time. Studying the interference of these waves and the corresponding response to perturbations enacted upon the system allows us to glean information about the intensity or relative phase of the waves and often provides insight regarding the nature of the perturbation itself. The configuration of interest in this work is the Sagnac interferometer, distinguished by two beams which share a common path but propagate around that path in opposite directions before recombining at the same beamsplitter used to separate the paths initially.

The Sagnac interferometer bears the name of French physicist Georges Sagnac, who in the early 1900s designed experiments using a rotating interferometer, in hopes to support the existence and study the behavior of a luminiferous ether [1–3]. The original configuration used by Sagnac, shown in Figure 1, consists of a source lamp (labeled 0), a beamsplitter (J), four mirrors (M1-M4), and a photographic plate (pp') all mounted upon a rotating disc. Modern iterations of this class of interferometer may utilize a different number of mirrors in a variety of configurations or dispel with free space optics entirely and be constituted of fiber optics, but all operate under the same general set of guiding principles [4].

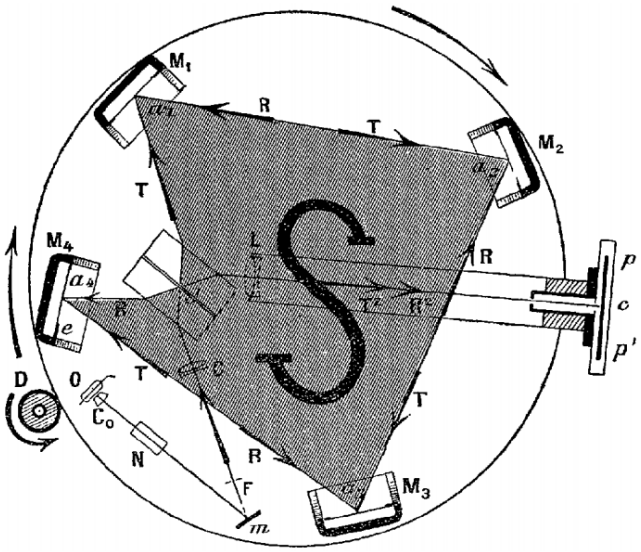

FIGURE 1. The interferometer configuration used by Georges Sagnac. As depicted in his 1913 paper published in *Comptes Rendus* [3], this configuration consists of a source lamp (labeled 0), a beamsplitter (J), four mirrors (M1-M4), and a photographic plate (pp') all mounted upon a rotating disc.

In a 1913 paper published by Sagnac[3], he related the angular rotation of the interferometer, $\vec{\Omega}$, to the fringe phase shift, $\delta\phi$, by the following equation

$$\delta\phi = \frac{8\pi\vec{\Omega}\cdot\vec{A}}{\lambda v} \tag{1.1}$$

where $\vec{A}$ is the area vector of the region enclosed by the interferometer loop, λ is the wavelength of light used, and v is the speed of light [5]. Sagnac was able to experimentally measure the expected phase shift based on the rotation of his apparatus, and used this result to argue in favor of an immobile rather than a dragging aether. Although the argument of an immobile aether eventually proved inaccurate; the results can instead be explained by the theory of relativity [6]; this relation between the phase shift and angular rotation has stood the test of time and has been termed the Sagnac effect. Furthermore, interferometers of this type, with two beams that traverse a common path in opposite directions, have come to be referred to as Sagnac interferometers. Other terms such as loop or ring interferometers are also commonplace.

The foremost advantages of this type of interferometer as compared with others such as the Mach-Zehnder or Michelson interferometer rely on the commonality of the paths. The interferometer is naturally aligned at the zero path difference fringe thereby reducing constraints on the necessary coherence length of the light source [7]. Furthermore, because both beams traverse the same path, there is an inherently reduced sensitivity to low frequency phase noise including many thermal and environmental sources [8, 9]. The elimination of numerous potential noise sources allows for improved detection of perturbations which break the symmetry of these paths. A common application of ring interferometers is their use as detectors of rotation [10–13]. As the interferometer rotates, one path travels with the rotation while the other propagates against the direction of rotation, breaking the symmetry of the optical path lengths. Other applications involve the use of this device in the study of magnetic effects [14, 15], acoustics [16, 17], temperature [18, 19], humidity [20],

biosensing [21], and gravity waves in the case of the proposed Laser Interferometer Space Antenna (LISA) [22, 23].

Sagnac interferometers which incorporate a resonance, such as that of electromagnetically induced transparency (EIT), have been posited to improve the rotational sensitivity of such an instrument by as many as five to eight orders of magnitude [24]. The types of resonances explored in pursuit of obtaining such a drastic improvement in sensitivity include atomic resonances [24–26], ring resonators [27–29], and coupled sequences of micro-resonators [30–33]. The pertinent feature here is the large differential phase found on resonance. This phase behavior allows for a detectable interferometric response to a particularly small detuning in some parameter relevant to the particular resonant system. It is this resonant enhancement of the sensitivity that we aim to exploit in this dissertation.

Surface Plasmon Resonance Sensors

A sensor is a device in which an output or measurement of the system responds to stimuli from its surrounding environment in a calculable manner. Surface sensitive sensing techniques preferentially respond to phenomena which occur in the near vicinity of an interface between two materials. One such technique utilizes surface plasmon resonance (SPR). In this technique, SPPs, coupled modes of charge-density waves and photons, are excited along the interface between a metal and dielectric and display an electromagnetic field profile which decays exponentially into both media. These surface waves exhibit subwavelength confinement of light creating increased field intensity and, thus, particularly high sensitivity to interfacial events. Detailed review articles regarding the concepts and technologies of SPR sensors have been authored by Jiří Homola [34, 35].

The use of surface plasmon resonance as an optical biosensor was first realized in the early 1980s by Claes Nylander and Bo Liedberg [36–38]. They recognized the concept as conducive to gas detection and performed an experimental investigation utilizing a gas cavity as part of the Kretschmann configuration [39]. They were successful in measuring both the shift in resonance angle, $\Delta\theta$, and the shift in reflectivity at a fixed angle of incidence, ΔR, in response to the introduction of differing concentrations of gas. Their results are shown in Figure 2. The differing gas concentrations manifest as a change in refractive index as experienced by the propagating surface plasmon, modifying the resonance. This general principle persists as the applications have expanded beyond gas concentration detection to others including film characterization [40, 41], liquid identification [42, 43], temperature sensing [44, 45], and chemical sensors [46, 47]. Additionally, techniques have expanded to encompass those using photonic crystals [48–50], fiber optics [51–53] and even interfacing with smart phones [54, 55].

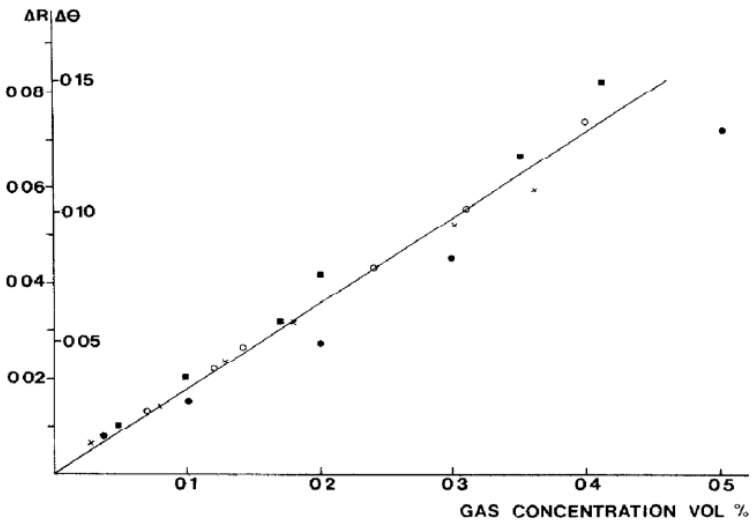

FIGURE 2. Early surface plasmon sensing data.
Published by Claes Nylander and Bo Liedberg in 1982 [36], this figure shows measurement of gas concentration as indicated by both a shift in the resonance angle, $\Delta\theta$, and a shift in reflectivity, ΔR, at a fixed angle.

In the last decade, there has been much discussion regarding the lower detection limits achievable using SPR sensors, with many of the best devices capable of detecting a refractive index changes as small as 10^{-7} RIU [56]. It has been argued that phase sensitive detection techniques have the ability to lower this limit of detection by an order of magnitude, down to 10^{-8} RIU [57–59]. Others have argued against this, stating that the drawbacks of the lower intensity at the resonance minimum, where the differential phase is maximized, outweigh the advantages of phase based detection [60]. One potential method of combating this counterpoint is through the use of a stacked metal and dielectric layer configuration, which creates a geometric Fano resonance, and alters the reflectance and phase profiles [61–64]. This allows for increased intensity in regions with significant phase change, thus minimizing concerns regarding detection noise. This work utilizes an interferometric surface plasmon sensing technique, contributing to the knowledge base regarding the capabilities of phase based probes.

Chapter Outline

This dissertation will explore the integration of surface plasmon sensing techniques within the construct of a Sagnac interferometer as a means of improved sensing capabilities and resonant enhancement of the sensitivity.

The second chapter will focus entirely on Sagnac interferometry and delve into some of the mathematical formalism. The optical components which comprise the interferometer and the general configuration in which they will be used will be introduced with particular attention given to the beamsplitter. As a part of this chapter, we will present the interference equations describing the normalized intensity

at the interferometer outputs. These equations will act as a foundational building block upon which much of the remaining discussion will be based.

The focus of this dissertation will then shift back to surface plasmon resonance in the third chapter. This chapter will include a derivation of the surface plasmon dispersion relation for wave propagation along the interface of two semi-infinite media. A discussion of the parameters necessary to satisfy this equation will follow, along with proposed materials that fit these requirements. Next, we will address coupling schemes for excitation of surface plasmons and introduce the configuration used for these experiments. Some features of the resulting resonance, and their importance to sensing techniques, will be highlighted. Finally, the chapter will conclude with experimental details regarding both the preparation of samples as well as the optical interrogation techniques utilized to characterize them.

The fourth chapter describes the theoretical model used and the results obtained by employing it. We begin with some logistical details regarding the model and methods for calculation of the outputs. We identify and differentiate two distinct types of perturbations, reciprocal and nonreciprocal, and delve into the response at both interferometer outputs to reciprocal perturbations, nonreciprocal perturbations, and the simultaneous existence of both. Included in this chapter is an examination of the sensitivity at each output and how well the results withstand variation to parameters of the system. The results of this investigation are summarized; highlighted by the observation that, unlike a typical Sagnac, the resonantly enhanced interferometer is in fact sensitive to reciprocal effects. This unlocks the potential for simultaneous detection of both reciprocal and nonreciprocal perturbations through use of a single source beam and monitoring of the two output channels.

In the fifth chapter, we will document the construction of the optical system while describing the components used and the procedures for alignment. We will then discuss the experimental implementation of both reciprocal and nonreciprocal effects by introduction of an electrical current to the metal film of the surface plasmon configuration. This will introduce ohmic heating as the reciprocal perturbation and plasmon drag as the nonreciprocal perturbation. Data collected from both outputs of the interferometer will be presented and discussed in attempt to support the expected outcomes based on the theoretical modeling contained in chapter four. A few comments on simultaneous detection will conclude this chapter.

The final chapter will highlight the conclusions drawn from this dissertation as well as present additional avenues for further exploration and closing remarks.

CHAPTER II

SAGNAC INTERFEROMETRY

Overview

In this chapter we take a more detailed and mathematical approach to Sagnac interferometry. We begin by presenting the generic configuration used in this dissertation and discussing the components used, with particular attention to the beamsplitter. We then derive the interference equations that describe the normalized intensity at the outputs of the interferometer and simplify them with use of the Stokes relations. Finally, we introduce a beamsplitter imbalance parameter and explore the effects of an uneven split ratio on the outputs.

Configuration

A Sagnac interferometer is the name given a closed loop interferometer consisting of two counterpropagating beams which traverse a common path. The commonality of the paths yields increased stability to laser fluctuations, environmental noise, or other noise sources which affect both paths equivalently. Consequently, this type of interferometer has proven useful in detection of non-reciprocal phenomena which break the inherent symmetry of the two paths. This detection is primarily done via a single output of the interferometer; however, there exists another interferometer output directed back along the input beam path. In this work, we explore the response of both interferometer outputs in search of any additional information that may be gleaned through observation of both output ports. We begin that discussion by describing the particular configuration used in this dissertation and

working through the mathematical formalism which describes the intensity at the interferometer outputs.

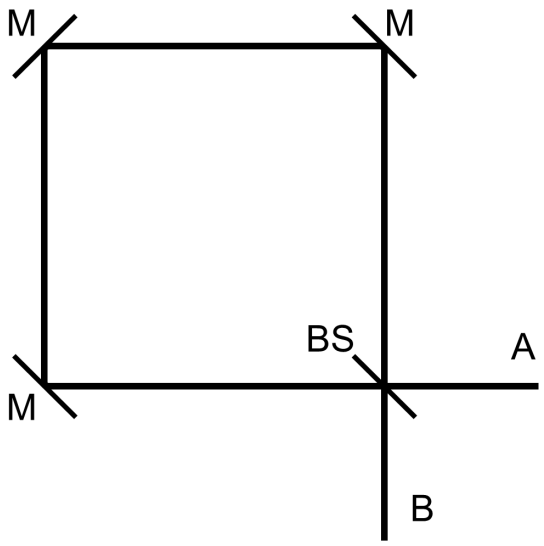

FIGURE 3. Schematic of a Sagnac interferometer.
This Sagnac configuration consists of a beamsplitter (BS) and three mirrors (M). The locations marked A and B act as both inputs and outputs of the system.

A schematic of the basic Sagnac interferometer configuration that will be discussed in this dissertation is portrayed in Figure 3. This type of interferometer consists of a single beamsplitter and two or more mirrors, three in the case of this work. For an input laser beam incident at A as marked in the figure, the outputs exit the interferometer at the locations marked A and B. In a perfectly balanced interferometer, with equivalent phase accumulation in the two paths, the output that exits the beamsplitter at the laser input exhibits perfectly constructive interference. In this same scenario, the complementary interferometer output displays destructive interference. Furthermore, assuming an ideal 50/50 reflection/transmission split at the beamsplitter, the signal at the destructive interference output is identically zero. These two outputs, which exhibit constructive and destructive interference, will

henceforth be referred to in this dissertation as the bright and dark interferometer output ports, respectively. Although the nature of the interference at each output is subject to change with the introduction of a phase difference to the propagating beams, the naming convention will continue to refer to that of the balanced interferometer configuration.

Beamsplitter

The lynchpin of the entire interferometer configuration is the beamsplitter itself. This component acts both to split the optical source into two beams and to recombine them, thereby producing the wave interference. As we will soon see in working out the full interference equations, the beamsplitter will introduce multiple reflection and transmission coefficients as the beam navigates the interferometer. The Stokes relations will help to simplify the resulting terms and elucidate the interpretation of the interferometer output equations. These Stokes relations follow from time reversal invariance of electromagnetism in non-absorbing partial reflectors, such as the beamsplitter used in the Sagnac interferometer.

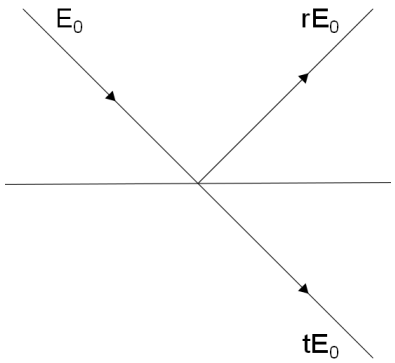

FIGURE 4. Schematic diagram of a field incident on an interface.
The incident field is partially reflected and partially transmitted with coefficients of reflection and transmission labeled r and t, respectively.

In the forward time picture, shown in Figure 4, an incident field results in both a transmitted and reflected field, with coefficients of reflection and transmission denoted here by r and t, respectively. In the time reversed picture of this scenario, in which phase conjugation has reversed the direction of propagation, the reflected and transmitted fields are now incident upon the interface. In order to satisfy time reversal invariance, the resulting outgoing fields must be both the time reversed counterpart of the above incident field as well as a null field. This time reversed scenario is diagrammed in Figure 5.

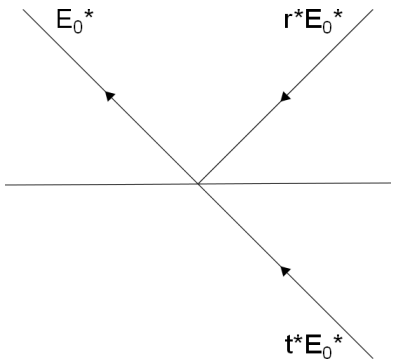

FIGURE 5. The reverse time picture of a field incident on an interface. Here the time reversed counterparts of the reflected and transmitted fields from above are incident onto the interface. For time reversal invariance to be satisfied, the resulting field must be the time reversed counterpart of the original incident field.

But for any field impingent upon an interface, we can write the reflected and transmitted components of that field in terms of the coefficients of reflection and transmission. This, then, also applies to the time reversed reflected and transmitted fields: when incident on the surface, each results in their own transmitted and reflected fields. The time reversed form of the reflected field results in transmitted and reflected fields as illustrated in the leftmost diagram of Figure 6. Similarly, the time reversed form of the transmitted field has its own reflected and transmitted fields as shown in the middle diagram of Figure 6. These field reflection and transmission coefficients,

r' and t', are denoted with a prime as they are incident from below and presumably may differ from r and t associated with incidence from above. When these resulting fields are added together, as is depicted in Figure 6, they should recover the time reversed picture of Figure 5.

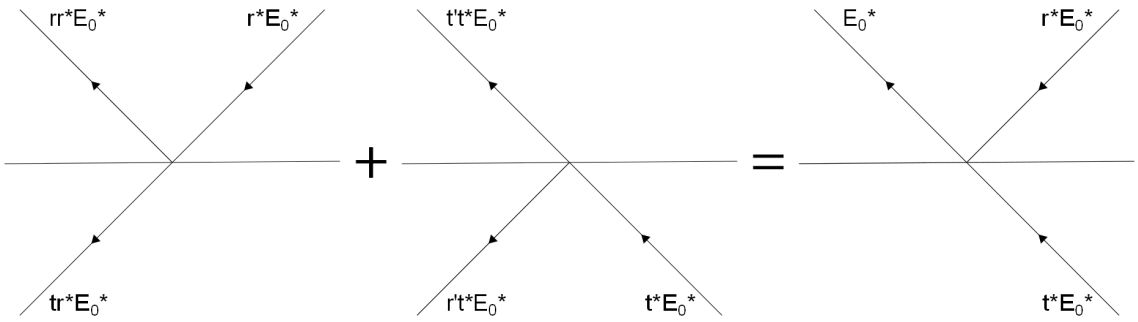

FIGURE 6. Illustration of the Stokes relations using time reversal invariance. The time reversed counterparts of the original reflected and transmitted fields, each with their own partial reflections and transmissions. These two diagrams, when combined, must recover the time reversed incident field and a complementary null field in order to satisfy the requirement of time reversal invariance. The equations resulting from the outgoing fields of each diagram uncover the Stokes relations.

With this in mind, we can now write two equations that must hold: the first coming from the outgoing fields in the upper-left quadrant of each diagram and the second coming from the outgoing fields in the lower-left.

$$rr^* E_0^* + t't^* E_0^* = E_0^* \tag{2.1}$$

$$tr^* E_0^* + r't^* E_0^* = 0 \tag{2.2}$$

leading to the familiar Stokes relations

$$rr^* + t't^* = 1 \tag{2.3}$$

$$tr^* + r't^* = 0 \tag{2.4}$$

With these tools and the overall configuration laid out, we are now equipped to derive the interference equations which describe the bright and dark outputs of the Sagnac interferometer.

Interference Equations

The normalized output intensities of the bright and dark ports can be calculated by keeping track of the electric field as it propagates around the interferometer. To calculate the output intensities at A and B, first suppose an input field of $E_0 e^{i\phi_0}$ impingent upon the beamsplitter. The corresponding transmitted and reflected fields travel opposite directions around the interferometer. Upon again reaching the beamsplitter they will have accumulated additional phase ϕ_1 and ϕ_2 respectively and their amplitude will be modified by the factor $\sqrt{T_1}$ and $\sqrt{T_2}$ respectively where T_1 and T_2 are the round trip intensity coefficients for the two paths. The transmitted field is incident again on the same face of the beamsplitter, resulting in the terms $rt\sqrt{T_1}E_0 e^{i(\phi_0+\phi_1)}$ and $tt\sqrt{T_1}E_0 e^{i(\phi_0+\phi_1)}$. Upon return to the beamsplitter the reflected field is incident on the opposite face resulting in the terms $t'r\sqrt{T_2}E_0 e^{i(\phi_0+\phi_2)}$ and $r'r\sqrt{T_2}E_0 e^{i(\phi_0+\phi_2)}$, where the prime denotes incidence from the opposite face of the beamsplitter. By superposition, the field at the bright output port is as follows.

$$E_+ = E_0 e^{i\phi_0}\left(rt\sqrt{T_1}e^{i\phi_1} + t'r\sqrt{T_2}e^{i\phi_2}\right) \tag{2.5}$$

Similarly, addition of the fields in the complementary port results in the following equation for the field at the dark output port of the interferometer.

$$E_- = E_0 e^{i\phi_0}\left(tt\sqrt{T_1}e^{i\phi_1} + r'r\sqrt{T_2}e^{i\phi_2}\right) \tag{2.6}$$

Since intensity is proportional to $|E|^2$ the normalized output intensity at the bright port can be drawn from the electric field equation at that output.

$$I_+ = I_0|rt\sqrt{T_1}e^{i\phi_1} + t'r\sqrt{T_2}e^{i\phi_2}|^2 \tag{2.7}$$

where $I_0 = |E_0 e^{i\phi_0}|^2$. Or equivalently,

$$I_+ = I_0\left[|r|^2|t|^2T_1 + |t'|^2|r|^2T_2 + \sqrt{T_1T_2}|r|^2\left(t^*t'e^{i(\phi_2-\phi_1)} + t'^*te^{-i(\phi_2-\phi_1)}\right)\right] \tag{2.8}$$

Making use of the stokes relation, $rr^* + t't^* = 1$, the resulting intensity may be written as

$$I_+ = I_0\left[|r|^2|t|^2T_1 + |t'|^2|r|^2T_2 + 2\sqrt{T_1T_2}|r|^2\left(1 - |r|^2\right)cos\left(\phi_2 - \phi_1\right)\right] \tag{2.9}$$

In the same manner, the intensity at the dark output port may be computed using the respective field equation.

$$I_- = I_0|tt\sqrt{T_1}e^{i\phi_1} + r'r\sqrt{T_2}e^{i\phi_2}|^2 \tag{2.10}$$

Which may be equivalently expressed as

$$I_- = I_0\left[|t|^4T_1 + |r'|^2|r|^2T_2 + \sqrt{T_1T_2}\left(t^*t^*r're^{i(\phi_2-\phi_1)} + r'^*r^*tte^{-i(\phi_2-\phi_1)}\right)\right] \tag{2.11}$$

Then, by applying a second stokes relation, $tr^* + r't^* = 0$, the dark port intensity can be written as

$$I_- = I_0\left[|t|^4T_1 + |r'|^2|r|^2T_2 - 2\sqrt{T_1T_2}|t|^2|r|^2cos\left(\phi_2 - \phi_1\right)\right] \tag{2.12}$$

As a sanity check, we first assume the round trip transmission coefficients and phase accumulation are equivalent for both directions of travel around the loop, meaning $T_1 = T_2$ and $\phi_1 = \phi_2$. We further assume the beamsplitter maintains an ideal 50/50 split ratio for incidence from both sides, such that $|r|^2 = |r'|^2 = |t|^2 = |t'|^2 = \frac{1}{2}$. Under this scenario, the bright port intensity reduces to $I_+ = TI_0$ and the dark port intensity goes to zero, displaying complete constructive and destructive interference, respectively.

Split Ratio Imbalance

In practical applications, the transmission coefficient may depend on the direction the beam travels around the path, and the beamsplitter may not provide an ideal 50/50 split. A directionally dependent transmission coefficient can be accounted for by a difference in T_1 and T_2, which are not required to be equivalent. To describe how an uneven beamsplitter may modify the output intensities, a split ratio imbalance parameter, ε, can be defined such that

$$|r|^2 = |r'|^2 = \frac{1}{2}(1+\varepsilon) \tag{2.13}$$

$$|t|^2 = |t'|^2 = \frac{1}{2}(1-\varepsilon) \tag{2.14}$$

Written in terms of this parameter, the normalized intensity outputs at the bright and dark ports are as follows

$$I_+ = \frac{1}{4}I_0\left(1-\varepsilon^2\right)\left[T_1 + T_2 + 2\sqrt{T_1T_2}cos\left(\phi_2 - \phi_1\right)\right] \tag{2.15}$$

$$I_- = \frac{1}{4}I_0\left[\left(1-\varepsilon\right)^2 T_1 + \left(1+\varepsilon\right)^2 T_2 - 2\left(1-\varepsilon^2\right)\sqrt{T_1T_2}cos\left(\phi_2 - \phi_1\right)\right] \tag{2.16}$$

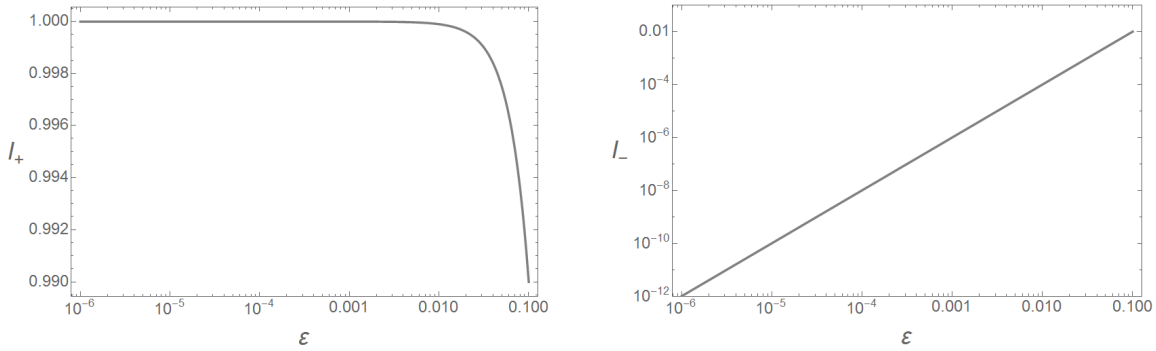

(a) Bright port.

(b) Dark port.

FIGURE 7. Impact of a beamsplitter split ratio imbalance.
Bright and dark port normalized output intensities as a function of ε for an interferometer with $T_1 = T_2$ and $\phi_1 - \phi_2 = 0$; ε of 0.1 represents a 55/45 split ratio.

The normalized output intensities as a function of ε for an interferometer with $T_1 = T_2$ and $\phi_1 - \phi_2 = 0$ are shown in Figure 7. From this, we can see that for ε up to 0.1, which represents a 55/45 split ratio, the normalized intensities vary by up to 0.01. This is not too significant a concern with respect to the bright port, where this variation is riding atop a large magnitude signal to begin with. However, in the dark port this is not the case. Using a laser line, non-polarizing beamsplitter optimized for 632.8 nm we expect to measure a value of ε below 0.1; how far below will set a limit on the lowest intensity theoretically achievable at the dark port of our interferometer.

Summary

This chapter provided further background information regarding Sagnac interferometry that will be utilized throughout the remainder of this dissertation. We first presented the basic Sagnac configuration that will be further expanded upon later on in this dissertation, but that serves as an informative starting point. Next, we derived the interference equations which characterize the intensity outputs of the interferometer. These will prove useful in the theoretical modeling contained within

the following chapters. Lastly, we introduced a split ratio imbalance parameter to explore the impact of an imbalanced beamsplitter. With an introductory discussion of Sagnac interferometry complete, we now shift gears and focus our attention on the concept of surface plasmon resonance.

CHAPTER III

SURFACE PLASMON RESONANCE

Overview

This chapter contains theoretical background information and experimental outcomes regarding the concept of surface plasmon resonance (SPR), as a detailed understanding of this phenomenon is vital before moving forward to incorporate it within the Sagnac geometry. We begin with a conceptual description of SPR and accompanying surface plasmon polaritons (SPPs). We then exploit Maxwell's equations of electromagnetism to arrive at the surface plasmon dispersion relation. Next, we consider the requirements that must be satisfied by the material parameters involved in this equation and explore some suitable materials for doing so. Armed with this knowledge, we introduce a configuration of these materials that allows for coupling to the surface plasmon mode. Furthermore, we explore the features of the resonance and the tunability of the resonance shape through variation of material parameters. Lastly, we detail experimental techniques for creation, optical interrogation, and independent characterization of samples exhibiting these resonance features.

Surface Plasmon Polariton Dispersion

SPR spectroscopy is a popular surface-sensitive characterization technique which provides a repeatable and quantifiable optical response to some interfacial event. This may include the binding of proteins to the surface, a change in temperature of the one of the constituent materials, or the presence of a biomarker within a biological

sample, among other stimuli [46]. This technique is facilitated by the existence of coherent electron oscillations known as surface plasmons. The oscillations may be localized to a small particle or propagate along an interface. The latter, also known as SPPs, are coupled modes of charge density waves and photons that propagate along the boundary between metal and dielectric materials. They are characterized by an electromagnetic field profile that peaks sharply at the interface and decays exponentially away from the interface. In order to gain a more mathematical understanding of the propagation of SPPs it is instructive to uncover the dispersion relation.

The dispersion relation for SPPs can be found by application of Maxwell's equations. To solve, consider an interface between two semi-infinite media and begin with an electric field of the following form that propagates along the interface, here designated as the x axis, and decays exponentially into the two media, along the z direction.

$$\overrightarrow{E} = \begin{cases} (\hat{x}E_{1x} + \hat{z}E_{1z})\, e^{ik_{\parallel}x - k_1 z - i\omega t} & z > 0 \\ (\hat{x}E_{2x} + \hat{z}E_{2z})\, e^{ik_{\parallel}x + k_2 z - i\omega t} & z < 0 \end{cases} \tag{3.1}$$

Where subscripts 1 and 2 refer to the materials above and below the x axis according to the schematic shown in Figure 8; E_x and E_z are the field amplitude coefficients in the x and z directions; $k_{\parallel}$ is the wave vector along the direction of propagation; k_1 and k_2 are the decay coefficients into the two materials, both taken to be positive; and ω is the frequency of the wave. We first impose boundary conditions, namely that the component of the electric field parallel to the interface, E_x, must be continuous across the surface $z = 0$. In doing so, we can relate the amplitude coefficients in the following manner.

$$E_{1x} = E_{2x} \tag{3.2}$$

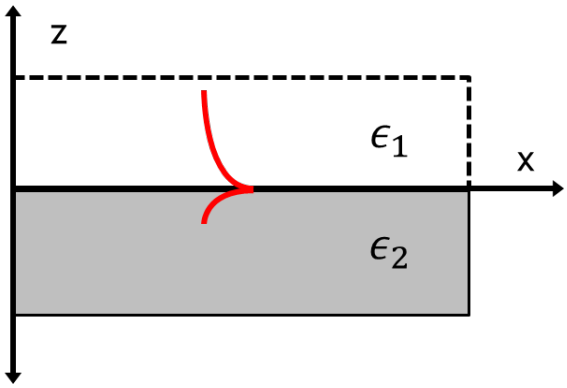

FIGURE 8. Single interface schematic for calculation of SPP dispersion relation. Orientation of axes is as shown and ϵ_1 and ϵ_2 represent the permittivities of the materials used. The curved lines at the interface are meant to evoke the exponential decay of electric field into the two media.

Secondly, in the absence of surface charge, we apply the boundary condition that the component of the electric displacement perpendicular to the interface, D_z, must also be continuous across the surface $z = 0$. Doing so gives a similar relation,

$$\epsilon_1 E_{1z} = \epsilon_2 E_{2z} \tag{3.3}$$

where ϵ_1 and ϵ_2 are the relative permittivities of the material. Then, apply Maxwell's equation for the electric displacement, first by taking the divergence as follows

$$\vec{\nabla} \cdot \vec{D} = \begin{cases} \epsilon_1 \left(ik_{\parallel} E_{1x} - k_1 E_{1z} \right) e^{ik_{\parallel} x - k_1 z - i\omega t} & z > 0 \\ \epsilon_2 \left(ik_{\parallel} E_{2x} + k_2 E_{2z} \right) e^{ik_{\parallel} x + k_2 z - i\omega t} & z < 0 \end{cases} \tag{3.4}$$

In the absence of a source term, the divergence of the electric displacement is equal to zero. By imposing this condition, we arrive at the following two equations.

$$ik_{\parallel}E_{1x} - k_1E_{1z} = 0 \tag{3.5}$$

$$ik_{\parallel}E_{2x} + k_2E_{2z} = 0 \tag{3.6}$$

Combining these with Equations 3.2 and 3.3 results in the statement below.

$$k_1\epsilon_2 + k_2\epsilon_1 = 0 \tag{3.7}$$

Based on the condition that k_1 and k_2 are assumed positive, this requires that ϵ change sign across the interface. As will be discussed in more detail later on, this can be accomplished if one of the materials is a metal. Here, we will take the first medium to be a typical dielectric material with $\epsilon_1 > 0$ and the second to be a metal with negative permittivity, $\epsilon_2 < 0$.

To arrive at the dispersion relation for SPPs, we begin with the wave equation

$$\overrightarrow{\nabla}^2\overrightarrow{E} - \frac{\mu\epsilon}{c^2}\frac{\partial^2}{\partial t^2}\overrightarrow{E} = 0 \tag{3.8}$$

and apply it to Equation 3.1, which yields the following two equations.

$$-k_{\parallel}^2 + k_1^2 + \frac{\epsilon_1}{c^2}\omega^2 = 0 \tag{3.9}$$

$$-k_{\parallel}^2 + k_2^2 + \frac{\epsilon_2}{c^2}\omega^2 = 0 \tag{3.10}$$

These may be combined with Equation 3.7 to obtain the surface plasmon dispersion relation

$$k_{\parallel} = \frac{\omega}{c}\sqrt{\frac{\epsilon_1\epsilon_2}{\epsilon_1+\epsilon_2}} \tag{3.11}$$

Although this relation looks linear in ω, there is a frequency dependence of ϵ_2 which makes the relationship nonlinear. Additionally, the lossy nature of metals give a complex permittivity, ϵ_2, which will be accounted for here by a complex wave vector, $k_{\parallel}$. Assuming ω and ϵ_1 real, and using $\epsilon_2 = \epsilon_2^{'} + i\epsilon_2^{''}$ where $|\epsilon_2^{'}| > \epsilon_2^{''}$ the real and imaginary components of the wave vector can be written, to lowest order, as

$$k_{\parallel}^{'} = \frac{\omega}{c}\sqrt{\frac{\epsilon_1\epsilon_2^{'}}{\epsilon_1+\epsilon_2^{'}}} \tag{3.12}$$

$$k_{\parallel}^{''} = \frac{\omega}{c}\left(\frac{\epsilon_1\epsilon_2^{'}}{\epsilon_1+\epsilon_2^{'}}\right)^{3/2}\frac{\epsilon_2^{''}}{2\left(\epsilon_2^{'}\right)^2} \tag{3.13}$$

Recalling that the second material is chosen to be a metal with $\epsilon_2^{'} < 0$, here we see that in order to arrive at a real solution for $k_{\parallel}^{'}$ we further require that $|\epsilon_2^{'}| > \epsilon_1$. The imaginary component of the wave vector, $k_{\parallel}^{''}$, describes the absorption of the propagating wave and determines the SPP propagation length. The field penetration depths into the respective materials are set by k_1 and k_2 which can be solved from Equations 3.9 and 3.10.

Discussion of Materials

All of the necessary requirements for ϵ_2 are satisfied by a number of metals such as silver, gold, and aluminum, leading to their recurring use in plasmonics applications. Each have a negative permittivity across a wide spread of wavelengths from the ultraviolet through the infrared as can be seen in Figure 9a, which uses Palik data

to interpolate the permittivity as a function of wavelength [65]. The magnitude of the permittivity is large enough to satisfy the requirement that $|\epsilon_2^{'}| > \epsilon_1$ for many gases and liquids that may be used as the dielectric material ϵ_1. In addition, the imaginary components, also interpolated from Palik data and displayed in Figure 9b, are small enough to satisfy the condition $|\epsilon_2^{'}| > \epsilon_2^{''}$. Of the metals pictured, silver is the least lossy and therefore will provide the narrowest resonance. A narrower resonance results in a higher sensitivity and it is for this reason that silver is the metallic material of choice for all experiments discussed throughout this dissertation. However, this choice of silver is not without drawbacks; the greatest being the propensity for oxidation when exposed to ambient conditions, thus altering the material properties and degrading the quality of the resonance [66–68]. This effect can be mitigated, in part, by either applying a protective coating layer such as gold [69, 70] or oxide layers [71] atop the silver or by controlling the environment to which the surface of the film is exposed.

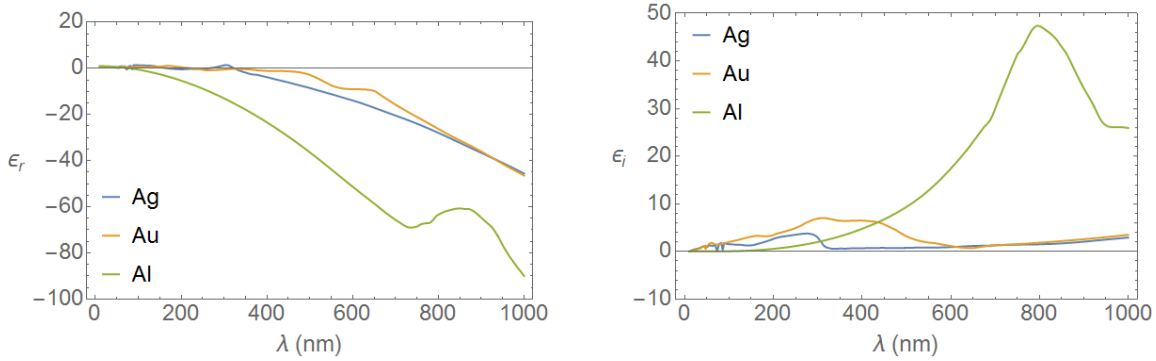

(a) (b)

FIGURE 9. Spectral permittivity of a few noble metals.
Real and imaginary components of the complex relative permittivity as a function of wavelength for silver (Ag), gold (Au), and aluminum (Al). Curves are interpolated using optical data from Palik [65].

For the experiments presented in chapter five of this dissertation, the dielectric used adjacent to the silver will be room temperature air. To prevent oxidation, the

samples will be stored under nitrogen until ready for use. Using the configuration of Figure 8 with air and silver, the field distribution of the SPP is shown in Figure 10a. Here the magnetic field is plotted as it is transverse to the direction of propagation and creates a more helpful visualization. This figure also illustrates the SPP wavelength which is very near, but slightly less than, the free space wavelength of 632.8 nm, as expected [72]. The approximate penetration depth of the field into the two media is observed more clearly by plotting the field amplitude, as is shown in Figure 10b. For this particular configuration, the 1/e optical penetration depths are found to be 400nm and 24 nm, respectively. It is this region, where the field is strongest, that will be probed be the surface plasmon sensing techniques.

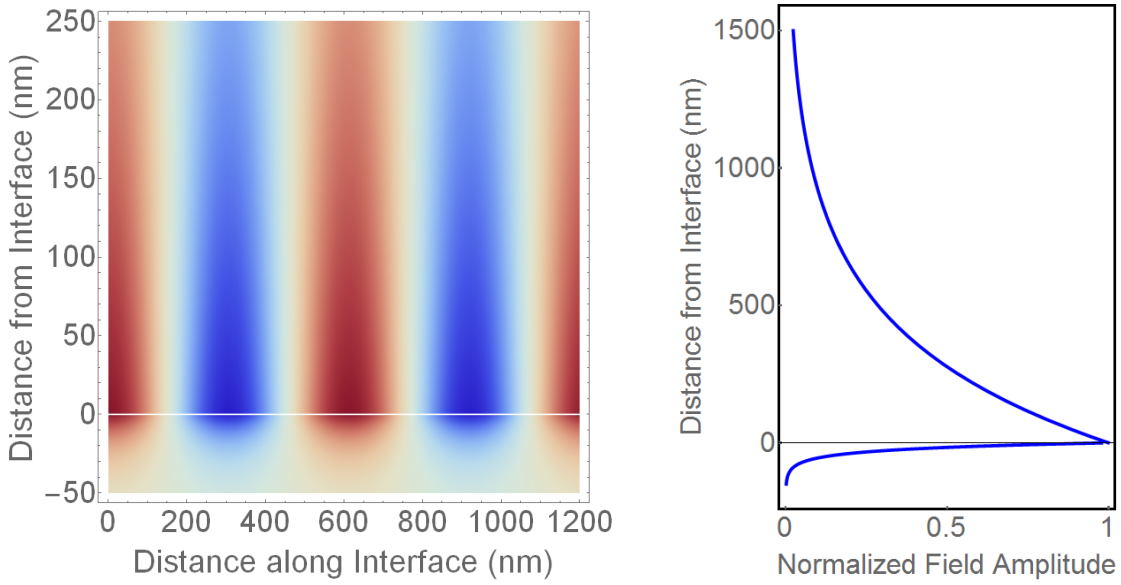

(a) (b)

FIGURE 10. Electromagnetic field of SPPs.
(a) SPP magnetic field for the configuration shown in Figure 8 with air and silver as the two materials and for wavelength of 632.8 nm. Magnetic, rather than electric field is shown because it is transverse to the propagation. (b) Normalized electromagnetic field amplitude as a function of the distance for the same configuration. This illustrates the exponential decay of the field away from the surface; 1/e optical penetration depths into the dielectric and metal are found to be 400nm and 24 nm, respectively.

Coupling to Surface Plasmon Polaritons

In order to utilize propagating surface plasmons for sensing applications, the issue of exciting SPPs must first be resolved. The difficultly lies in the fact that the SPP mode is inaccessible by light incident from the dielectric itself. For a given frequency, the wave vector of the light in the dielectric medium must be increased by some amount, Δk in order to match that of the SPP. This can be seen in Figure 11 which plots the SPP dispersion relation for a silver/vacuum interface along with the light line in vacuum; notice that the SPP mode lies entirely to the right of the light line, and thus cannot be coupled to directly from vacuum.

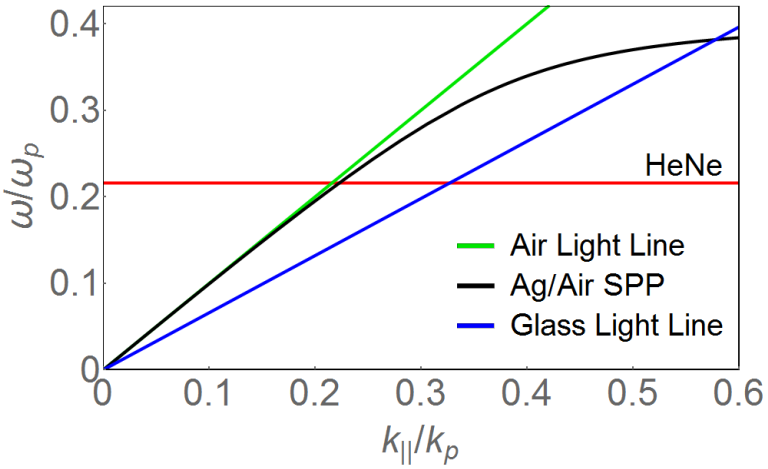

FIGURE 11. Mode dispersion of SPPs.
Dispersion relation of SPPs at an Ag/vacuum interface and light lines in both vacuum and glass to show that use of a glass prism enables coupling to SPPs. Frequencies are normalized to the plasma frequency, ω_p, and the real part of $k_{||}$ is plotted after normalization to $k_p = \omega_p/c$. The HeNe frequency, the frequency used in the calculation of the SPP dispersion, is indicated in the figure as a reference.

To excite SPPs, the momentum mismatch must be overcome through some coupling scheme. This can be accomplished via grating coupling, in which the higher order diffracting beams compensate the additional momentum, or attenuated total reflection, also termed prism coupling [73]. In this dissertation we focus on

the coupling scheme of attenuated total reflection, which involves use of a prism of higher index material than the SPP dielectric in order to shift the light line to higher wave vector – further to the right as seen in Figure 11. From the prism, the SPP is accessible by incident light frequencies below the intersection of the mode dispersion with the light line in the prism. At a particular frequency, the momentum of the incident light parallel to the interface is matched to that of the SPP by variation of the incident angle of the light within the prism. This coupling scheme is referred to as attenuated total reflection, because the angle which accomplishes this is beyond the angle of total internal reflection. The prism can be implemented on either side of the interface, replacing either of the two semi-infinite media with a finite thickness film. The more common configuration, and the one that will be employed in this dissertation, is the Kretschmann configuration [39], in which a finite thickness metal film is sandwiched by prism and dielectric material as shown in Figure 12.

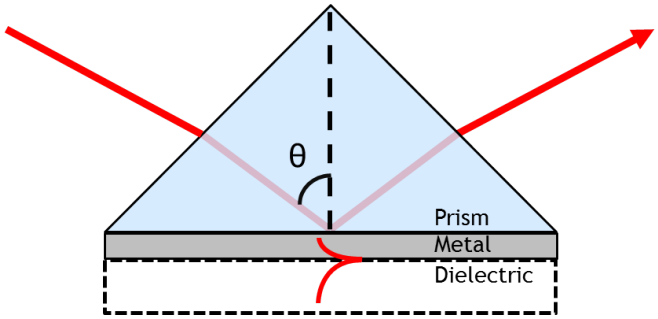

FIGURE 12. Kretschmann configuration for coupling to SPPs. Light incident on the silver from the glass at an angle θ excites SPPs on the opposite surface of the silver, along the interface with the adjacent dielectric as indicated with the cartoon of the field amplitude profile.

Surface Plasmon Resonance Features

Using the Kretschmann configuration described above, it is possible to excite surface plasmons on the metal/dielectric interface. The incident light must be

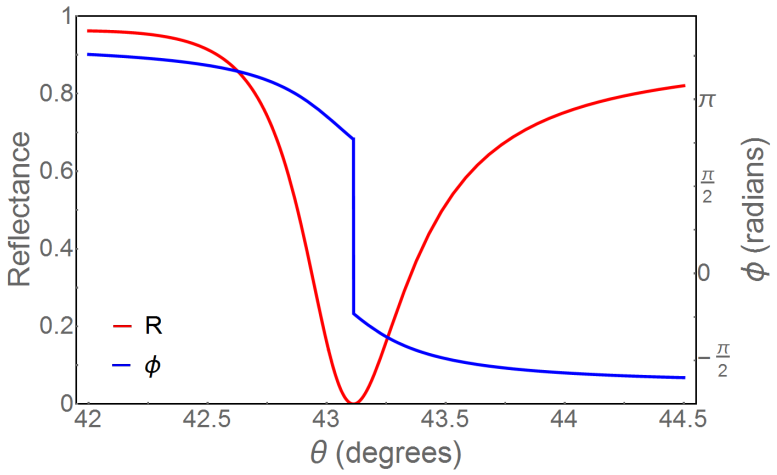

FIGURE 13. SPR angular reflectance and phase.
Calculated for a glass prism, silver, and air in the Kretschmann configuration using Palik data for the silver permittivity[65]. The thickness of the silver film is optimized to give zero reflectance at the resonance minimum and exhibits a π jump in phase at the angle of minimum reflectance.

polarized with p, or transverse magnetic, polarization so that the electric field oscillates within the plane of incidence and penetrates the metal film. Variation of the angle of incidence affects the projection of the momentum along the surface according to $k_{\|} = \frac{\omega}{c}\sqrt{\epsilon}\sin(\theta)$. By varying the incident angle of the beam upon the surface and measuring the output at the specular beam, we can map out the angular reflectance spectrum. Above the angle for total internal reflection, there will be a dip in the reflectance, shown in Figure 13 along with the accompanying phase profile, which corresponds to the excitation of SPPs. This profile is referred to as the resonance lineshape. It can be observed not only in the angular domain, but also with variation in wavelength of the incident light or permittivity of the dielectric adjoining the metal film. The resonance is slightly asymmetric, with the larger magnitude slope occurring on the side of the resonance nearer the angle of total internal reflection. The width and depth of this resonance depend on the parameters involved; they can be tuned, for example, through variation of the thickness of the metal film.

For a particular wavelength of incident light and set of prism, metal, and dielectric materials, there is a critical thickness of the metal film for which the reflectance drops to zero at the minimum of the resonance. This occurs when the intrinsic damping is equal to the radiative damping [74]. As the thickness of the metal film is detuned from this critical value in either direction, the resonance becomes shallower. For thicknesses below this critical thickness, the shallower resonance is also broadened and shifted to higher angle, whereas for thicknesses above this critical value the resonance narrows and the resonance minimum trends toward a lesser angle. This behavior is portrayed in Figure 14 for film thicknesses ranging from 25 nm to 75 nm.

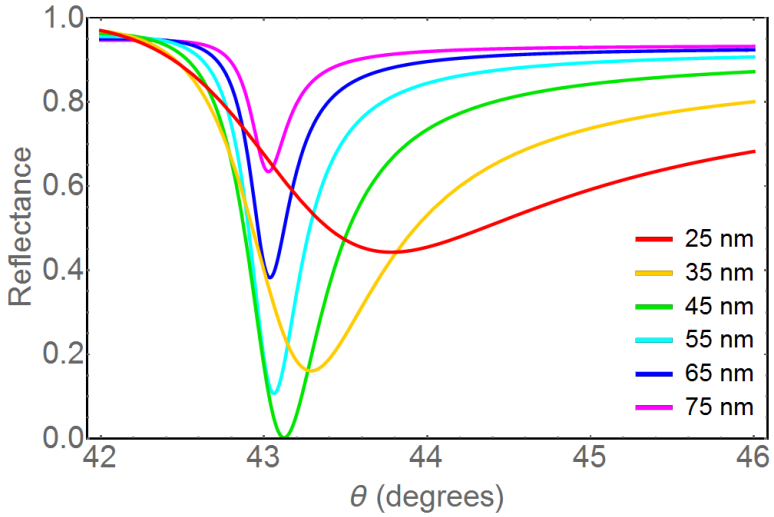

FIGURE 14. SPR angular reflectance for varied silver film thicknesses. Computed for a glass prism, silver, and air in the Kretschmann configuration with silver film thickness varied as indicated. Changes in thickness of the film alters both the location of the minimum and the depth of the resonance curve.

In addition to the zero in reflectance, the critical thickness metal film is also marked by a singularity in the differential phase and a π phase jump on resonance [57]. The magnitude of the phase slope on resonance decreases as the film thickness departs from this critical value. In addition, the sign of the slope flips across this critical thickness; it is negative for thinner films and positive on resonance for thicker

films. This behavior is shown in Figure 15, which displays the phase profiles for silver film thicknesses ranging from 25 nm to 75 nm.

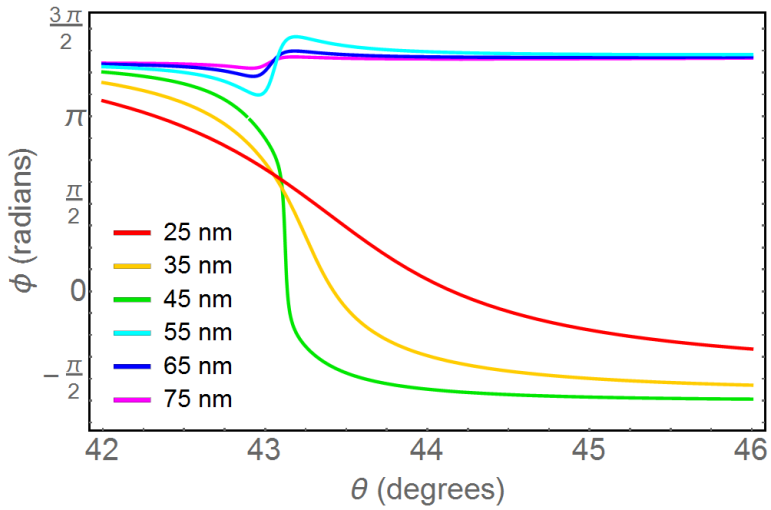

FIGURE 15. Angular dependence of SPR phase with varied film thickness. Computed for a glass prism, silver, and air in the Kretschmann configuration with silver film thickness varied as indicated. Steeper phase profiles are accomplished by tuning the thickness nearer the critical value. The slope of the phase on resonance is negative for thicknesses below this critical value and positive for thicknesses above.

These features of a narrow intensity resonance and large differential phase are advantageous when employed in sensing applications. For intensity based sensors, which rely on measurement of the reflectance, it is the slope of the reflectance which is crucial. For this reason it is advantageous to maximize the slope, which occurs at a position slightly detuned from the minimum of the resonance. When operated in this way, a small change in the material parameter to be detected will induce the largest possible change in intensity. By the same argument, intensity based detection schemes tend to operate near the angle which minimizes the intensity, which exhibits the maximum slope in phase.

Sample Preparation and Characterization

The type of samples desired are smooth silver films with uniform thickness of approximately 50 nm. We choose to deposit the silver onto plain Corning soda-lime glass microscope slides which can then be easily adhered to, and subsequently removed from, the hypotenuse of a right angle prism using index matching liquids. The glass slides are cut to match the height of the prism using a score and snap technique, followed by a smoothing of the cut edges with lapping film. Smaller glass substrates, less than 1 cm on a side, were also cut and deposited on, to be used later for characterization by atomic force microscopy (AFM). The slides are cleaned before deposition with a drop and drag technique using acetone and ethanol. Plasma cleaning and piranha cleaning methods were also tested for comparison but made no noticeable difference in the quality of the deposited films.

Once the substrates have been prepared, sample fabrication is performed in the Center for Advanced Materials Characterization in Oregon (CAMCOR) facility at the University of Oregon. The film is thermally evaporated using the Amod deposition system from Angstrom Engineering with the substrates mounted on a rotating plate within the chamber to facilitate uniform deposition. We use a source material of 99.99% pure silver pellets from Kurt J. Lesker company resting in a molybdenum boat. The silver is deposited under vacuum conditions of approximately 10^{-6} torr with deposition rates ranging from 0.1-15 Å/s onto glass substrates trimmed to the desired size and cleaned as described above. Deposition rates are primarily chosen from the higher end of this range in order to deposit higher quality films [75]. The thickness of the Ag films is controlled both by deposition rate and by variation of the deposition time and is monitored by a quartz crystal microbalance (QCM) mounted in the deposition chamber. Because of their differing locations, a tooling factor is

calculated to related the QCM thickness to the thickness of the film deposited on the substrate. Upon completion of the fabrication procedure, samples are stored under nitrogen to preserve their integrity until ready for use.

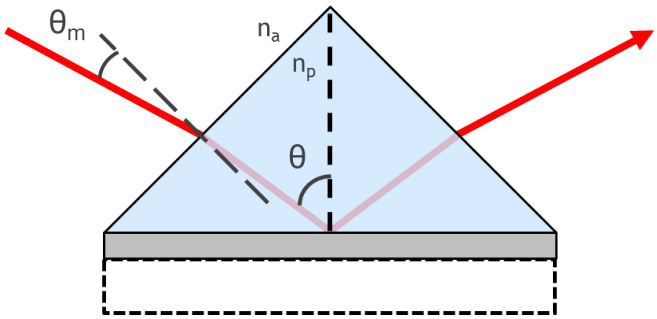

FIGURE 16. Schematic for angle conversion.
Displays the geometry needed to relate the incidence angle within the prism, θ, to the angle of the motorized rotation stage, θ_m, required to achieve this incidence.

To optically interrogate a sample, it is removed from the dry box and promptly mounted, with the silver film facing outward, onto the hypotenuse of a Thorlabs 25 mm right angle BK7 glass prism using Cargille refractive index liquid. The index matching liquid is applied so as to eliminate any air gaps between the prism and glass slide and to provide a constant refractive index environment to remove any disruption of the incoming beam. The prism, with the silver film now attached, is mounted onto a motorized rotation stage, enabling variation of the angle of incidence of the source beam onto the sample. The motor angle is set to zero for 45 degree incidence on the back of the prism. The angle of the motorized stage can then be related to the angle of incidence within the prism through the use of basic geometry and Snell's law yielding

$$\theta_m = \arcsin\left(\frac{n_a}{n_p}\sin\left(\theta - \frac{\pi}{4}\right)\right) \tag{3.14}$$

where n_a and n_p and the refractive indices of the air and prism respectively, and θm and θ are the angles of the motorized stage and incidence within the prism as

indicated in Figure 16. The beam spot on the back of the sample is aligned as closely as possible over the center of rotation of the motorized stage so that the same region of the sample is interrogated as the prism is rotated and the specularly reflected beam emanates from the same location over a range of angles. Two inch diameter optics are used to collimate the output and focus it onto the detector allowing an angular scan over nearly ten degrees to be completed without repositioning of the detector. Detection is performed with a silicon photodiode through a lock-in amplifier designed to pick out the optical signal modulated by an optical chopper wheel at 911 Hz. The motorized rotation and signal collection is controlled via GPIB interface with a computer running LabVIEW software.

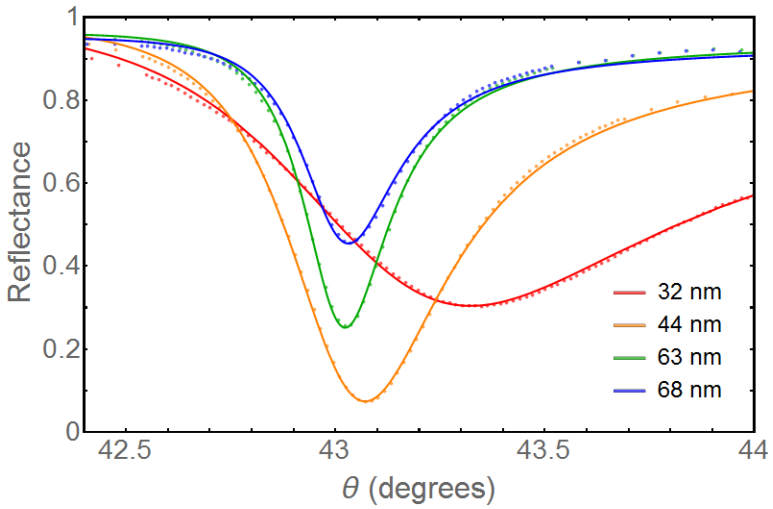

FIGURE 17. Angular reflectance experimental data with best fit functions. Silver films of different thickness were deposited by variation of deposition time and characterized optically. The dots are the experimental optical data points and the solid lines are a least squares fit to that optical data. The thickness values indicated in the legend are those output by the fitting procedure.

The optical data collected is then analyzed in Mathematica. Reflectance from the SPR configuration is computed by $R = |r|^2$ with reflectivity, r, of a single thin

film system given by [76]

$$r = \frac{r_{12} + r_{23}e^{-2i\delta}}{1 + r_{12}r_{23}e^{-2i\delta}} \tag{3.15}$$

where r_{ij} is the p wave reflectivity at the interface between two materials, i and j, with relative permittivities ϵ_i and ϵ_j and angles of incidence θ_i and θ_j according to

$$r_{ij} = \frac{\sqrt{\epsilon_i}\cos(\theta_j) - \sqrt{\epsilon_j}\cos(\theta_i)}{\sqrt{\epsilon_i}\cos(\theta_j) + \sqrt{\epsilon_j}\cos(\theta_i)} \tag{3.16}$$

and where the parameter δ is proportional to the film thickness, d, and is given by

$$\delta = \frac{2\pi d}{\lambda}\sqrt{\epsilon_2}\cos(\theta_2) \tag{3.17}$$

Thickness characterization of the samples is performed via a three parameter fit to the reflectance data with the three parameters being the real and imaginary parts of the permittivity and the thickness of the silver film. The optical data, along with the best fit curves, are shown in Figure 17 for a set of four samples fabricated with different deposition times. The determined film thicknesses are displayed in the plot legend and the permittivity values for silver are consistent with the literature [65, 77].

TABLE 1. Best fit parameter values from optical film characterization.

Property	Fit to Optical Data	Independent Verification	Source
ϵ	-17.3 + 0.96 i	-15.9 + 1.07 i	Palik [65]
		-18.3 + 0.48 i	Johnson & Christy [77]
d	51.6 nm	50.5 nm	AFM

Using these thicknesses as calibration, the deposition time can be optimized to produce silver films with a resonance minimum even closer to zero than any of the initial samples. Figure 18 shows optical data in which the normalized reflectance dips

just below 0.05 at its minimum. Performing the fitting procedure as outlined above yields a film thickness of 51.6 nm and relative permittivity of $-17.3 + 0.97i$. Table 1 shows that this value falls between the values for the silver permittivity at this wavelength from Palik and Johnson and Christy.

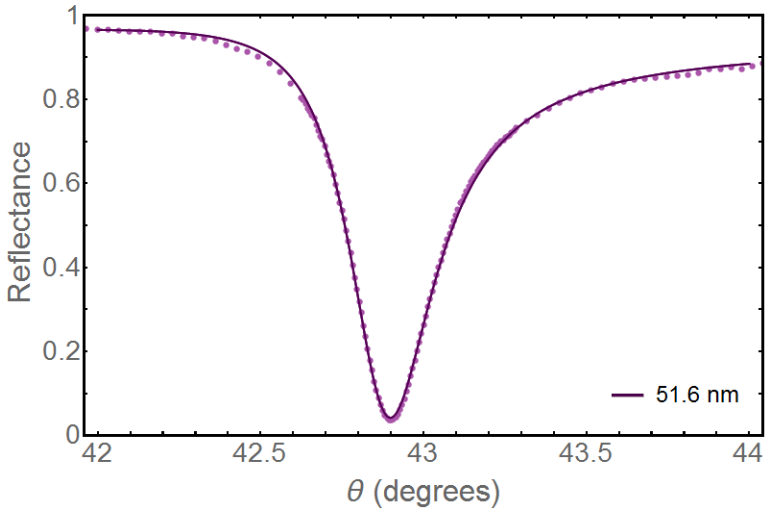

FIGURE 18. Angular reflectance data with fit for a near-critical thickness film. A near-critical thickness film was achieved based on the calibration from Figure 17 and then characterized optically. The dots represent the measured reflectance values and the solid line a fit to the optical data. The fitting procedure yields a relative permittivity of $\epsilon = -17.3 + 0.97i$ and thickness of 51.6 nm for the silver film.

For independent verification of film thickness we turn to AFM. Using CAMCOR facilities, thickness measurements for a sampling of deposited films were obtained by scraping the silver films deposited on the smaller glass substrates and scanning across the step left in its wake. This data obtained from this scan may then be analyzed to measure the film thickness. A visualization of the silver film and substrate of one of these samples, created using the NanoScope Analysis software package, is presented in Figure 19. An alternate presentation of this data is the plot of Figure 20. Here we plot the percentage of pixels at each height against the height as measured above the lowest pixel height. When viewed in this way, the data exhibits two clear peaks,

the lower one representing the substrate surface and the higher one representing the silver surface. The shoulder on the high end of the silver height distribution is a result of pileup along the edge caused by the scraping procedure. By fitting each of these peaks with a Gaussian distribution, we identify the film thickness as the difference between the centers of these distributions and obtain a measure of the roughness of the film via the full width at half maximum (FWHM). The resulting thickness, 50.5 nm, matches well with that from the optical data, as shown in Table 1. The roughness of the silver film is estimated at 2.8 nm. This analysis acts as independent verification of the film thickness value obtained via SPR and instills confidence in the thickness measurements obtained by the fitting procedures to the optical data.

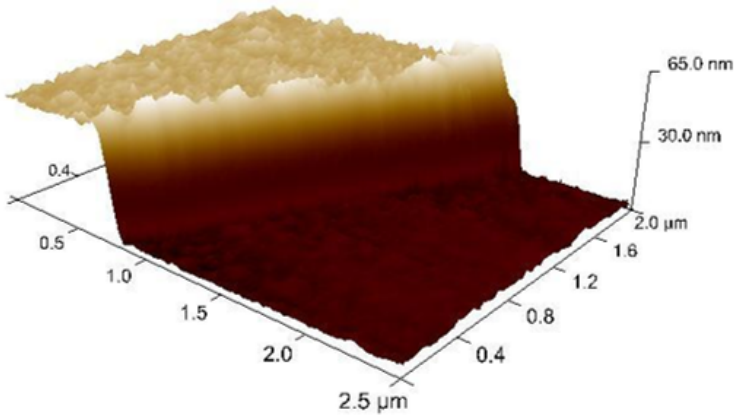

FIGURE 19. Visualization of silver film topography created from AFM data. Atomic force microscopy was used to independently verify the thickness of the silver film. The elevated surface on the left hand side of the figure is the top of the silver film and the lower surface on the right is the exposed glass substrate where the silver has been scraped off for a step height measurement. The image was generated using the NanoScope Analysis software package.

Summary

The intent of this chapter was to highlight the physics behind propagating surface plasmons and the accompanying resonance, as well as provide details regarding the

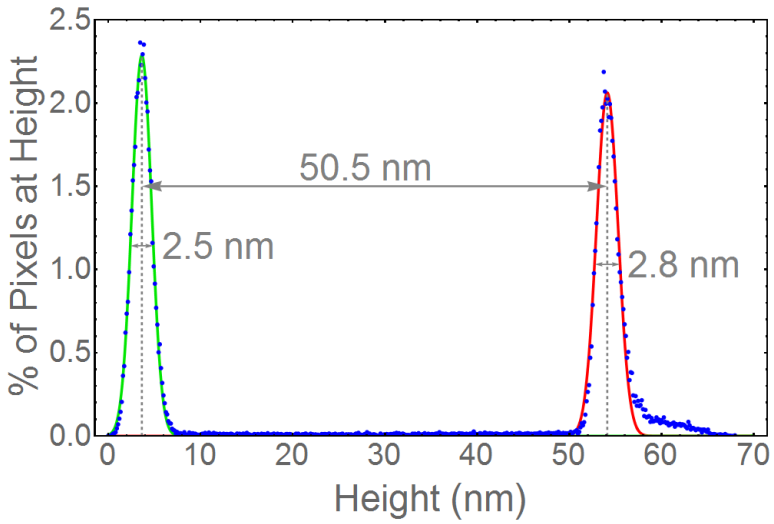

FIGURE 20. AFM step height analysis.
Pixel height data for the silver film was recorded via AFM. The peaks at the film and substrate surfaces are fit with Gaussian distributions to determine the film thickness as well as obtain a measure of the surface roughness. The shoulder on the high side of the rightmost peak is due to pileup of silver caused by scraping.

experimental preparation and characterization of samples to be used in the surface plasmon sensing experiments contained in the following chapters. We derived the dispersion relation for SPPs and discussed the physical significance of the material parameters which factor in to this equation. We discussed experimental configuration and procedures necessary to excite SPPs and observe the corresponding resonance. Finally, we demonstrated the ability to fabricate and characterize high quality silver films for use in the SPR sensing experiments. Armed with both the mathematical tools necessary to describe the system as well as the experimental techniques required to produce high quality samples, we proceed to construct a theoretical model which incorporates these features of the resonance within the architecture of the Sagnac interferometer.

CHAPTER IV

RESONANTLY ENHANCED SAGNAC INTERFEROMETRY

Overview

A resonantly enhanced Sagnac interferometer is simply one that incorporates a resonant system within the construct of the interferometer itself. Resonance is a ubiquitous phenomenon encountered in a wide variety of systems, so a discussion of resonantly enhanced Sagnac interferometers is broadly applicable. A few examples of resonances that are already being pursued within this geometry include atomic resonances [24–26], ring resonators [27–29], and coupled sequences of micro-resonators [30–33]. While the particular resonance used within the system will heavily influence the potential applications of said experiment, the mathematical formalism remains quite general. This is because of the near-universal resonance features: an approximately Lorentzian intensity profile accompanied by a steep change in phase on resonance. Introducing these features within the structure of the interference equations arrived upon in the second chapter produces interesting results and motivates further research in resonantly enhanced Sagnac interferometry. In this chapter we will describe the creation of a theoretical model to describe the system. We begin by describing the system to be modeled and detail the methods for introducing perturbations to the system. Then we display and analyze results for the normalized intensity at the dark port and compute the accompanying sensitivity. Next, we perform the same intensity and sensitivity analysis for the bright port. After that, we touch on the impacts of an angular detuning from the resonance minimum before finally summarizing the results obtained from this theoretical model.

Inclusion of a Resonance

In this work the interferometer is resonantly enhanced via surface plasmon resonance (SPR). The results are more broadly applicable; however, a particular resonance is chosen here to model a system that can be implemented and tested experimentally. A schematic diagram of the interferometer configuration under consideration is presented in Figure 21. Here the source beam is incident from the left and splits evenly at a 50/50 beamsplitter. The two resulting beams traverse the same overall path around the interferometer but in opposite directions. At the prism-coupled SPR element both beams undergo the resonant interaction, and upon returning to the beamsplitter the two beams interfere resulting in two interferometer output signals.

The resonant interaction specific to this system involves the coupling of light to SPPs. Upon reaching the SPR element, the counter-propagating beams excite counter-propagating SPPs at the metal dielectric interface. For this to occur, the conditions must be such that the momentum component of the incident light along the interface is matched to that of the SPP mode for beams incident from both sides of the prism. The metal film thickness used is tuned to match the intrinsic and radiative damping and will be referred to as the critical film thickness for SPR. As the thickness is detuned from this critical value, the magnitude of the differential phase decreases as shown in Figure 22. A large slope in the phase is crucial to provide the desired resonant enhancement effects. For this reason, we focus on metal film thicknesses at or near the critical thickness for the duration of this work.

After the beams have undergone the resonant interaction and propagated around the entirety of the interferometer loop, they recombine at the beamsplitter. The normalized intensities at the two output ports of the resonantly enhanced

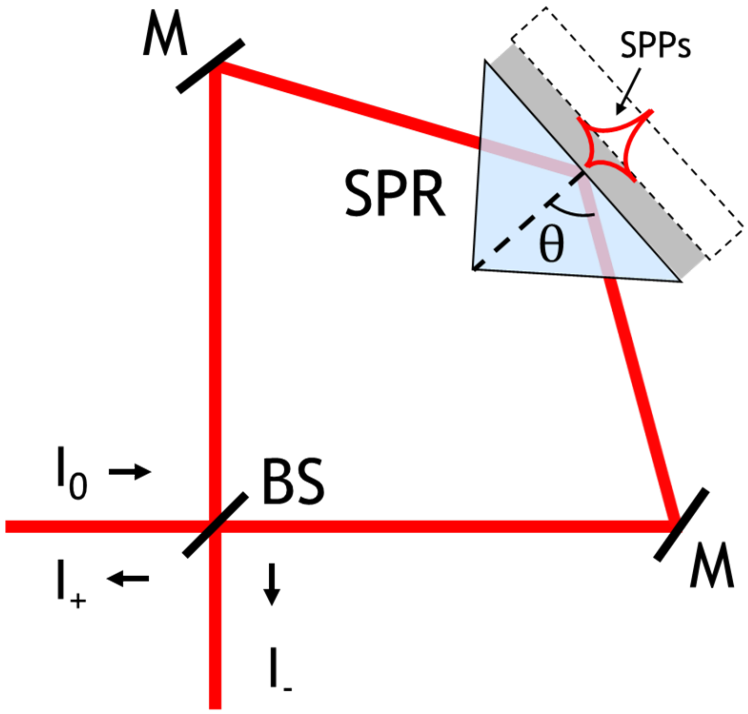

FIGURE 21. Resonantly enhanced Sagnac interferometer using SPPs.
In this schematic diagram, the Kretschmann prism configuration replaces one of the mirrors and the counterpropagating beams excite counterpropagating SPPs at the interface of the metal and dielectric.

interferometer are given by modifying the interference equations derived earlier to include the resonant terms.

$$I_{\pm} = \frac{1}{4}[R_1 + R_2 \pm 2\sqrt{R_1 R_2} cos\,(\phi_2 - \phi_1)] \tag{4.1}$$

Here R and ϕ represent the intensity and phase, respectively, due to reflection from the SPR element. Subscripts 1 and 2 distinguish the two counterpropagating paths around the interferometer while the plus and minus signs differentiate the two output ports. Aside from the resonant interaction, the phase accumulation in the remainder of the loop is assumed to be equal between the paths and the mirrors are assumed to be perfectly reflecting. This interference equation is generalizable beyond just SPR,

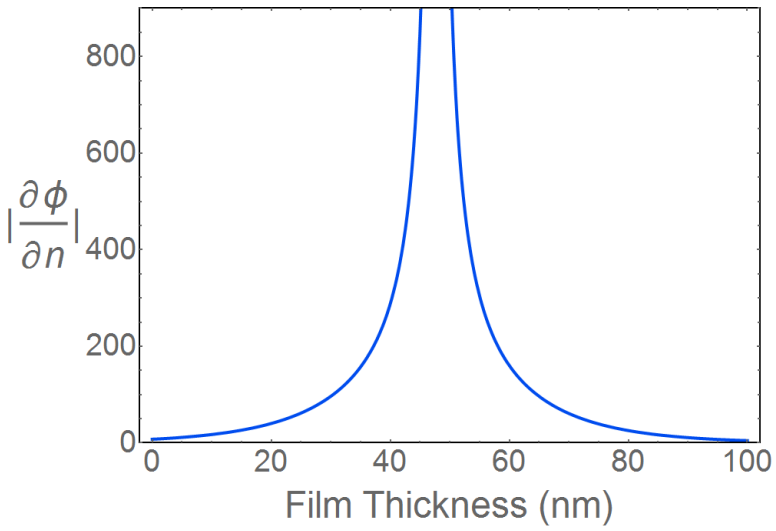

FIGURE 22. Differential phase magnitude with variation in metal film thickness. The magnitude of the differential phase is calculated on resonance. There is a singularity at the critical film thickness and the magnitude falls off sharply on either side.

and will serve as the basis of our investigation on the sensing capabilities of resonantly enhanced Sagnac interferometers.

Perturbation Detection

To explore these sensing capabilities, we investigate the response of the system to external perturbations. In this work, we choose to model perturbations as a refractive index detuning applied to the lower-index dielectric opposite the prism in the SPR configuration. This dielectric is chosen to exhibit perturbations as a matter of practicality, since a common application of SPR is to detect ultrasmall shifts in refractive index of this dielectric[46]. This refractive index value is one of the parameters that goes into the calculation of the R and ϕ terms in Equation 4.1, computed using the Fresnel equations. The reflectance and phase dependence on the refractive index of this outer dielectric, for a fixed angle of incidence, reproduce the expected general resonance features as shown in Figure 23. The reproduction of

a nearly-Lorentzian dip in the reflectance accompanied by a steep change in phase on resonance justifies the choice to introduce perturbations to the refractive index of the lower-index dielectric. However, the results are general to a detuning in any parameter of a resonant system that similarly influences a resonance.

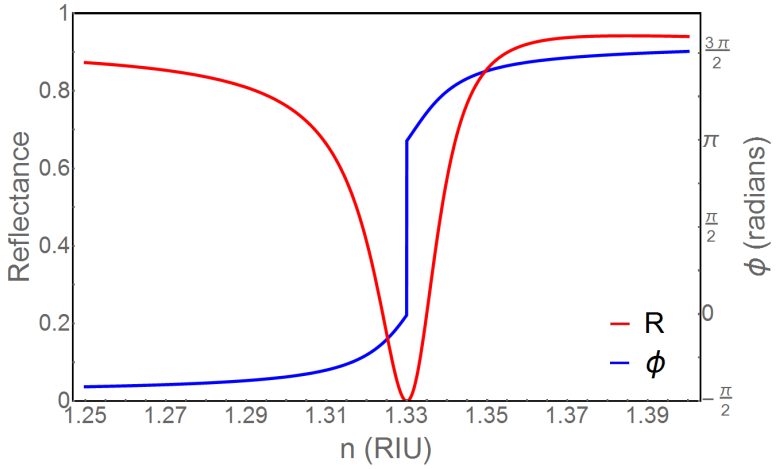

FIGURE 23. SPR reflectance and phase in the refractive index domain. Computed for a configuration consisting of a glass prism, silver, and dielectric of refractive index n. The film thickness and incidence angle are optimized for maximum coupling to SPPs at the refractive index of water. The resonance features in this domain are qualitatively similar to those in the angular domain.

Perturbations to the system fall into one of two classifications: reciprocal or nonreciprocal. For reciprocal phenomena, the perturbation affects both the clockwise and counter-clockwise paths of the Sagnac interferometer equivalently. In the terms of Equation 4.1, this means that for purely reciprocal effects, $R_1 = R_2$ and $\phi_1 = \phi_2$. Reciprocal perturbations are implemented in this work by adding Δn to the refractive index as seen by both the clockwise and counter-clockwise propagating paths. Although no phase difference is introduced by a reciprocal effect, a change in reflectance caused by the detuning has the potential to alter the interferometer output according to Equation 4.1. One example of a reciprocal perturbation to the lower-index dielectric in the Kretschmann configuration is a temperature drift. A

temperature drift shifts the refractive index according to the thermo-optic coefficient of the material, but the shift is independent of the direction of beam propagation around the loop [44].

On the other hand, a perturbation is nonreciprocal if it depends on the direction of propagation. These phenomena break the symmetry between the counter-propagating paths of a balanced interferometer such that $\phi_1 \neq \phi_2$. As seen from Equation 4.1 this phase difference alters the nature of the interference, moving from constructive toward destructive or vice versa. This, in combination with any intensity changes introduced by the detuning, fully describes the change in signal measured at the bright and dark ports. We choose to implement a nonreciprocal detuning by adding Δn to the refractive index of the lower-index dielectric as experienced by one path and subtracting Δn from the refractive index of the same dielectric as seen by the counter-propagating path. For reference, the phase difference produced by a nonreciprocal detuning of $|\Delta n| = 10^{-7}$ is plotted in Figure 24 for metal film thicknesses near the critical thickness. The phase difference peaks sharply at the resonant angle, prompting operation of the sensor at this fixed angle of incidence. The magnitude of the peak grows as the film thickness approaches the phase singularity on resonance as seen in Figure 22, reflecting the benefit of a large differential phase associated with the near-critical thickness films. An example nonreciprocal perturbation of refractive index is uniform translational motion of the lower-index dielectric adjacent to the metal film in the SPR configuration[78, 79]. For a moving dielectric, there is a relativistic drag effect known as Fresnel-Fizeau drag [80, 81] which imparts a phase shift dependent on the scalar product of the velocity vector of the dielectric and the SPP propagation direction. This directional dependent phase difference amounts to a nonreciprocal detuning in the refractive index of the dielectric.

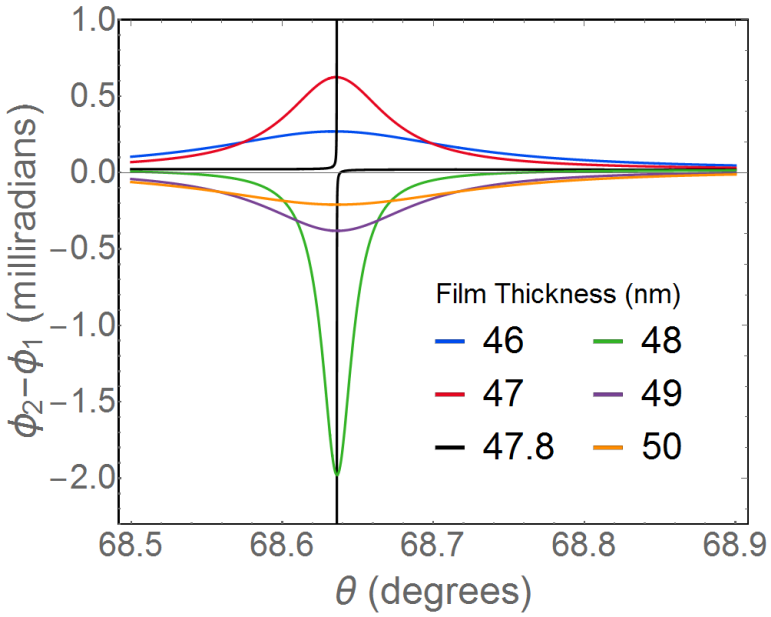

FIGURE 24. Phase difference produced by a nonreciprocal perturbation. The perturbation is introduced as a shift in the refractive index with a magnitude of $|\Delta n| = 10^{-7}$. The phase difference peaks sharply at the resonant angle and the magnitude is greater for film thicknesses near the critical value.

In many cases, both reciprocal and nonreciprocal phenomena will be present simultaneously. This is often unwanted as it can contribute additional noise to the system, but may be unavoidable under certain circumstances. For example, while studying a nonreciprocal flow there will be a limit on how precisely the temperature may be controlled. In these instances, one might wish to measure both nonreciprocal and reciprocal effects simultaneously: such as the velocity of a moving dielectric and any temperature change associated with it. In order to do so accurately, we should utilize a device in which the response of the system to one type of perturbation is able to be dependably distinguished from the response of the other. In this chapter we will show that the resonantly enhanced Sagnac interferometer is capable of achieving this level of discrimination. The dark port displays a high sensitivity to nonreciprocal fluctuations and is robust against reciprocal phenomena. Meanwhile, the bright port

is highly sensitive to reciprocal drifts while maintaining a relative insensitivity to nonreciprocal effects.

Dark Port Intensity

We begin by exploring the response of the dark port to both nonreciprocal and reciprocal perturbations. For the nonreciprocal response, we plot I_- from Equation 4.1 as a function of the nonreciprocal detuning. This nonreciprocal detuning alters the refractive index of the dielectric by the same magnitude, but in opposite directions for the two paths. It is performed for near-critical thickness metal films while maintaining a fixed incidence angle in the prism, the resonant angle for the SPR system. Under these initial conditions, the field reflectance from the SPR element is at its minimum. As we detune from this resonant minimum, the reflectance values of the two counter-propagating signals do increase but remain nearly equivalent, with differences owing to a slight asymmetry in the resonance lineshape. Along with intensity changes, the nonreciprocal detuning introduces a phase difference between the two paths. As this phase difference accumulates it causes a switching from destructive to constructive and then back to destructive interference at the dark port output. This results in the nonmonotonic behavior of the normalized intensity output seen in Figure 25. This general lineshape persists for film thickness on either side of the critical value. The first shift from destructive to constructive interference happens rather abruptly due to the π phase change on resonance. This resonant phase behavior provides a significant phase difference with the introduction of only a slight detuning to the perturbed parameter in the system, in this case the refractive index of the dielectric. The result is a strong enhancement in the output intensity at the dark port. This resonantly

enhanced signal provides a sensitivity to nonreciprocal phenomena in the dark port greater than that achievable in a nonresonant Sagnac interferometer.

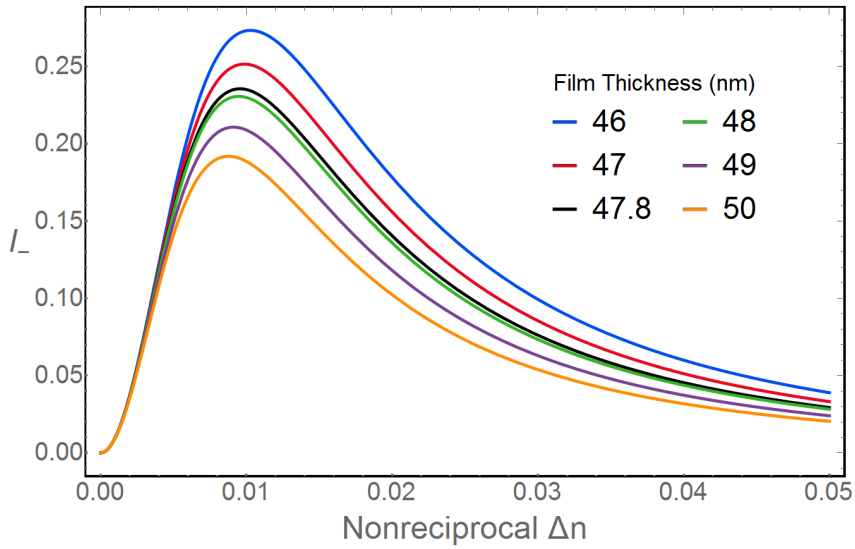

FIGURE 25. Dark port response to nonreciprocal perturbations. Normalized intensity output at the dark port, I_-, exhibits nonmonotonic behavior with the introduction of nonreciprocal phenomena. The film thickness is varied as denoted in the legend.

In addition to the strong nonreciprocal response, a relative insensitivity of the signal to reciprocal phenomena is needed to fully realize the potential of the dark port as a sensor of nonreciprocal phenomena. We model reciprocal sensing in the dark port by computing I_- as a function of the reciprocal detuning. The reciprocal detuning is implemented as described earlier, with Δn equivalent for both interferometer paths. Again, the incidence angle in the prism remains fixed at the resonant angle of SPR, where the reflectance is at its minimum. As we detune the system, the intensity upon reflection from the SPR element increases; identically in both paths for reciprocal detuning. Unlike the nonreciprocal case, the phase remains equivalent in both paths. Because of this, the output retains its destructive interference and the intensity remains zero, despite the intensity increase in the counter-propagating

paths. The result is a signal completely insensitive to the introduction of purely reciprocal phenomena.

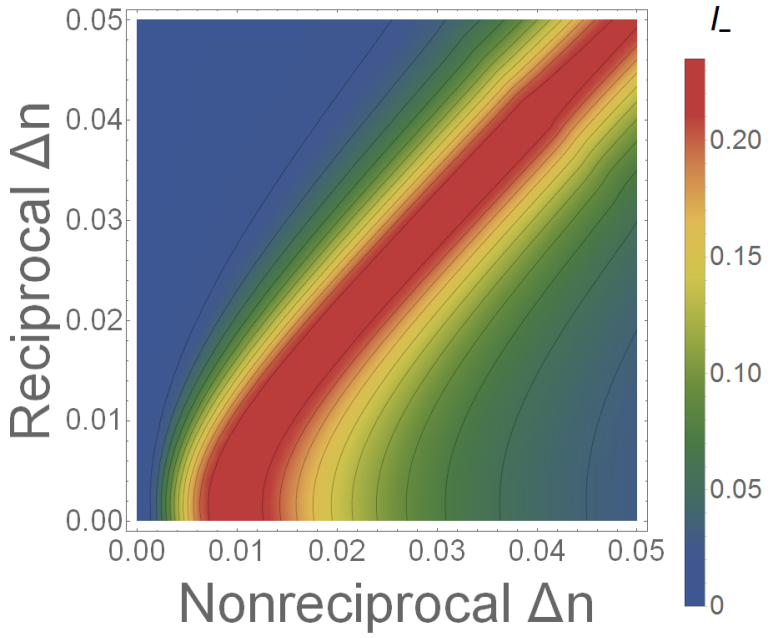

FIGURE 26. Dark port perturbation response.
Normalized output intensity, indicated by the color bar, as a function of both reciprocal and nonreciprocal detunings.

But what happens when reciprocal and nonreciprocal phenomena are present simultaneously? To determine the robustness of the system, we consider the system response in the presence of both types of phenomena. This response is plotted in Figure 26. Here we see that the system maintains its nonmonotonic behavior as a function of nonreciprocal detuning even in the presence of reciprocal phenomena. However, unlike before, we observe that the reciprocal detuning can influence the intensity output when occurring in conjunction with nonreciprocal effects. The nonreciprocal effect introduces a phase difference at the output so there is no longer complete destructive interference. Because of this, intensity variations of the counter-propagating paths owing to reciprocal perturbations can begin to affect the output signal. This result is unique to the resonantly enhanced interferometer and can

reintroduce noise that the nonresonant Sagnac interferometer is constructed to be immune to. While this may be a subtle effect, it is important to consider when utilizing a resonantly enhanced system.

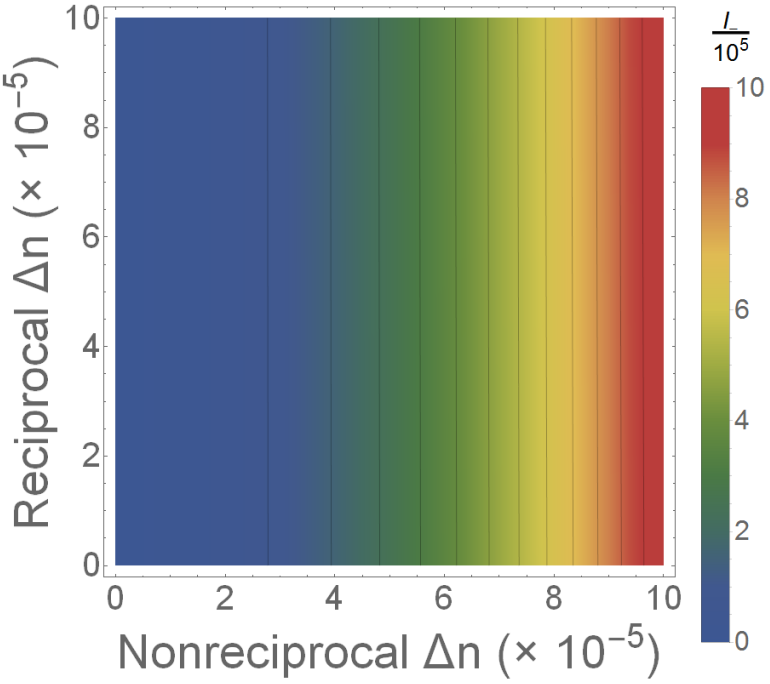

FIGURE 27. Dark port response to small perturbations.
A zoomed-in view of Figure 26. The near-vertical contours suggest a strong response to nonreciprocal perturbations and relative insensitivity to reciprocal phenomena.

Dark Port Sensitivity

Under certain circumstances, the sensitivity to reciprocal effects in the dark port will be small enough that it may be safely neglected and the dark port signal used for detection of nonreciprocal phenomena. As evident by Figure 27, a zoomed-in version of Figure 26, in the region of small detunings the dark port remains largely insensitive to the reciprocal perturbations. For larger detunings, the effect is large enough to influence the behavior of the output intensity. In practice, this sets a limit on the sensing capabilities of the dark port. Reciprocal detunings must be kept small enough

so as to be insignificant compared to nonreciprocal detunings in order to definitively attribute the response of the dark port to a nonreciprocal perturbation.

To further quantify the performance of the resonantly enhanced Sagnac interferometer we analyze its sensitivity. We define the sensitivity in the dark port as $S_- = \frac{\partial I_-}{\partial \Delta n}$, where Δn is the magnitude of either the reciprocal or nonreciprocal detuning. The sensitivity is plotted against Δn to illustrate how the sensitivity varies with the strength of the perturbation. While one of the detunings is varied, the other is held fixed at a constant detuning of $|\Delta n| = 10^{-7}$ to exemplify the system behavior in the presence of other perturbations. Figure 28 shows both the nonreciprocal and reciprocal sensitivities in the dark output port as a function of the magnitude of the respective detuning. The incidence angle in the prism and thickness of the metal film are held fixed at the resonant angle and the critical SPR thickness, respectively. As seen in the figure, the sensitivity to nonreciprocal effects is orders of magnitude larger than the sensitivity to reciprocal effects in the dark port. This significant difference in sensitivity persists over a wide range of detunings making the dark port an effective detector of nonreciprocal phenomena.

As compared with other surface plasmon sensors, this eases detection of nonreciprocal effects. While these effects are capable of detection in an intensity-based, or even a Mach-Zehnder configuration phase-based scheme, these techniques are more easily contaminated by reciprocal noise. For example, in detection of a dielectric flow, the drag effect would induce a shift in the intensity and phase upon reflection. However, so would a temperature drift, necessitating precise temperature control in these experiments. In the resonantly enhanced Sagnac interferometer not only is the sensitivity to nonreciprocal perturbation enhanced, but small reciprocal perturbations are also, to a large extent, filtered out. This allows for a relaxation of

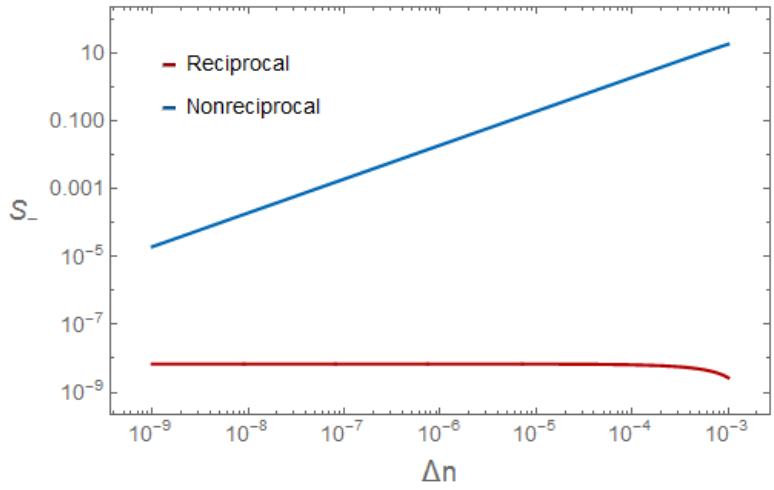

FIGURE 28. Nonreciprocal and reciprocal sensitivity in the dark port. The reciprocal sensitivity is plotted for reciprocal Δn varied and a constant nonreciprocal detuning of $|\Delta n| = 10^{-7}$. For the nonreciprocal sensitivity curve, Δn is the magnitude of the nonreciprocal detuning and the reciprocal detuning is held fixed at 10^{-7}.

constraints such as precise temperature control typically required in such experiments. These same principles can be applied to any nonreciprocal perturbation that may also be accompanied by reciprocal phenomena.

Persistence of Results

In experiments designed to detect both types of perturbations simultaneously, the strength of both types of perturbations may exceed the $|\Delta n| = 10^{-7}$ value that was used to hold one type of perturbation constant in the previous calculation of the sensitivity. The question then becomes, how much could these constraints be relaxed while maintaining a large gap between the sensitivity to nonreciprocal and reciprocal phenomena. To explore the extent of the nonreciprocal dominated regime, we modify the calculation described above by increasing the magnitude of the Δn held constant. For example, Figure 29a displays reciprocal sensitivity with $|\Delta n|$ nonreciprocal held fixed at 10^{-6} and nonreciprocal sensitivity with Δn reciprocal also

held fixed at 10^{-6}. This is repeated in Figure 29b but with the parameter adjusted down to 10^{-5}. Comparison of these plots with that of Figure 28 shows that the trace of the nonreciprocal sensitivity exhibits little change. However, the reciprocal sensitivity grows as the magnitude of an also present nonreciprocal perturbation increases. This significantly lessens the gap between the two on the left side of the plot, but the discrepancy persists for higher detunings. As it turns out, the leftmost side of the plot contains a bit of an incongruity; the red trace shows the reciprocal sensitivity when a nonreciprocal perturbation of magnitude $|\Delta n| = 10^{-5}$ is present. In the presence of a nonreciprocal perturbation of this magnitude, it is no so instructive to focus on the nonreciprocal sensitivity to a perturbation of magnitude $|\Delta n| = 10^{-9}$. Instead, it is more illuminating to look further along the x-axis at $\Delta n = 10^{-5}$ where we see a discrepancy between the sensitivities of three orders of magnitude. This illustrates the effectiveness of this device as a simultaneous detector when both effects are present with larger strength in addition to the previously discussed potential of enhanced nonreciprocal phenomena in the regime closer to pushing the lower limits of perturbation detection.

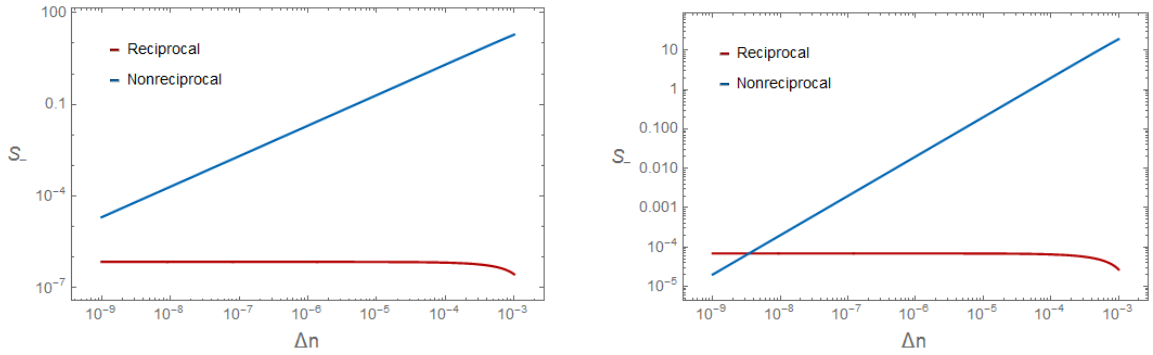

(a) (b)

FIGURE 29. Dark port sensitivity for simultaneous detection. (a) Same as Figure 28 except that the $|\Delta n|$ not varied is held fixed at 10^{-6}. (b) Same again, but now with the $|\Delta n|$ not varied is held fixed at 10^{-5}.

We also consider the impact on sensitivity of variation in the silver film thickness. Figure 30 shows the sensitivity to reciprocal and nonreciprocal phenomena for two supercritical thicknesses. These films are 3 nm and 6 nm thicker than the critical thickness film which reaches zero at the minimum of the resonance. As with Figure 28, the type of perturbation held fixed is done so at a constant detuning of $|\Delta n| = 10^{-7}$. We observe very minimal deviation from the sensitivity at critical thickness suggesting that the dark port sensitivity is quite forgiving with respect to deposited film thickness.

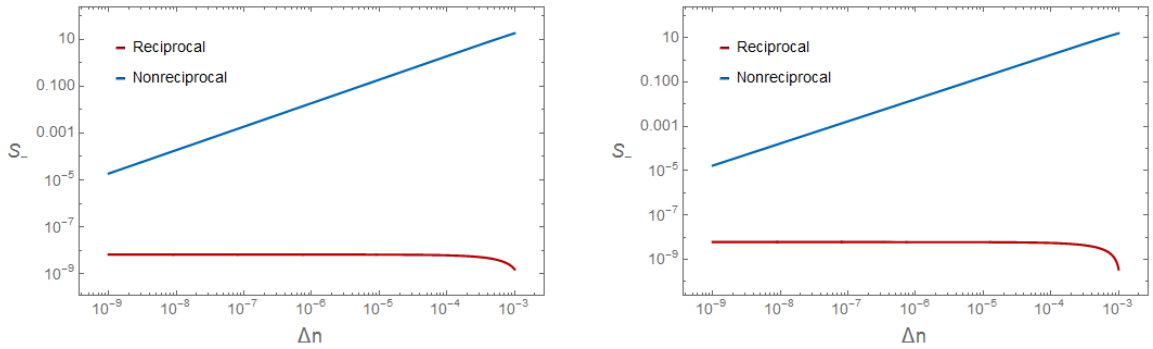

(a) (b)

FIGURE 30. Dark port sensitivity for supercritical thickness. (a) The reciprocal and nonreciprocal sensitivity are plotted for a silver film thickness 3 nm greater than the critical thickness. (b) The reciprocal and nonreciprocal sensitivity are plotted for a silver film thickness 6 nm greater than the critical thickness. In both cases, very little deviation from the sensitivity at critical thickness is observed.

Bright Port Intensity

In a balanced interferometer, the bright port exhibits perfectly constructive interference. This remains the case for the resonantly enhanced system. Even still, the bright port exhibits low signal intensity when the system is aligned at the resonant angle of SPR. This is due to the reflectance from the SPR element being at its minimum, specifically zero in the case of the critical thickness film. This serves as

our starting point in the bright port; we proceed to introduce perturbations to the adjacent dielectric and investigate the system response.

We investigate the reciprocal sensitivity in the bright port by plotting I_+ from Equation 4.1 as a function of the reciprocal detuning. Because no phase difference is introduced between the two counter-propagating paths in a reciprocal detuning, the bright output port retains its constructive interference. However, the introduction of a detuning causes a shift away from the reflectance minimum, increasing the intensity in the counter-propagating paths and thus the intensity at the bright output port. The intensity at the output as a function of the reciprocal detuning is shown in Figure 31. Here we see that the introduction of a reciprocal perturbation results in an interferometer output that is modulated by the resonance lineshape. Again, this result is unique to the resonantly enhanced system. In the absence of the intensity modulation provided by the resonance, for example at an off-resonant angle with flat reflectivity response, the intensity at the bright port would be unaffected.

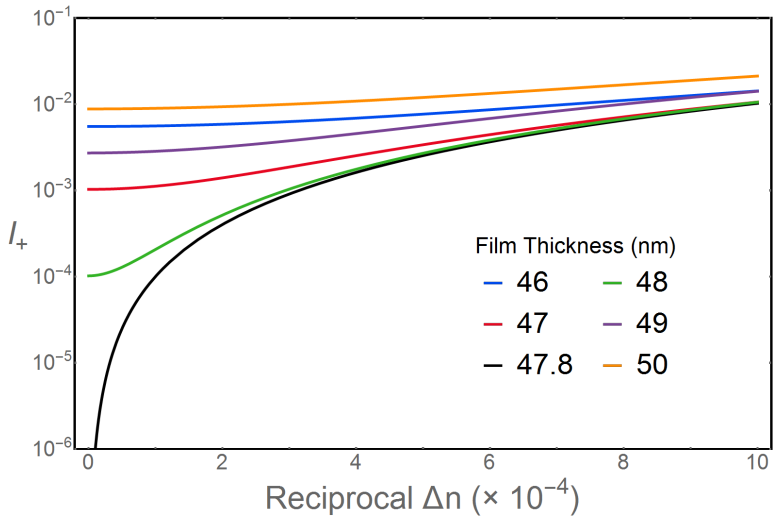

FIGURE 31. Bright port response to reciprocal perturbations. Normalized intensity output at the bright port, I_+, increases as perturbations shift the system away from the resonance minimum. The film thickness is varied as denoted in the legend.

Having looked at the bright port response to reciprocal detunings, we move on to investigate the response to nonreciprocal detunings. We model nonreciprocal sensing in the bright port by computing I_+ as a function of nonreciprocal detuning. Similarly to the dark port, nonreciprocal detuning increases the reflectance from the SPR element as we detune from the minimum of the resonance. In addition, the phase difference introduced by the nonreciprocal perturbation leads to a change in the nature of the interference at the output. In the bright port, the interference switches from constructive to destructive and then back to constructive. Because of this, the bright port also exhibits nonmonotonic behavior as a function of nonreciprocal detuning. Unlike the response of dark port, we do not see a resonant enhancement of the interferometer output in the bright port. This is due to the fact that the π change in phase across resonance shifts the output from constructive interference to nearly complete destructive interference. The result is a near-perfect cancellation of terms in the bright port, thus minimizing the effect of the intensity increase away from resonance.

For a fuller picture, it is instructive to consider the output response in the presence of both type of effects. Figure 32 shows the normalized intensity at the bright port as a function of reciprocal and nonreciprocal detunings. The metal film thickness and incident angle are held fixed at the critical and resonant values, respectively. The overall trend of this density plot looks similar to that of the dark port but with a valley running diagonally across the plot rather than a ridge. The key difference comes when we focus in on smaller detuning and begin to analyze the sensitivity.

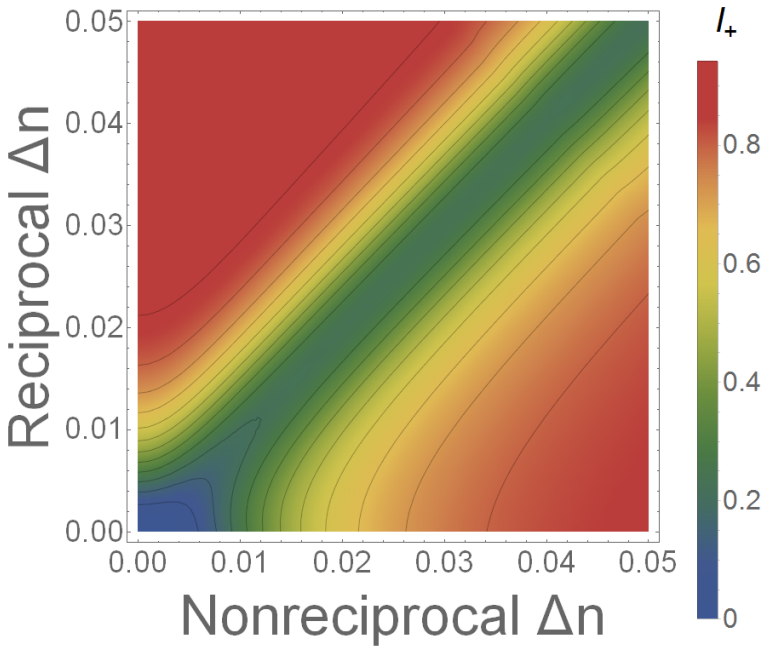

FIGURE 32. Bright port perturbation response.
Normalized output intensity, indicated by the color bar, as a function of both reciprocal and nonreciprocal detunings.

Bright Port Sensitivity

For small nonreciprocal detunings the bright port signal is dominated by the reciprocal response. Figure 33 displays the response for small detunings where the reciprocal response dominates, as opposed to much of Fig 32 where the effects are comparable in magnitude. This sets a constraint on the sensing capabilities of the bright port. As long as the nonreciprocal signal is sufficiently small, as is often the case particularly when pushing the lower limits of detection, the bright port can be used as a monitor of the reciprocal drift. To illustrate this we perform a more rigorous analysis of the sensitivity.

Using $S_+ = \frac{\partial I_+}{\partial \Delta n}$ as our definition for sensitivity in the bright port, we perform similar calculations as was done for the dark port. Figure 34 shows the sensitivity to reciprocal and nonreciprocal effects in the bright port. While one detuning is varied,

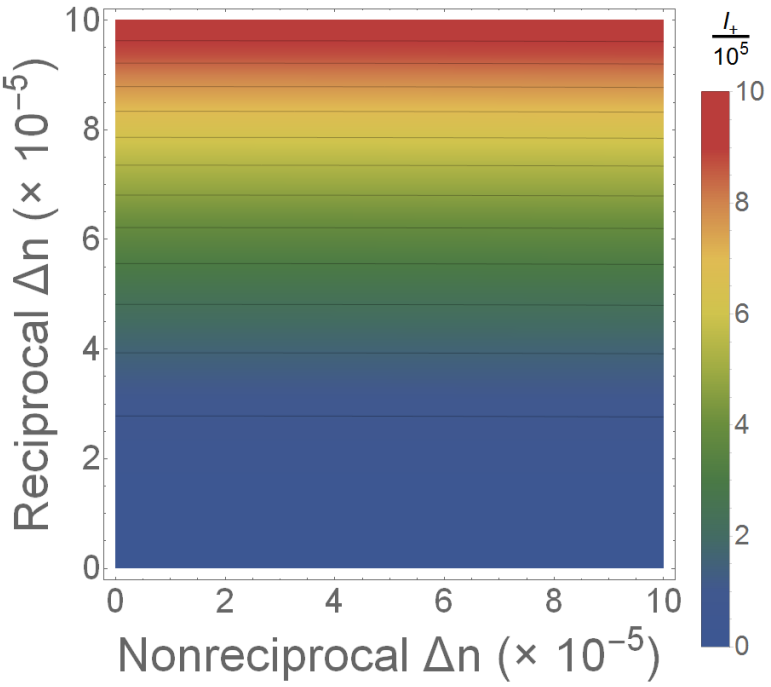

FIGURE 33. Bright port response to small perturbations.
A zoomed-in view of Figure 32. The near-horizontal contours suggest a strong response to reciprocal perturbations and, by comparison, a weak response to nonreciprocal phenomena.

the detuning of the alternate effect is held fixed at a constant detuning of $|\Delta n| = 10^{-7}$. In this port we observe a reciprocal sensitivity orders of magnitude larger than the nonreciprocal sensitivity. At a nonreciprocal detuning near 10^{-5} there is a transition in the bright port nonreciprocal sensitivity from one slope to another and the sensitivities begin to converge. This magnitude detuning is approximately where the nonreciprocal detuning increases the phase difference at the interferometer output sufficiently, such that the bright port moves from destructive back to constructive interference. However, the phenomena that is of interest for sensing applications will occur in the region of small Δn where the sensitivity difference is roughly five orders of magnitude. This enables clear detection of reciprocal effects using the bright port. In combination with the results for the dark port, this opens new avenues of

simultaneous detection utilizing SPR. While current detection schemes are capable of detection of one or the other type of perturbation, a resonantly enhanced Sagnac is capable of concurrent monitoring of both. For example, one could monitor both the concentration and magneto-optic properties of a magnetic fluid in the vicinity of the metal film.

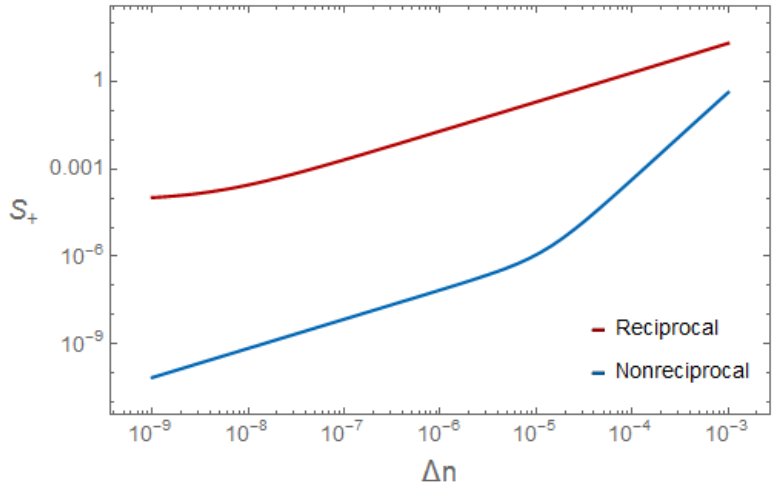

FIGURE 34. Reciprocal and nonreciprocal sensitivity in the bright port. The reciprocal sensitivity is plotted for reciprocal Δn varied and a constant nonreciprocal detuning of $|\Delta n| = 10^{-7}$. For the nonreciprocal sensitivity curve, Δn is the magnitude of the nonreciprocal detuning and the reciprocal detuning is held fixed at 10^{-7}.

Persistence of Results

In simultaneous detection experiments, the strength of both types of perturbations may exceed the $|\Delta n| = 10^{-7}$ value that was used to hold one type of perturbation constant in the previous calculation of the sensitivity. To explore the persistence of this large gap in sensitivity, we repeat the calculation described above, but while increasing the magnitude of the Δn held constant. Figure 35a shows the bright port sensitivity with this parameter set to 10^{-6} and Figure 35b shows the bright port sensitivity with this parameter set to 10^{-5}. By comparison of these plots with

Figure 34, we observe the same qualitative features but note that the gap between the reciprocal and nonreciprocal sensitivity does decrease slightly. For reciprocal sensitivity with $|\Delta n|$ nonreciprocal held fixed at 10^{-5} and nonreciprocal sensitivity with Δn reciprocal also held fixed at 10^{-5}, the sensitivity difference has shrunk to approximately four orders of magnitude. However, the fact that a sizable gap persists between the two suggests that, for simultaneous detection, even while the strength of a nonreciprocal perturbation increases, the reciprocal sensitivity dominates the response of the bright port.

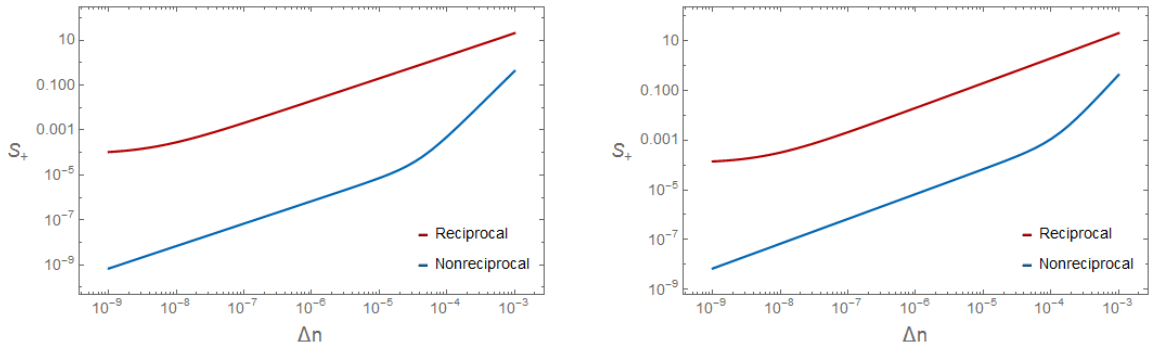

FIGURE 35. Bright port sensitivity for simultaneous detection. (a) Same as Figure 34 except that the $|\Delta n|$ not varied is held fixed at 10^{-6}. (b) Same again, but now with the $|\Delta n|$ not varied is held fixed at 10^{-5}.

A second modification considered is that of the thickness of the silver film. In the prior calculations the film thickness is assumed to be the critical thickness which achieves identically zero reflectance at the resonance minimum. In practice, experimental limitations will preclude the realization of a film at exactly this thickness. To account for this, we explore the sensitivity of the bright port for films other than the critical thickness. Figure 36 shows both the reciprocal and nonreciprocal sensitivity for film thicknesses 3 nm greater than critical in panel (a) and 6 nm greater in panel (b). As in the case of the critical film thickness, the

discrepancy starts out larger for smaller detunings and decreases as the strength of the perturbation increases. For these supercritical thicknesses, the gap closes sooner, starting at five orders of magnitude initially and dropping to one order of magnitude difference at around $\Delta n = 10^{-5}$. There still exists a region over a range of parameter values in which the response to reciprocal phenomena is multiple orders of magnitude greater. However, if greater precision of film thickness is necessary in order to achieve sufficient sensitivity contrast, other deposition techniques such as epitaxial growth of single crystalline films may be considered [82, 83].

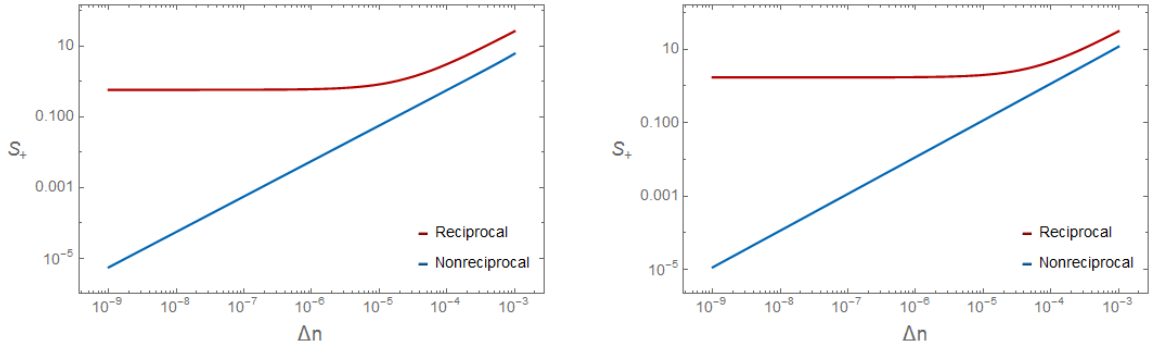

FIGURE 36. Bright port sensitivity for supercritical thickness. (a) The reciprocal and nonreciprocal sensitivity are plotted for a silver film thickness 3 nm greater than the critical thickness. (b) The reciprocal and nonreciprocal sensitivity are plotted for a silver film thickness 6 nm greater than the critical thickness. In both cases, a similar disparity exists initially, but lessens more quickly for larger perturbations.

Angular Detuning

In the previous interferometer output results, the angle of incidence onto the silver film from within the prism is taken to be precisely at the reflectance minimum of SPR. However, in some instances a choice could be made to detune this angle slightly above or below the resonance angle. Although the slope in the phase profile decreases as we shift away from the resonance minimum, the slope of the reflected intensity

increases up until reaching the inflection point. Furthermore, the reflected intensity itself will increase with this angular detuning leading to a larger normalized intensity in the bright port. A particular angle of interest may be that which maximizes the slope of the intensity. After computing this angle, we may use it in a similar fashion as above to construct density plots which display the bright and dark port response to both reciprocal and nonreciprocal perturbations. This computation confirms a nonzero bright port signal even in the balanced interferometer configuration, as can be seen by inspection of the scale bar in Figure 37. Beyond this distinction, the qualitative behavior of this figure remains much the same as that of the system without angular detuning. The nearly horizontal contours suggest a strong response to the introduction of reciprocal perturbations, and by comparison very little response to the presence of nonreciprocal perturbations continuing out to Δn of nearly 10^{-3}.

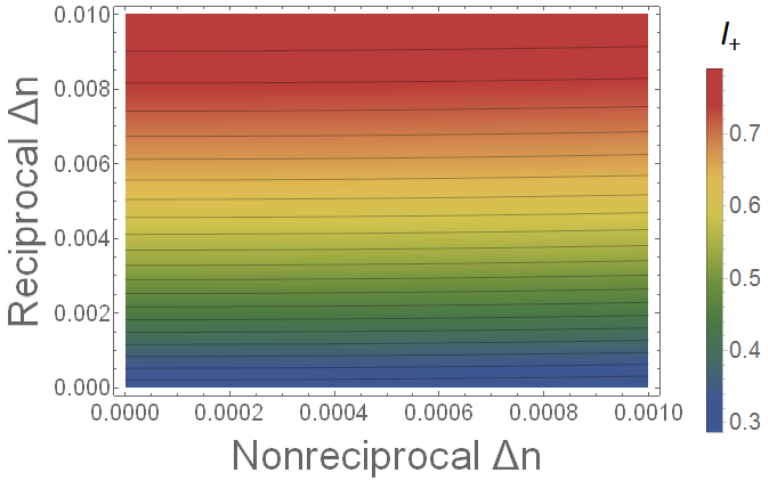

FIGURE 37. Angle detuned bright port intensity.
Normalized output intensity is plotted as a function of both reciprocal and nonreciprocal perturbations. The incidence angle is fixed at the angle which maximizes the slope in the surface plasmon reflectance.

The dark port, on the other hand, maintains perfectly destructive interference under ideal conditions such that the intensity at this output remains zero for the

balanced interferometer, even with the angular detuning. Figure 38 displays the normalized intensity as a function of both reciprocal and nonreciprocal perturbations. The intensity contours in this plot are nearly vertical, representative of a response dominated largely by the introduction of nonreciprocal perturbations. This holds for reciprocal perturbations in Δn on the order of roughly 10^{-4}. As a point of reference, this corresponds to a temperature change of approximately 1 $^{\circ}C$ in liquids pervasive in scientific research such as water and ethanol.

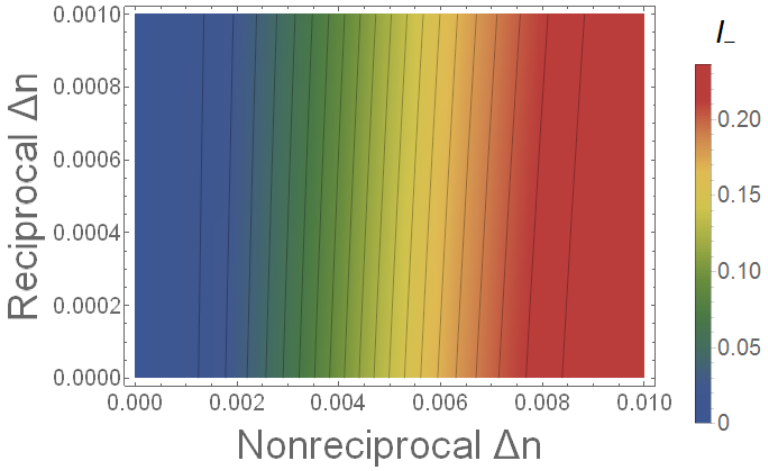

FIGURE 38. Angle detuned dark port intensity.
Normalized output intensity is plotted as a function of both reciprocal and nonreciprocal perturbations. The incidence angle is fixed at the angle which maximizes the slope in the surface plasmon reflectance.

The foremost conclusion to be drawn from this discussion is that the results obtained above are not exclusive to the resonance angle itself. The propensity toward detection of reciprocal effects in the bright port and nonreciprocal perturbations in the dark port holds true for additional angles of incidence away from the resonance minimum. The nonzero bright port signal in the balanced interferometer represents a departure from the earlier conclusions, nonetheless the residuum of the behavior remains qualitatively the same.

Summary

The overall response of both the dark and bright ports of the interferometer is succinctly summarized, with the response attributed to either intensity or phase perturbations, in Table 2. The outputs displayed here were generated from the interference equations, irrespective of the surface plasmon or any other particular resonance. The equations were modified by introducing a small change, δ, directly to each of the parameters that represent a round trip intensity transmission coefficient or total accumulated phase for both the clockwise and counter-clockwise paths, rather than indirectly through a refractive index shift, Δn, as before. A reciprocal intensity change, ΔI, was introduced by adding nonzero δ of the same sign and magnitude to the round trip intensity transmission coefficient of the two paths; a nonreciprocal intensity change by changing the sign of δ for one of the paths. Similarly, a reciprocal phase change, $\Delta\phi$, was introduced by adding nonzero δ of the same sign and magnitude to the total accumulated phase in both paths; a nonreciprocal phase change by adding δ of the same magnitude but opposite sign. In reality, a perturbation is likely to affect both the intensity and the phase of the system; however, here the two were considered independently.

TABLE 2. Interferometer response to reciprocal and nonreciprocal effects.

	Reciprocal	Nonreciprocal
ΔI	I_-: constant	I_-: increase
	I_+: increase	I_+: decrease
	$I_- + I_+$: increase	$I_- + I_+$: constant
$\Delta\phi$	I_-: constant	I_-: increase
	I_+: constant	I_+: decrease
	$I_- + I_+$: constant	$I_- + I_+$: constant

In this scenario, the dark port signal remains constant in the presence of any reciprocal perturbation and responds solely to nonreciprocal phenomena. Though the dark port displays no reciprocal response, the bright port enables monitoring of reciprocal intensity perturbations. And while it also responds to nonreciprocal perturbations, the reciprocal response in the bright port overpowers the influence of nonreciprocal phenomena.

For most any perturbation, Table 2 shows that the sum of the two interferometer intensities, $I_- + I_+$, remains constant. The exception is a reciprocal intensity change, where movement along the resonance has altered the overall circulating intensity within the interferometer. Whether this leads to an increase or decrease in the bright port signal, and hence the sum, depends on the type of resonance and how it is employed. For example, when using SPR aligned at the reflectance minimum, a reciprocal ΔI will couple less strongly to the surface mode and lead to an increase in signal, as is displayed in the table. On the other hand, if the system maximizes transmission through a medium exhibiting electromagnetically induced transparency (EIT), small perturbations could instead cause a decrease of signal.

In this chapter, we have developed a theoretical model which facilitates modeling the introduction of perturbations, both reciprocal and nonreciprocal, to a resonantly enhanced ring interferometer and computing the output response. The results of this model point toward a dark port signal which is highly sensitive to nonreciprocal phenomena and comparatively insensitive to reciprocal perturbations. Conversely, the bright port signal is found to be dominated by sensitivity to reciprocal effects. These results are robust to variation in the film thickness or resonance angle and to the presence of competing effects. The end result is a device which appears well-suited for the simultaneous detection of both nonreciprocal and reciprocal phenomena.

CHAPTER V

EXPERIMENTAL IMPLEMENTATION AND RESULTS

Overview

This chapter describes the construction of an experimental apparatus and experimental results obtained from that device in an effort to support the results of the theoretical modeling described in the prior chapter. We begin with a discussion of the optical configuration, noting the components used and relaying the methods for alignment of the interferometer. We then describe the experimental means by which we introduce the perturbations to the system and the components needed to carry out this procedure. We next present experimental results for detection of reciprocal ohmic heating in the bright port. The data qualitatively matches the model of the previous chapter but falls short quantitatively due to some logistical constraints. After that, we present experimental results toward detection of nonreciprocal plasmon drag in the dark port. A signal is observed with some characteristics matching those our model but other features which appear in conflict with our expectation; a full understanding of these observations is left unresolved. Finally, we discuss the prospects of simultaneous detection and summarize the results of this chapter.

Configuration and Alignment

Incorporating the surface plasmon resonance system into the Sagnac interferometer introduces a few additional experimental considerations to take into account when building the resonantly enhanced interferometer. One such consideration pertains to the angle of incidence of the light beam upon the prism. In a

typical Sagnac, the angles the beam makes with the reflecting elements are not crucial; the important alignment issue is simply that the paths of the counterpropagating beams overlap. However, due to the narrow angular width of the resonance and the desire to probe a particular location along that resonance, the incident angle of the laser beam upon the prism must be set precisely in this configuration. In the initial alignment of the system, two mirrors and a right angle prism are configured according to the schematic shown in Figure 39. The initial alignment is relatively straightforward to implement and is aided by use of the rectangular grid of the optical table and the back reflections from the lateral faces of the prism for alignment. The motorized rotation stage holding the prism is zeroed while the back reflection from the lateral face is aligned to pass back through the iris from which it came. The second mirror is then positioned to close the loop, with final adjustments made by projecting the dark port output onto a blank sheet. A micrometer dial is used to precisely control the tilt of the mirror until maximum cancellation of the signal in achieved in the dark port. This will be limited by the imbalance of the beamsplitter split ratio, as discussed previously. The end result of this initial alignment procedure is 45 degree incidence on the back of the prism from both directions; the configuration must then be modified to achieve the desired angle dictated by the location of the surface plasmon resonance.

In the first iteration of the experimental setup constructed in the lab, the general configuration chosen was a symmetric one, as shown in the schematic of Figure 40, with the two mirrors mounted on rotation stages and the prism configuration affixed to a translation stage oriented diagonally with respect to the grid of the optics table. It is symmetric in the sense that the incidence angle upon both mirrors is identical and the counter propagating beams travel the same distance before exciting

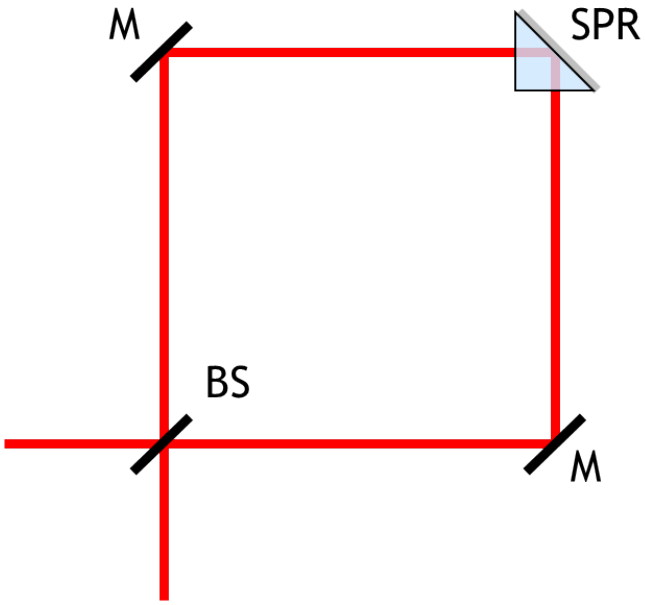

FIGURE 39. Initial alignment of the interferometer
The initial angles are set by zeroing the rotation stage below the prism while the back reflection from the lateral face of the prism travels directly back along its incident path. The second mirror is positioned to close the loop with a micrometer used for fine tuning to achieve the lowest possible signal in the dark port.

propagating plasmons along the metal and dielectric interface. The alignment of this configuration was executed first by rotating the two side mirrors to the same desired angle followed by a translation of the prism configuration such that the hypotenuse is aligned with the point where the two beams intersect. The intensity of the beams at their intersection is large enough that the beam spots are visually discernable on the back of the prism, facilitating the alignment procedure by allowing for initial alignment by eye and fine tuning of the alignment by inspection of the interferometer outputs. In practice, this procedure proved to be tedious in that it often required an iterative process to achieve alignment at the desired angle and also did not allow for easy characterization of samples to determine the thickness and dielectric properties of the silver films as deposited.

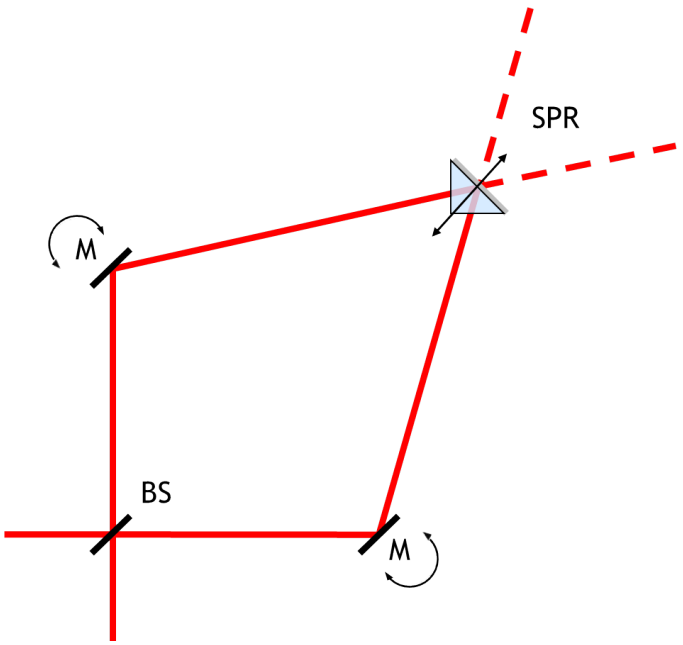

FIGURE 40. A symmetric configuration for alignment at the desired angle. This configuration is aligned first by equal rotation of the two mirrors followed by translation of the SPR prism mount to close the beam paths. While it maintains an inherent symmetry of the system, it does not facilitate seamless optical characterization of silver films.

Instead, the optical configuration was modified to achieve the form illustrated in Figure 41. In this conformation, one of the mirrors remains fixed, both in location and orientation, with the beam reflected from this mirror directed toward the prism configuration. The prism is mounted on a motorized rotation stage which can be adjusted to achieve the desired angle of incidence within the prism without disturbing the position of this first mirror. The motor angle is set to provide the desired incident angle using the relation between the two described in an earlier chapter. Once positioned appropriately, the beam reflected from the SPR configuration will cross paths with the portion of the input beam which is initially transmitted through the beamsplitter. The second mirror is then translated such that the plane of the surface of the mirror contains this intersection point of the beams, and the mirror is rotated such that the counterpropagating paths of the interferometer overlap entirely. This

gives rise to a certain asymmetry between the paths, as one beam travels a shorter path to reach the interferometer; however, this difference in length is compensated on the return trip to the beamsplitter, thus, maintaining equivalent phase accumulation in the paths and not disrupting the symmetry of the interferometer as a whole. Additionally, the difference in travel time from the beamsplitter to the prism for one path compared to the other is less than one nanosecond, a timescale much smaller than that of any of the perturbations to be studied in this dissertation.

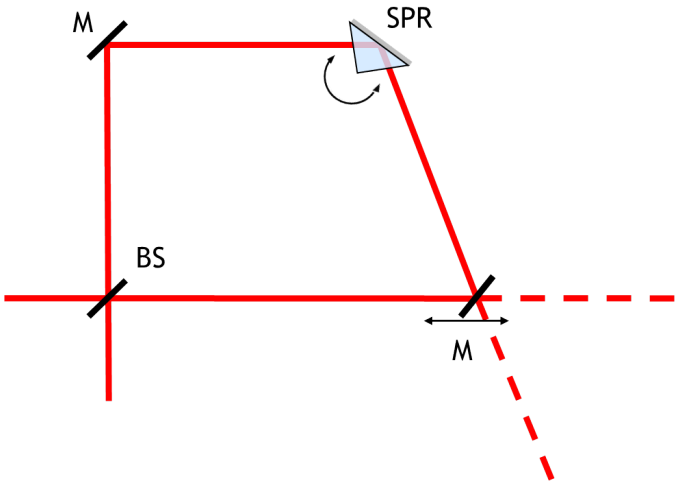

FIGURE 41. An asymmetric configuration for alignment at the desired angle. This configuration fixes entirely the position of one of the mirrors and includes a rotation stage for the prism to achieve the desired angle of incidence. The second mirror is then positioned to close the interferometer loop. While not symmetric in the same manner as the prior system, it does maintain equivalent optical path lengths while also facilitating seamless optical characterization of silver films.

One potential drawback to the alignment of this configuration is that the beam reflected from the prism, if aligned to the minimum of the resonance, can be difficult to observe visually due to the largely diminished intensity. This can affect the alignment of the second mirror, though the problem can be mitigated through exploration of other avenues, such as the interference pattern at the output, to perform the fine tuning of the alignment. On the other hand, an overwhelming success of this

configuration is the simplicity of achieving the desired angle with one simple rotation of the prism and, subsequently, the ease with which it allows for characterization of samples.

When characterizing a sample, the beam transmitted by the 50/50 beamsplitter is blocked so that only a single beam is incident upon the prism configuration. The motorized rotation stage on which it is mounted can be programmed through LabVIEW to methodically vary the incidence angle through a specified range. The reflected beam is diverted toward a silicon photodetector by placing an additional mirror within the interferometer beam path. The diverted beam is further redirected by a combination of two lenses positioned precisely to enable an angular scan without need for repositioning the detector. The first of two lenses is placed a cumulative distance of a focal length away from the spot on the back of the prism from which the reflected beam originates. This positioning generates a beam normal to the plane of the lens upon exit from the lens. A second lens is then positioned parallel to the first and a focal length away from the detector so that the beam incident on this lens is refracted toward the detector. The distance between the lenses is inconsequential because the beam traverses this segment normal to the plane of both lenses. This setup enables an angular scan over a range of nearly ten degrees, limited primarily by the size of the optical elements used.

This interferometer configuration is the pivotal part of a larger optical setup shown schematically in Figure 42, and as configured on the optical table in Figure 43. The optical source used is a 5 mW HeNe laser (JDS Uniphase model 1125/P). The output beam from this source first passes through an optical isolator (OFR IO-3D-633-VLP), which eliminates optical feedback and maintains the stability of the source. After redirection of the beam with 1" mirrors, a spatial filter (Newport Model 900)

is used to eliminate high k spatial frequency components. The Airy pattern output produced by the pinhole of the spatial filter is filtered by an iris with aperture set at approximately 1 cm, large enough to select the central bright spot. This cleaned-up beam is then telescoped down to roughly 2 mm beam diameter using a configuration of Newport AR.14 anti-reflection coated lenses. Just prior to the interferometer is a linear polarizer (Newport 10GT04AR.14) to reinforce the p-polarization of the beam and a beamsplitter with roughly 15:85 (R:T) split ratio for HeNe wavelength (Newport 10RQ00UB.2). This beamsplitter is used both as a reference to monitor the input beam for intensity fluctuations and to divert the bright port signal for detection upon its exit from the interferometer. After this beamsplitter is a second, non-polarizing, laser line, 50/50 beamsplitter (Newport 10B20NP.25) used to split the beam into two components which then begin their trips around the interferometer. These two beams reflect off silvered 2" mirrors and cross at the hypotenuse of a BK7 right angle prism (Thorlabs PS911), incident at an angle beyond the critical angle for total internal reflection of a glass and air interface. The prism is mounted on a motorized rotation stage (Newport URS75CC) driven by motor controller (Newport ESP300). The beam is modulated at 911 Hz by optical chopper (Thorlabs MC1000). The output and reference signals are collected with a silicon photodiode (Thorlabs DET36A) or photomultiplier tube (Hamamatsu R955), depending on the level of intensity, each of which is connected to a Lock-In Amplifier (SR810) with a 50 Ω terminating resistor for impedance matching. All motor control and data collection are integrated with the LabVIEW software so the experiments may be run easily through the laboratory computer.

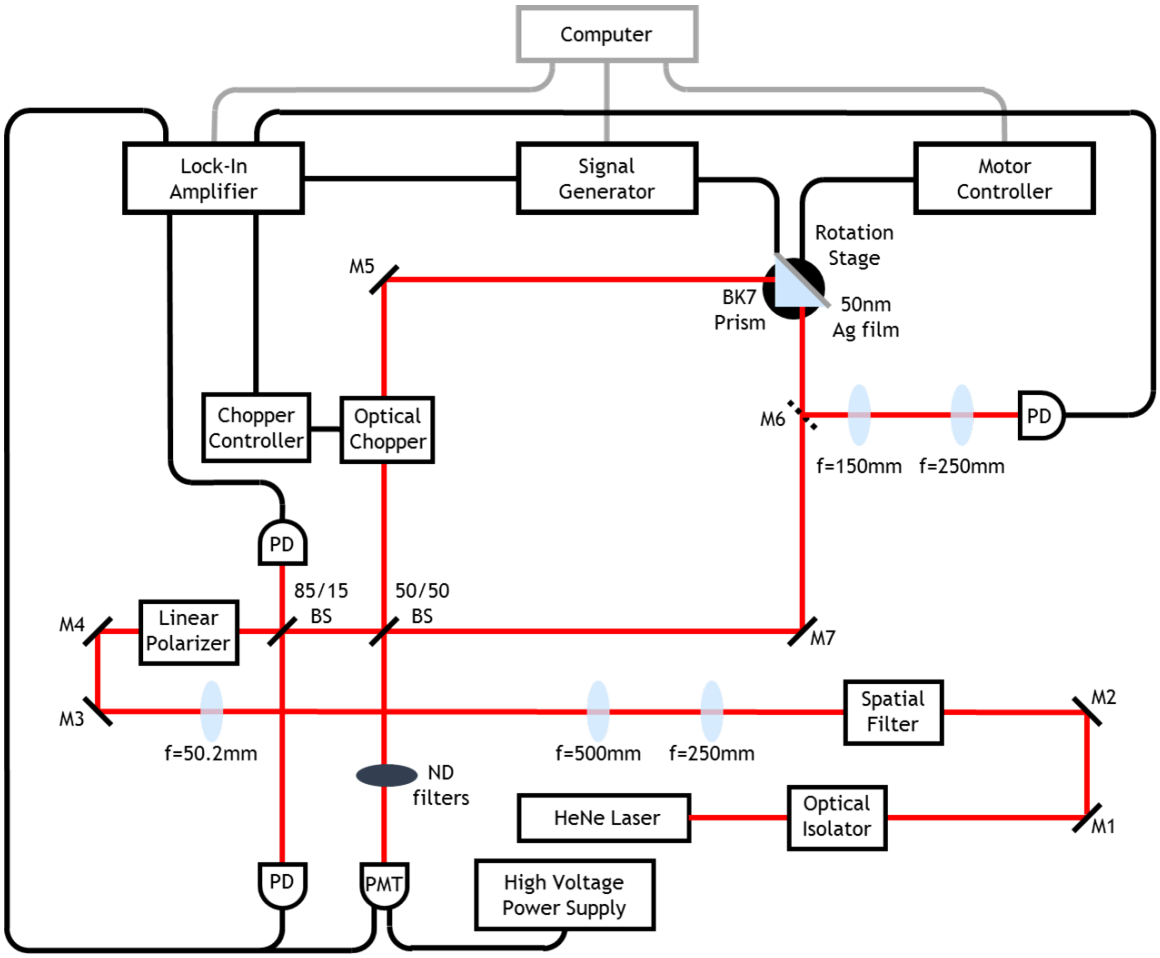

FIGURE 42. Schematic of full experimental configuration.

Perturbation Implementation

With the optical configuration assembled, the next step toward experimentally investigating the findings of the previous chapter is to choose a method through which the reciprocal and nonreciprocal perturbations may be enacted upon the physical system. For this work, a choice was made to implement these perturbations by application of an electrical current across the silver film which supports the propagation of SPPs. This decision was made due to the ability of the current to simultaneously produce both types of perturbations, and also because of the minimal

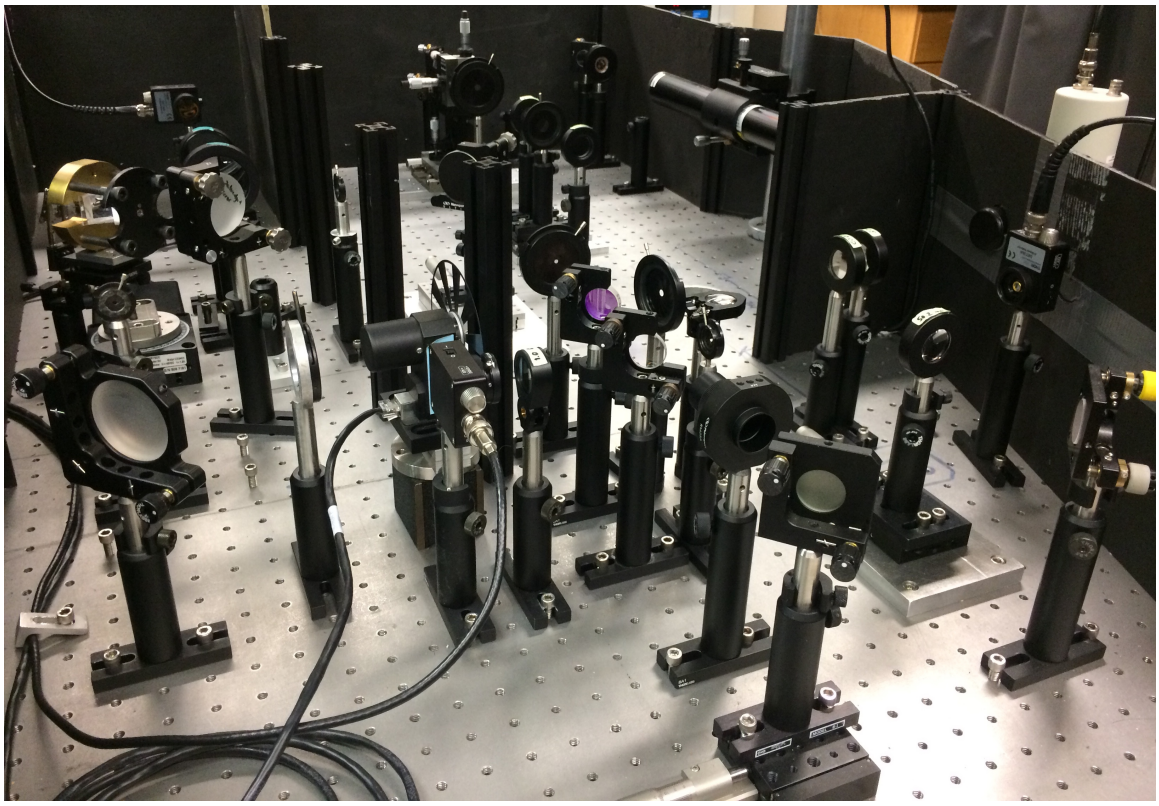

FIGURE 43. Experimental configuration as constructed in the laboratory.

extra equipment and cost associated with pursuit of this route. The presence of a current through the silver film leads to ohmic heating, which will then drive a temperature change in the layered film system. This, in turn, will generate an optical response at the interferometer output owing to the thermo-optic coefficient of the relevant material, which describes the refractive index response of the material to a change in temperature. As this will impart equivalent phase accumulation on the interferometer paths, independent of the direction of propagation, this thermal induced heating will manifest as a reciprocal perturbation within the system.

In addition to generating heat, the electric current in the film is also expected to give rise to a nonreciprocal dragging effect. The presence of the current breaks a symmetry of the system and sets up a preferred direction of electron motion within

the silver film. The SPP propagation direction will then be parallel to the direction of the electric current for one path around the interferometer and antiparallel for the counterpropagating path. This is expected to produce a relativistic dragging effect referred to as plasmon drag, which acts somewhat analogous to that of the Fresnel-Fizeau drag effect experienced by a beam of light traveling through a moving dielectric [84]. This perturbation is presumed to manifest as a difference in phase accumulation of the two beams around the path and, therefore, result in an interferometer response as predicted in the previous chapter for a nonreciprocal perturbation.

In practice, this electrical current is implemented by affixing short wire segments to both ends of a deposited metal film with a two-part, high conductivity, silver epoxy. The newly attached leads add only a small bit of additional resistance; the film with leads is measured to have resistance on the order of 10 ohms, with some variability owing to slight differences in the actual dimensions of the deposited silver film. The electric current is supplied to the film by connecting the leads to either a power supply or a function generator, with the latter capable of supplying a variety of pulse shapes. If desired, a current limiting resistor can also be added to the system to allow for further control of the current. The magnitude of the current passing through the system can be measured by insertion of an ammeter into the electronic circuit.

After a two hour cure time for the silver epoxy, the sample may be put to use within the optical system. The glass substrate, with vapor deposited silver film and cold soldered wire leads, is affixed to the back of a prism with the metal film facing outward, away from the prism. A refractive index matching liquid is used to eliminate any refractive air gaps between the prism and glass slide. This prism, now with metal film attached is placed within a prism mount fabricated by a prior graduate student,

Lawrence Davis, schematically shown in Figure 44 [44]. The micro-volume enclosed dielectric cavity and close proximity of the thermometer to the dielectric are the desired features motivating the use of this apparatus; however, a few modifications are made for this experiment. In order to prevent electrical contact between the silver film and brass mass, a layer of plastic cling wrap is situated so as to provide physical separation between the two. Also, rather than filling the cavity with a liquid, it is comprised of ambient, room temperature air. The enclosed system provides a stable environment for the air and limits the formation of an oxide layer on the silver film. In addition, the heater resistor is unused as the heat for this experiment will be generated by a current in the silver film itself.

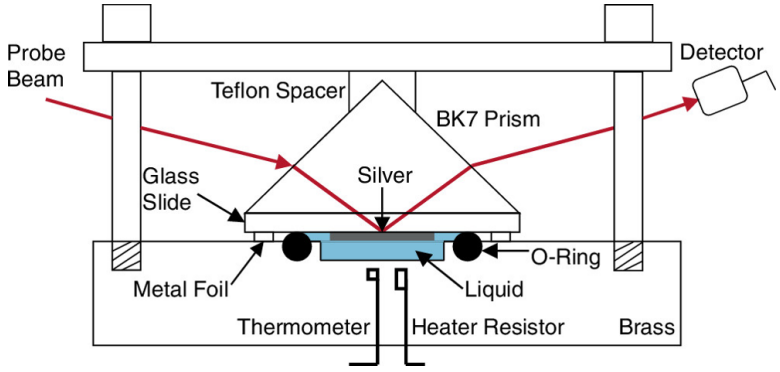

FIGURE 44. Diagram of the SPR prism mount used by L. J. Davis. This image was taken from reference [44]. The setup was modified for this experiment by filling the reservoir with air rather than liquid, removal of the heater resistor, and use of plastic cling wrap in place of metal foil.

The prism, now in the prism holder, can then be mounted on the rotation stage and aligned within the optical system as described above. Using the configuration for sample characterization, an angular reflectance measurement is performed to observe the surface plasmon resonance and a least squares fit to the optical data is executed to obtain the sample specific material parameters. From there, the motor angle can be set to probe the desired location along the resonance, whether that be at the

resonance minimum or some other off-resonant angle. The mirror redirecting the beam for characterization is then removed and the remaining interferometer mirror positioned to align the interferometer, first but translating it so that the counter propagating beams meet at the mirror surface and then by adjusting the angle so that the paths fully overlap. At this point the system is set up and ready to perform experiments.

Reciprocal Ohmic Heating in the Bright Port

We begin our discussion of experimental results obtained from the resonantly enhanced interferometer with optical data collected from the bright port. While applying a current in the silver film, the temperature of the film and its surroundings increases in response to ohmic heating. Then, according to the thermo-optic coefficient which describes the material, the refractive index shifts as a result of the increased temperature. As discussed in the previous chapter, this will manifest most strongly as a response in the bright port signal. In order to verify that a response in the output signal can be traced to temperature increase of ohmic heating, an independent measure of temperature is collected by placing a thermometer in the location as shown in Figure 44, 250 μm from the back of the air-filled cavity. In order to more strongly observe the response of the interferometer to temperature change, the angle of incidence within the prism is set to the angle of maximum slope on either side of the resonance. For the particular sample under investigation those angles are found to be 42.92° and 43.12°. The locations of these angles with respect to the resonance are indicated in Figure 45. In order to heat the sample quickly and reduce time of the experiment, a potential difference of five volts is applied across the metal film resulting in a direct current of approximately 175 mA. In future applications of

this device, temperature fluctuations may be a side effect of some other phenomena under investigation and vary more slowly than the time scales resulting from this particular procedure. However, here we aim for a proof of principle result to show that the bright port responds to change in temperature and, thus, may be used to monitor temperature change, or other effects similar in nature, while performing interferometric measurements.

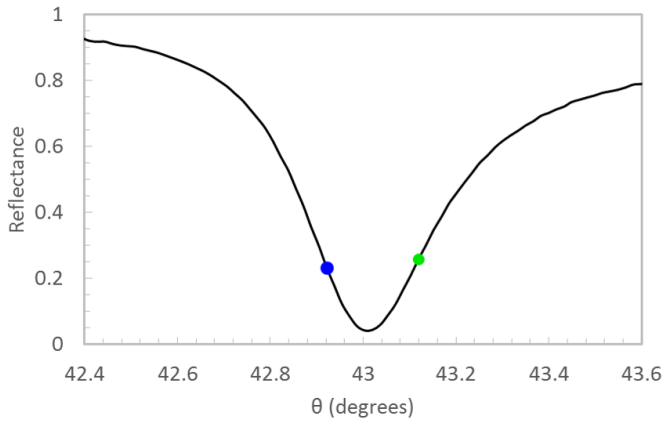

FIGURE 45. Angles of incidence used in bright port data collection. The black trace represents the normalized angular reflectance data collected from the sample. The blue dot indicates 42.92° while the green dot corresponds to 43.12°. These correspond to approximately the angle of maximum slope on either side of the resonance curve.

The data collection for this experiment is automated and run by LabVIEW software. When the potential difference is applied across the silver film, the time, temperature, laser reference signal, and bright port signal are recorded on the computer at regular time intervals as the system heats up. The recorded time is, for the most part, inconsequential for this experiment as we are primarily concerned with the temperature at that particular moment and not how long it took to reach that temperature. The recorded time stamps will serve a greater purpose in the experiments to come, particularly when probing the nonreciprocal perturbations. The laser reference signal is collected to be used in the normalization of the bright

port signal, accounting for any fluctuations in the intensity of the input beam. The normalized bright port data is sorted by temperature with bin sizes of 0.1°C, the nominal resolution of the thermometer used. Data are then averaged to find the mean bright port signal at a given temperature and the standard error is computed for that set of data points. This data is plotted for the incidence angle of 42.92° in Figure 46a. A linear fit to this data is performed with the resulting equation displayed in the plot legend. This data can then be compared with the theoretical model using the results from the previous chapter.

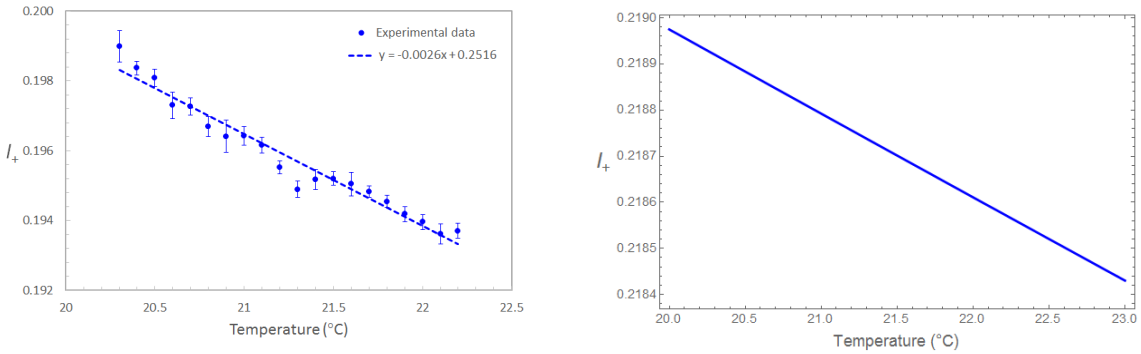

(a) (b)

FIGURE 46. Bright port response to reciprocal ohmic heating for θ =42.92°. (a) Normalized experimental optical data with error bars to indicate the standard error. The dotted line represents a linear fit to the data with the equation shown in the legend. (b) Theoretical model of the same scenario using a temperature dependent refractive index of air.

This experimental process is modeled theoretically using the normalized output intensity equations presented earlier. The surface plasmon reflectance term is computed using the sample-specific material parameters for that particular silver film obtained from a least squares fit to the angular reflectance data of Figure 45. In this model, we consider only the thermo-optic behavior of the dielectric, air in this case. The temperature dependent refractive index of the air is calculated based on an

updated Edlén equation from Birch and Downs[85]. The result of this model, plotted across the range of temperatures observed experimentally, is displayed in Figure 46b.

By comparison of experiment with the theory, we first observe that the normalized values of the theoretical model differ from the experimental data by approximately 10%. To account for this discrepancy, we consider a few potential contributing factors. First, while our best efforts were made toward alignment of the beams it is feasible that there exists some residual misalignment. This would result in less than perfectly constructive interference, even beyond the limit set by beamsplitter imbalance, and lower the values of the experimental data, as is observed. Secondly, this discrepancy may also be in part due to the methods used for normalization of the data. The signal was normalized to the bright port measurement with the interferometer aligned to an angle just beyond the angle of total internal reflection. This accounts for losses in the system but assumes they are constant with angle; angular dependencies of loss mechanisms such as reflections from optical components will introduce a small error to the normalized bright port signal when aligned at other angles. In addition, the refractive index values used for the dielectric material may not accurately describe the air used in this experiment owing to reasons such as differences in composition, for one. Despite the discrepancy in the value of the normalized output, it is instructive to compare the slopes, as this gives an indication of the output response to temperature change.

Visually, we observe that the sign of the computed slope matches that of the experimental data. In comparing the magnitudes of the slopes we find that the theoretical slopes is smaller than the experimental by just more than a factor of ten: 0.00018 for the theoretical and 0.0026 for the experimental. Another way of stating this is that, based on these values for 42.92° incidence, a change in the normalized

reflectance of 0.001 corresponds to an independently measured temperature change of about 0.4°C. Conversely, the theoretical model predicts that, for the material parameters used, the same change in reflectance requires a temperature change of 5.5°C.

This same discrepancy exists in when the interferometer is aligned on the higher angle side of the resonance, at an angle of 43.12°. The data collected for this angle is shown in Figure 47a along with a linear fit to the data. The sign of the slope in the temperature data is opposite that of the previous data set due to the change in sign of the slope across the resonance itself. The theoretically modeled values for this angle are shown in Figure 47b. Again we observe that normalized intensity values are greater in the theoretical depiction. Comparing the slopes, we again observe an order of magnitude difference, 0.00014 for the theoretical and 0.0021 for the experimental, predicting a larger temperature change than is experimentally measured.

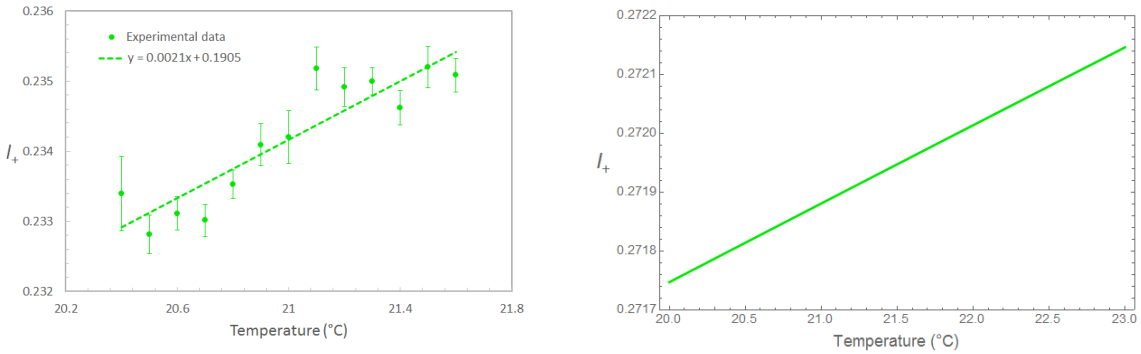

(a) (b)

FIGURE 47. Bright port response to reciprocal ohmic heating for θ =43.12°. (a) Normalized experimental optical data with error bars to indicate the standard error. The dotted line represents a linear fit to the data with the equation shown in the legend. (b) Theoretical model of the same scenario using a temperature dependent refractive index of air.

However, recall that the SPR sensing techniques probe the immediate vicinity of the interface, with SPP field penetration depths on the order of hundreds of

nanometers. It is possible that the actual temperature change experienced by the few hundred nanometers of material in the immediate vicinity of the interface is closer to the higher, theoretically predicted temperature than the lower value measured experimentally. In any case, we expect the measured temperature to be an underestimate of the actual temperature change experienced at the interface due to the difference in location of the temperature measurement as performed by the optical technique and independently by the thermometer. The thermometer is positioned .25 mm from the base of a 0.4 mm dielectric reservoir as indicated in Fig. 44. This amounts to a 0.65 mm total displacement from the source of the heat, the silver film. At a minimum, we can use this measured change in temperature to set a lower bound. Toward further resolving this discrepancy, one avenue of investigation would be to perform a transient heat transfer analysis and solve the temperature distribution in the system providing a relation in temperature between the two locations of relevance. A second consideration is that the model accounts only for a change in the refractive index of the dielectric. A thermo-optic analysis of the remaining constituents, such as the silver film, could be added to the model. That being said, this result does act in support of the general conclusion that the bright port of the resonantly enhanced Sagnac exhibits sensitivity to reciprocal perturbations. It is feasible that this output could be calibrated and optimized for use as a monitor of reciprocal phenomena, which could be done in conjunction with detection at the dark port, the next area of discussion.

Nonreciprocal Plasmon Drag in the Dark Port

We proceed to discuss our experimental probing of the dark port in search of response to nonreciprocal phenomena. In this experiment, the perturbation of interest

is introduced to the system in the same manner as that of the reciprocal ohmic heating, by applying a voltage across the silver film of the SPR configuration. This establishes an electric field within the silver giving rise to a preferred direction of motion for the electrons in the silver film. The beams of the interferometer then will excite SPPs, one of which has a propagation direction matching the direction of current flow in the silver and the other of which is counter to this flow. We expect to observe an electron-plasmon interaction similar to that of the plasmon drag effect in which there is a momentum transfer between the SPP mode and the electrons. Much of the previous work on this interaction pertains to the characterization of the electrical current induced by the optical interaction [84, 86–88]. The magnitude of the resulting current peaks sharply on resonance, where there is maximal coupling to SPPs, and the direction matches that of the propagating plasmons.

On the other hand, there is some precedent, but much less understanding, in the literature for observation of coupling in the opposite direction; where an applied electrical signal modifies an optical signal through interaction of the electrons with SPPs. In this intensity based measurement, application of a square wave pulse resulted in a SPR reflectance shift with timing to match that of the pulse [89]. After modeling the expected reflectance profile due to variation in the film thickness and permittivity, the authors concluded that, "the explanation of the observed phenomenon is beyond simple current-induced changes of the basic film parameters" [89]. Use of an interferometric scheme, by employing the SPR configuration within a Sagnac, for further exploration of this phenomenon has the potential to provide new details, including phase information, in order to better understand and describe this interaction between SPPs and electrons. Further insight into this interaction may

have broader impacts as well, as plasmonics are viewed as a potential intermediary between photonics and electronics in the area of information processing [90, 91].

To probe for nonreciprocal response in the bright port we utilize a function generator to drive an electrical current in the silver film while collecting the intensity output at the dark port with a photomultiplier tube and through use of a lock-in amplifier. Neutral density filters are used in front of the detector as necessary to avoid saturation. We choose to apply a square wave voltage and look for a modulation in the output at the same frequency. It is important that the square wave be vertically offset so that it is not centered around zero because alternation between positive and negative values of the same magnitude is not expected to elicit a response. This will flip the direction of the current, but in both cases SPPs will be propagating both with and against the current, producing the same phase difference in both scenarios. Here we use a square wave with a 5 volt peak-to-peak amplitude and 2.5 volt offset, as this +5 volts is the largest voltage capable of being produced by the function generator used. We expect the strength of the interaction to scale positively with the current in the film, in which case increasing the voltage will produce a larger response. A range of frequencies was examined, spanning from tens of kHz down to roughly tenths of mHz. The higher frequencies were analyzed via digital oscilloscope because the timing of the LabVIEW program subroutine, as written, was too slow to process this data in real time. Much of this search came up empty; a null result was observed in which the dark port signal did not vary on the timescale to match the input frequency, exhibiting only noise fluctuations. However, in some instances, a modulation of the dark port signal was observed. A more or less representative sampling of this data will be discussed and analyzed below.

Angle Greater Than Resonance Minimum

The results of one such data run are shown in Figure 48. For this data set, the incidence angle within the prism was fixed at an angle greater than the resonance angle, specifically 43.25°. An input voltage with frequency of 5 mHz was used as is shown in Figure 48a. We concurrently collect temperature data with the expectation that, as before, the current induced heat will raise the temperature of the system over the course of the experiment. This is indeed the case as is seen in Figure 48b.

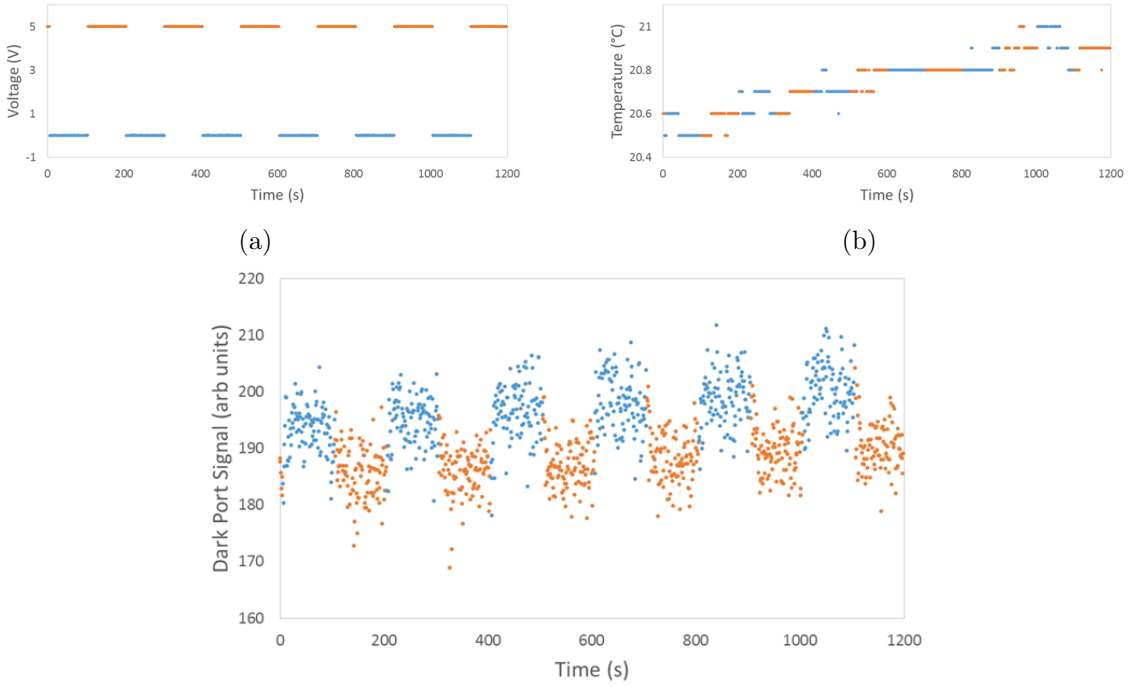

FIGURE 48. Dark port response to nonreciprocal plasmon drag. (a) Square wave voltage applied by the generator as a function of time. (b) Temperature recorded by the thermometer used for independent measure of temperature. A steady temperature increase is observed. (c) The dark port signal shows a modulated response with a frequency matching that of the applied voltage on top of a slight overall trend upward with time. Color is consistent throughout and used purely as a visual aid to distinguish low and high voltage regions.

In the dark port signal we observe a modulated response with a frequency matching that of the input square wave. The plot in Figure 48c is color coded to clearly demarcate the time intervals in which a voltage is applied across the silver film from those in which no voltage is applied. The signal in regions with no current is distinctly higher than it is in regions with voltage applied. In addition to this modulation, there is an overall upward trend in the data. This is attributed to the temperature change, which also increases steadily over the course of the data collection. While the dark port is generally impervious to the effects of temperature change, the presence of a nonreciprocal perturbation to break the symmetry of the paths does introduce a small sensitivity to reciprocal effects.

Qualitatively similar behavior can be reproduced using the theoretical model developed in the previous chapter. To account for the fact that the dark port intensity does not reach identically zero in experiment, we first introduce a disruption to the system which raises the baseline of the dark port signal to some nonzero value. Then, on top of that signal, we introduce two perturbations: one to model the reciprocal ohmic heating and a second to model the nonreciprocal plasmon drag. We observed in Figure 48b that the temperature of the system increased more or less linearly with time. For this reason, we introduce the reciprocal perturbation into the model simply as a linear increase in the refractive index of the dielectric. For the nonreciprocal perturbation, we assume, as a first pass, a current induced change to the real component of the relative permittivity of silver. We enter this into the model with a frequency matching that of the applied voltage in the experiment. When no voltage is applied across the film, no adjustments are made to the permittivity of silver. But when a voltage is applied, we model this as a nonreciprocal change in the permittivity: the permittivity increases as seen by one path and decreases as experienced by the

counterpropagating path. With some adjustment to the magnitude of the two effects entered into the model, we obtain the plot shown in Figure 49, which exhibits behavior qualitatively similar to the data of Figure 48c.

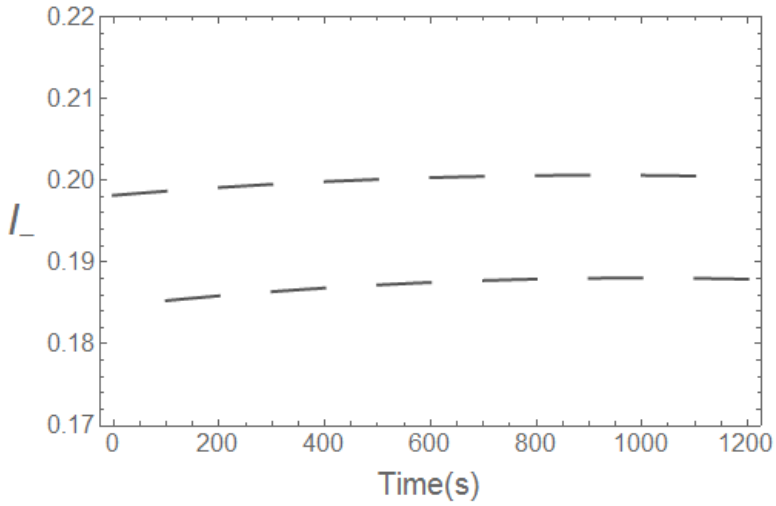

FIGURE 49. Dark port model of plasmon drag.
We use the theoretical model to introduce a nonreciprocal perturbation to the real component of the silver permittivity at a frequency of 5 mHz and a reciprocal perturbation to the dielectric that grows linearly with time. This produces qualitatively the same behavior as observed in the experimental data.

For just one trace, there are likely multiple sets of fit parameters which could used to match the data fairly well with experimental observation. However, if we are able to build up a repository of data collections, spanning the parameter space of incidence angle and magnitude of the applied voltage, we may be better able to pin down a set of fit parameters which describe the experimental data. This will likely involve moving beyond our assumption of nonreciprocal perturbation manifest only in the real component of the silver permittivity, and expanding it to also involve other parameters such as the imaginary component or the thickness. While this output appears suggestive of a nonreciprocal dragging effect, and the theoretical model can

be employed to reproduce similar qualitative behavior, further measurements are necessary to fully characterize the interaction.

Angle at Resonance Minimum

We next move to a data set collected with the angle aligned at the resonance minimum. A square wave signal output from the function generator is again used to apply and remove a 5 volt potential difference across the silver film with a frequency of 5mHz. The dark port data associated with this measurement, shown in Figure 50, again displays a modulated response with frequency matching that of the input signal. However, a striking difference is observed between this signal and the previous one. In this data we observe a curvature in the response indicative of a nonzero optical response time to the changes in the electrical current. This noticeable response time is unexpected for the plasmon drag effect; previous results in the literature exhibit a lack of noticeable response time, even with pulse durations as short as a millisecond [89]. This response time is characterized by a time constant that may be found by fitting the data with equations of the form

$$Ae^{-\alpha(t-t_0)} + B \tag{5.1}$$

$$A\left(1 - e^{-\beta(t-t_0)}\right) + B \tag{5.2}$$

where A and B are constants representing the amplitude and the vertical shift of the data, and t_0 represents the time at which the voltage changes. The results of fitting this equation to the data are shown as the solid lines in Figure 50. The parameters α and β are the inverse of the time constant for the fall and rise of the dark port signal, respectively. The best fit parameters to the data using these equations are displayed

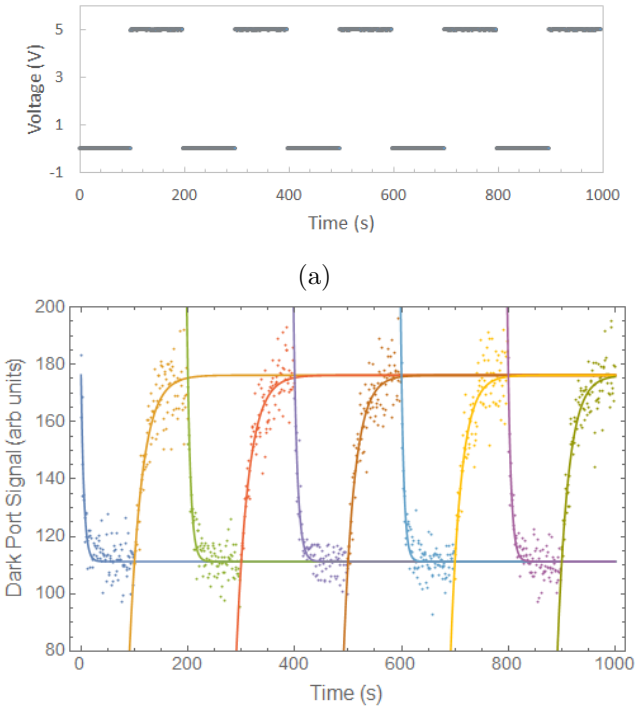

FIGURE 50. Dark port nonreciprocal response at the resonance minimum. (a) Square wave voltage applied by the generator as a function of time. (b) Dark port signal as a function of time. The experimental data points show a modulated response with a frequency matching that of the applied voltage, but with an extended response time. The solid curves represent the exponential fit functions which characterize the response time.

in the Table 3. From this, we observe that the rise in signal happens on a time scale approximately 3–4 times faster than the drop; roughly 22 seconds for the former and 6 seconds for the latter. In revisiting the data of Figure 48c, it appears as though there could be a similar effect present in that data, albeit on a much shorter time scale. In any case, the effect is not nearly as pronounced as seen here with the angle of incidence aligned to the minimum of the resonance. To test whether this behavior is unique to this angle, we move to a second off-resonant angle.

TABLE 3. Decay constants of the dark port signal at the resonance minimum.

Based on the data shown in Figure 50b, α and β display the parameters resulting from a fit to the data of the form of Equations 5.1 and 5.2.

Time Frame	α	β
0-199 s	0.1847	0.0423
200-399 s	0.1606	0.0433
400-599 s	0.1438	0.0479
600-799 s	0.1871	0.0492
800-999 s	0.1657	0.0488

Angle Less Than Resonance Minimum

Figure 51 displays the dark port signal with the interferometer aligned for an incidence on the lower angle side of the resonance, at 43.02°. The voltage signal applied across the silver film remains the same. Here we again see a modulation of the signal at the expected frequency; furthermore, we observe that the extended response time of the signal is persistent, even away from resonance.

Equations 5.1 and 5.2 are applied as a fit to this data, resulting in the parameters shown in Table 4. The magnitude of the values obtained are consistent with those shown above; however, in this scenario the time constant is longer for the drop in the signal, approximately 17 seconds, and shorter when the signal rises again, roughly 7 seconds. What does remain consistent from the previous angle is that the shorter time constant is associated with the disappearance of a current from the silver film while the longer time constant is associated with the appearance of a current. We explored the possibility of this effect arising from an electronics issue, such as an impedance mismatch somewhere in the system, but efforts to track down a potential source were ultimately unsuccessful. The magnitude of the time constant could provide a clue about the source, for example if it were related to an RC time constant located within the system; though here the resistances of interest are of the order of tens of

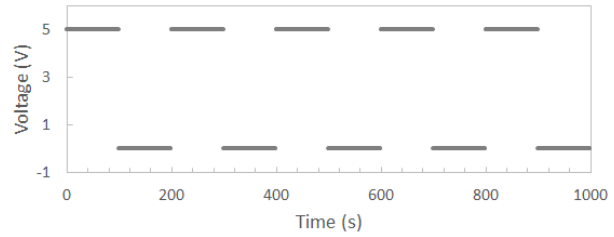

(a)

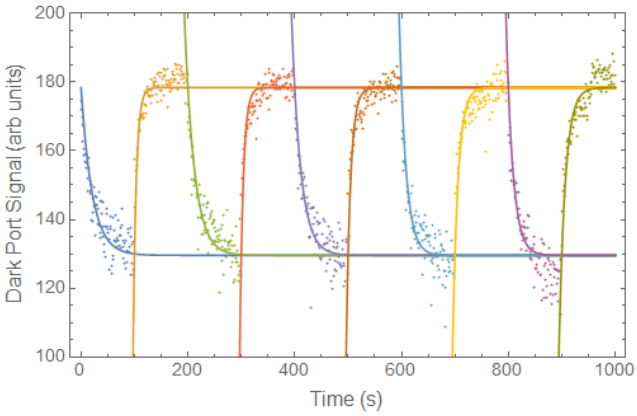

(b)

FIGURE 51. Dark port nonreciprocal response at an angle less than resonance. (a) Square wave voltage applied by the function generator as a function of time. (b) Dark port signal as a function of time. The experimental data points show a modulated response with a frequency matching that of the applied voltage, but with an extended response time. The solid curves represent the exponential fit functions which characterize the response time.

ohms corresponding to a capacitance on the order of a farad, which seems largely implausible.

TABLE 4. Decay constants for an angle less than the resonance minimum.

Based on the data shown in Figure 50b, α and β display the parameters resulting from a fit to the data of the form of Equations 5.1 and 5.2.

Time Frame	α	β
0-199 s	0.0475	0.1698
200-399 s	0.0545	0.1557
400-599 s	0.0591	0.1255
600-799 s	0.0792	0.1012
800-999 s	0.0796	0.0856

Rotation of Film Orientation

In an attempt to determine whether the modulation of the output seen occurs as a result of the plasmon drag effect, we devised an experiment involving a rotation of the silver film orientation. If we posit that the magnitude of the effect is proportional to the scalar product of the drift velocity of the electrons with the momentum vector of the SPPs, then rotating the film such that the direction of current flow in the film is perpendicular to the propagation of SPPs should result in a disappearance of the modulation in the signal. The construction of the brass mass from the prism mount shown in Figure 44 is not compatible with the epoxied leads for this alternate orientation of the sample. Instead, we remove the prism from the mount and position the film as shown in Figure 52. This configuration should give rise to an electron drift velocity with a near vertical orientation while the SPP propagation remains primarily within the horizontal beam plane.

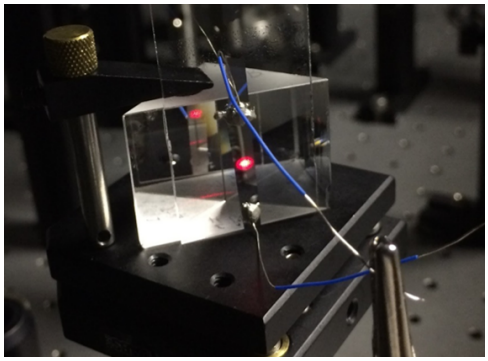

FIGURE 52. Photo of apparatus with film oriented vertically.
In order to generate an electrical current perpendicular to the direction of plasmon propagation, the glass substrate onto which the silver was deposited was rotated on the back of the prism by an angle of 90 degrees.

In this experiment, the interferometer is aligned at the same angle of incidence on the lower angle side of the resonance as before, that being 43.02°. A 10 mHz square wave with 5 volt peak-to-peak amplitude was applied across the silver film by

a function generator. The interferometer output was collected at the dark port and the results are shown in Figure 53a. Despite the orientation of the film such that the electron drift velocity is perpendicular to the momentum vector of the SPPs, the output signal is modulated at the frequency of the voltage input. The amplitude of this modulation is on the same order as similar experiments performed with silver film in the original orientation. This goes against our intuition and calls into question whether or not the observed effects are as a result of plasmon drag. In addition, we continue to observe an exponential growth and decay in the signal response with a timescale on the order of seconds.

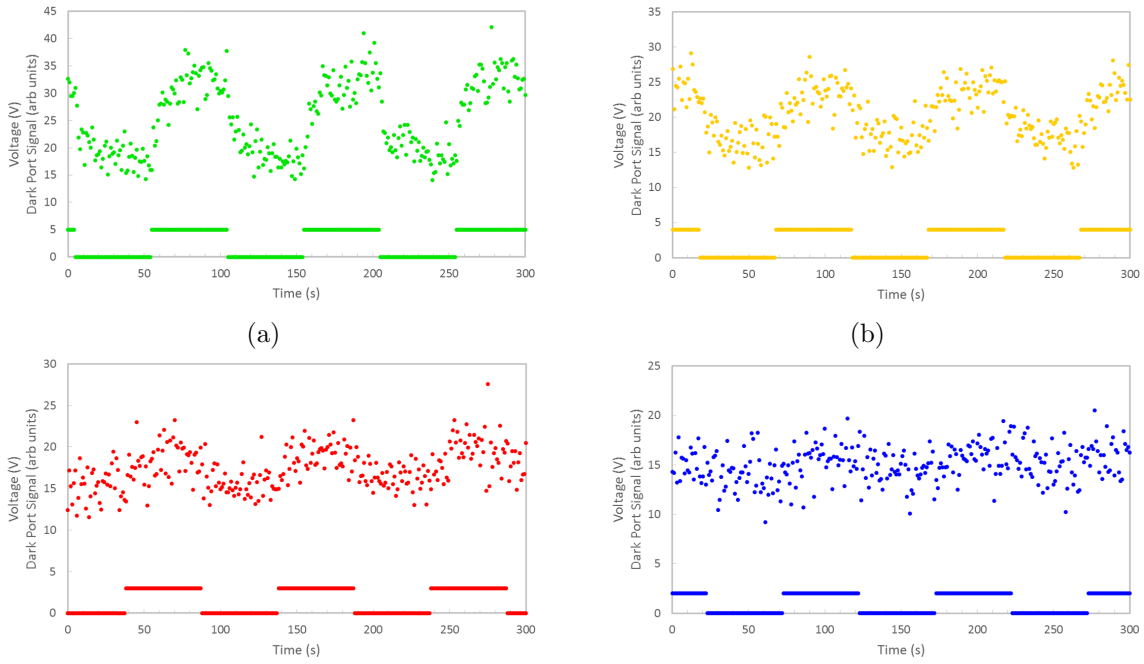

FIGURE 53. Dark port response for varied current with vertically oriented film. (a) Dark port response for a 5 volt peak-to-peak applied voltage. The solid lines represent the voltage applied while the dots display the bright port signal. (b) Dark port intensity and applied voltage for a 4 volt peak-to-peak signal. (c) Dark port intensity and applied voltage for a 3 volt peak-to-peak signal. (d) Dark port intensity and applied voltage for a 2 volt peak-to-peak signal.

The continued observance of a modulated signal matching the frequency of the applied voltage suggests, if not plasmon drag, some other link between the two. To further investigate this link, we vary the amplitude of the square wave potential applied across the silver film at a fixed frequency. Figure 53 shows the results of stepping down the voltage from 5 volts, to 4 volts, then 3 volts, and finally 2 volts. The signal in the regions with no current present in the film remains fairly consistent across all the plots shown. However, by looking at the regions of the plot where the current is present we observe a dark port signal that increases with the voltage applied across the film. An amplitude of this modulation is estimated by averaging the data values in the presence of a voltage and in the absence of a voltage and computing the difference; standard error is propagated through this calculation. These amplitudes are plotted with respect to the amplitude of the applied voltage in Figure 54. The data appears to exhibit an exponential scaling of modulation amplitude with respect to the peak-to-peak voltage supplied by the function generator.

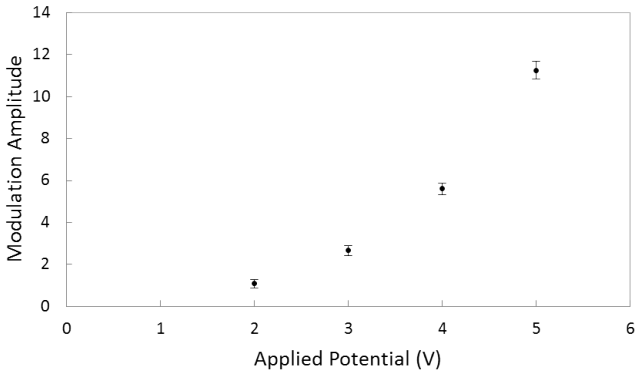

FIGURE 54. Scaling of modulation amplitude.
Calculated from the data displayed in Figure 53, the amplitude of modulation in the dark port signal appears to scale exponentially with the amplitude of the applied voltage. Errors bars represent the standard error, propagated through the calculation of the modulation amplitude.

Analysis

Unfortunately, a modulated response of the dark port output was not measured with sufficient repeatability and predictably to fully characterize the SPP interaction with electrons by use of our model and in terms of a current induced shift in the material parameters of the silver film. We anticipate the amplitude of this modulation to vary with position along the resonance based on the change in the amount of energy that is coupled into the SPP mode for each angle. With measured amplitudes of modulation across a range of angles along the resonance, we could search for some singular combination of parameters, involving the relative permittivity and thickness of the silver film, capable of reproducing this behavior when applied in our model. For any particular angle, we would also expect the amplitude of the modulation to vary with the amplitude of the applied voltage. Collection of a similar set of data for a different applied voltage could provide insight into how any current induced changes to material properties of the film scale with the strength of the current. Initial findings suggest an exponential dependence of the intensity modulation on the amplitude of the applied voltage.

Simultaneous Detection

While the data presented here was collected for only one interferometer output at a time, there were no hindrances encountered in performing these experiments that would preclude the simultaneous detection of both ports. The aim of this work was to provide proof of principle that the bright port could be used for detection of reciprocal perturbations in a resonantly enhanced interferometer and that the dark port response is dominated by sensitivity to nonreciprocal phenomena. Future

experiments could utilize both, in tandem, to further characterize the response of the resonantly enhanced system or in applications as a device for simultaneous detection.

Summary

In this chapter we have presented the assembly, alignment procedures, and experimental results of a resonantly enhanced Sagnac interferometer using surface plasmon polaritons. We first discussed the choice of configuration and the components used in building a balanced interferometer. We then presented the methods used to introduce both reciprocal and nonreciprocal perturbations to the system in the form of ohmic heating and plasmon drag. The first set of experimental results presented pertain to the detection of reciprocal ohmic heating in the bright port supplied via an electrical current in the silver film. A response in the interferometer output was observed which qualitatively matches our model. We examined various sources of quantitative disagreement and suggested paths for improvement. The following section displayed and analyzed data collected from the dark port of the interferometer. A modulation of the dark port signal was observed exhibiting some behavior consistent with plasmon drag and was qualitatively reproducible by use of the theoretical model. An unexpected response time of the signal appear in some of the data and was characterized via exponential fitting procedures, but the ultimate source of this behavior remains unknown. In addition, a dependencies on the direction and magnitude of the electrical current were explored by rotating the orientation of the silver film and varying the voltage applied across it. We observed a modulation of similar amplitude with the rotated orientation and an exponential scaling with voltage. Finally, we reviewed the prospects of the device for future simultaneous detection experiments.

CHAPTER VI

CONCLUSION

This dissertation has sought to convey our exploration into the field of resonantly enhanced Sagnac interferometry using surface plasmon polaritons. We began with a brief overview of both Sagnac interferometry and surface plasmon resonance sensors, covering topics ranging from historical development to modern applications. We calculated the interference equations which give rise to the normalized intensity at the two interferometer outputs. We dealt with the physics of SPPs, from the dispersion relation to coupling schemes for excitation, as well as the resulting surface plasmon resonance. We learned how to engineer the resonance, adjusting the appropriate material parameters to give rise to the desired lineshape. We fabricated samples which displayed this resonance. We then theoretically modeled the outputs and sensitivity of a resonantly enhanced Sagnac interferometer and finally assembled an experimental apparatus and performed initial experiments described by this model.

Through our investigation we found that the inclusion of a resonance within a Sagnac interferometer gives rise to some intriguing results. The dark port behaves mostly as expected for a Sagnac interferometer: rejecting low frequency reciprocal noise and exhibiting sensitivity to nonreciprocal, symmetry breaking perturbations to the system. However, the rapidly changing phase on resonance acts to enhance this signal, improving nonreciprocal sensitivity as compared to the system without resonance. The bright port was also found to respond to these nonreciprocal perturbations; however, the more predominant response is to perturbations that are reciprocal in nature. The intensity modulation imparted on the system by the resonance gives this interferometer, unlike a nonresonant Sagnac, the capacity to

monitor reciprocal drifts within the system. The preferential response to a particular type of perturbation in each of the interferometer outputs gives this device the ability to distinguish between reciprocal and nonreciprocal phenomena in cases where both perturbations may be present, and enables the possibility of simultaneous detection all contained in one device with a single optical source.

This scheme was realized experimentally by applying an electrical current to the silver film supporting SPPs. Optical data collected from either side of the resonance exhibited a response consistent with the reciprocal effect of ohmic heating. The magnitude of the effect suggests a larger temperature change than that which was measured; however, this is not surprising given that the independent measurement of temperature was spatially separated from the optically interrogated region, in a location further away from the source of heat generation. The optical data collected from the dark port exhibited a periodic response with a frequency matching that of the applied electrical signal. However, the nature of the response was not entirely consistent with that expected for the nonreciprocal plasmon drag, and therefore we concede that the origin of the signal may be due, at least in part, to other sources. In addition, the strength of the applied voltage was varied and the modulation amplitude appeared to scale exponentially with this voltage.

Future Directions

There are a number of areas that exist for continued study on this topic. As far as the experimental detection of reciprocal effects in the bright port, the largest obstacle in this work was the physical displacement between the location of the independent measure of temperature and the region probed optically giving rise to a temperature discrepancy. One way to address this could be through a transient heat transfer

analysis to compute a temperature distribution relating the temperature in these two locations. Another possibility could be to prolong the temperature measurements allowing for greater equilibration in hopes to minimize the temperature gradient. A further possibility would be to devise a new configuration or alternate method for independent measure of temperature that is capable of providing a more accurate temperature measurement.

As for the nonreciprocal perturbation detection in the dark port, the results of this dissertation contained some features suggestive of the plasmon drag effect, but other features were not consistent with being produced by this effect. If the interferometer response could be reliably linked to the plasmon drag effect there are some additional experiments to be performed that could further the understanding of the electron-SPP interaction. Two important parameters to vary in these experiments, which were explored in some detail in this work, would be the voltage applied across the silver film and the incidence angle within the prism. The voltage acts as a knob for the current flow, and hence the electron drift velocity, in the metal while the incidence angle controls the amount of energy transferred into the surface mode through the degree of coupling to SPPs. A more complete data set within this parameter space, in combination with the theoretical model to explore these dependencies, could relate the change in optical signal resulting from these affects to modifications in the parameter values that go into the calculations.

Other avenues exist for exploration of the Sagnac interferometer resonantly enhanced by SPR that do not involve introduction of an electrical current within the silver film. For instance, the perturbations could instead be introduced by use of a microfluidic flow channel as the outer dielectric of the SPR configuration. In this scheme, Fresnel-Fizeau drag associated with the moving dielectric would provide the

nonreciprocal perturbation, while the reciprocal phenomena could again be manifest as a temperature or instead, for example, by concentration changes in the fluid.

In addition to the many experimental avenues, another future direction involves modifications to the theoretical model. One specific path of interest would be the inclusion of a metal/insulator stack within the SPR configuration for greater tunability of the resonance lineshape. The use of a Fano resonance to further engineer the lineshape could be optimized for greater sensitivity or improvement of signal to noise. The implementation of perturbations could also be adjusted to include more than just a change in refractive index of the outer dielectric. While this general behavior is able to qualitatively portray much of the system behavior, quantitative description of specific phenomena may involve manipulation of multiple parameters in the system.

Closing Remarks

Throughout my work toward this dissertation, and more broadly during my time at the University of Oregon, I have experienced significant growth in both the academic and personal aspects of my life. Through graduate level coursework, I have accumulated a wealth of knowledge describing the mechanisms through which our physical world operates while simultaneously exploring and expanding the limits of my resolve and understanding. In my experiences teaching and interacting with students, I have cultivated a quiet confidence in clear and effective communication of concepts and affirmed the deeply rooted joy found in positively impacting others toward growth and success. By conducting advanced scientific research, I have exercised and augmented my problem solving capabilities and accessed a formerly untapped level of persistence to move forward, even in the face of adversity. I have

delighted in the thrill of discovery and taken pride in that which I have accomplished. I have also been humbled, time and time again, and faced with the stark realization that I am wholly incapable of fully actualizing the totality of my own lofty expectations. Through it all, I have become a more amicable colleague, a more compassionate friend, a more curious student, a more forgiving husband, a more diligent teacher, a more patient father, a more purposeful scientist, and a more genuine individual. For this I am especially grateful.

REFERENCES CITED

[1] P. Hariharan, "Sagnac or michelson-sagnac interferometer?" Appl. Opt. **14**, 2319–2321 (1975).

[2] G. B. Malykin, "Earlier studies of the sagnac effect," Phys. Usp. **40**, 317–321 (1997).

[3] G. Sagnac, "Sur la preuve de la réalité de l'éther lumineux par l'expérience de l'interférographe tournant," C.R. Acad. Sci. **157**, 1410–1413 (1913).

[4] E. J. Post, "Sagnac effect," Rev. Mod. Phys. **39**, 475–493 (1967).

[5] R. Anderson, H. R. Bilger, and G. E. Stedman, "Sagnac effect: A century of earthrotated interferometers," Am. J. Phys. **62**, 975–985 (1994).

[6] G. B. Malykin, "The Sagnac effect: correct and incorrect explanations," Phys. Usp. **43**, 1229–1252 (2000).

[7] B. Culshaw, "The optical fibre Sagnac interferometer: an overview of its principles and applications," Meas. Sci. Technol. **17**, R1–R16 (2006).

[8] K. Krakenes and K. Blotekjaer, "Comparison of fiber-optic Sagnac and Mach-Zehnder interferometers with respect to thermal processes in the fiber," J. Lightwave Technol. **13**, 682–686 (1995).

[9] J. Hwang, M. Fejer, and W. Moerner, "Scanning interferometric microscopy for the detection of ultrasmall phase shifts in condensed matter," Phys. Rev. A: At. Mol. Opt. Phys. **73**, 021802 (2006).

[10] S. Ezekiel and H. J. Arditty, "Fiber-optic rotation sensors. tutorial review," in "Fiber-Optic Rotation Sensors and Related Technologies," (Springer, Berlin, Heidelberg, 1982), pp. 2–26.

[11] H. C. Lefèvre, "The fiber-optic gyroscope: Challenges to become the ultimate rotation-sensing technology," Opt. Fiber Technol. **19**, 828–832 (2013).

[12] K. U. Schreiber and J. R. Wells, "Invited review article: Large ring lasers for rotation sensing," Rev. Sci. Instrum. **84**, 041101 (2013).

[13] B. Song, H. Zhang, Y. Miao, W. Lin, J. Wu, H. Liu, D. Yan, and B. Liu, "Highly sensitive twist sensor employing sagnac interferometer based on pm-elliptical core fibers," Opt. Express **23**, 15372–15379 (2015).

[14] P. Zu, C. Chiu, G. Wei, W. Siang, and Y. Jin, "Enhancement of the sensitivity of magneto-optical fiber sensor by magnifying the birefringence of magnetic fluid film with loyt-sagnac interferometer," Sens. Actuators, B **191**, 19–23 (2014).

[15] Q. Liu, S. Li, and X. Wang, "Sensing characteristics of a mf-filled photonic crystal fiber sagnac interferometer for magnetic field detecting," Sens. Actuators, B **242**, 949–955 (2017).

[16] P. R. Hoffman and M. G. Kuzyk, "Position determination of an acoustic burst along a sagnac interferometer," J. Lightwave Technol. **22**, 494–498 (2004).

[17] J. Ma, Y. Yu, and W. Jin, "Demodulation of diaphragm based acoustic sensor using Sagnac interferometer with stable phase bias," Opt. Express **23**, 29268–29278 (2015).

[18] L. Shao, Y. Luo, Z. Zhang, X. Zou, B. Luo, W. Pan, and L. Yan, "Sensitivity-enhanced temperature sensor with cascaded fiber optic sagnac interferometers based on vernier-effect," Opt. Commun. **336**, 73–76 (2015).

[19] Y. Cui, P. P. Shum, D. J. J. Hu, G. Wang, G. Humbert, and X. Dinh, "Temperature sensor by using selectively filled photonic crystal fiber sagnac interferometer," IEEE Photonics J. **4**, 1801–1808 (2012).

[20] L. Sun, J. Li, L. Jin, Y. Ran, and B. Guan, "High-birefringence microfiber sagnac interferometer based humidity sensor," Sens. Actuators, B **231**, 696–700 (2016).

[21] S. Gao, L. Sun, J. Li, L. Jin, Y. Ran, Y. Huang, and B. Guan, "High-sensitivity dna biosensor based on microfiber sagnac interferometer," Opt. Express **25**, 13305–13313 (2017).

[22] K. Danzmann and the LISA study team, "LISA: laser interferometer space antenna for gravitational wave measurements," Classical Quantum Gravity **13**, A247–A250 (1996).

[23] D. A. Shaddock, "Operating lisa as a sagnac interferometer," Phys. Rev. D: Part. Fields **69**, 022001 (2004).

[24] U. Leonhardt and P. Piwnicki, "Ultrahigh sensitivity of slow-light gyroscope," Phys. Rev. A: At. Mol. Opt. Phys. **62**, 055801–055801 (2000).

[25] F. Zimmer and M. Fleischhauer, "Sagnac interferometry based on ultraslow polaritons in cold atomic vapors," Phys. Rev. Lett. **92**, 253201 (2004).

[26] W. Nan, Z. Yun-Dong, W. Hao, T. He, Q. Wei, W. Jin-Fang, and Y. Ping, "Precise relative rotation sensing using slow light," Chin. Phys. B **19**, 014216–6 (2010).

[27] V. V. Ivanov, M. A. Novikov, and V. M. Gelikonov, "Measurement of linear velocity using a resonant ring interferometer with a low-coherence light source," Tech. Phys. Lett. **25**, 940–943 (1999).

[28] M. S. Shahriar, G. S. Pati, R. Tripathi, V. Gopal, M. Messall, and K. Salit, "Ultrahigh enhancement in absolute and relative rotation sensing using fast and slow light," Phys. Rev. A: At. Mol. Opt. Phys. **75**, 053807 (2007).

[29] Y. Zhang, H. Tian, X. Zhang, N. Wang, J. Zhang, H. Wu, and P. Yuan, "Experimental evidence of enhanced rotation sensing in a slow-light structure," Opt. Lett. **35**, 691–693 (2010).

[30] A. B. Matsko, A. A. Savchenkov, V. S. Ilchenko, and L. Maleki, "Optical gyroscope with whispering gallery mode optical cavities," Opt. Commun. **233**, 107–112 (2004).

[31] A. Naweed, G. Farca, S. I. Shopova, and A. T. Rosenberger, "Induced transparency and absorption in coupled whispering-gallery microresonators," Phys. Rev. A: At. Mol. Opt. Phys. **71**, 043804 (2005).

[32] J. Scheuer and A. Yariv, "Sagnac effect in coupled-resonator slow-light waveguide structures," Phys. Rev. Lett. **96**, 053901 (2006).

[33] L. Yan, Z. Xiao, X. Guo, and A. Huang, "Circle-coupled resonator waveguide with enhanced sagnac phase-sensitivity for rotation sensing," Appl. Phys. Lett. **95**, 141104 (2009).

[34] J. Homola, S. S. Yee, and G. Gauglitz, "Surface plasmon resonance sensors: review," Sens. Actuators, B **54**, 3–15 (1999).

[35] J. Homola, "Present and future of surface plasmon resonance biosensors," Anal. and Bioanal. Chem. **377**, 528–539 (2003).

[36] C. Nylander, B. Liedberg, and T. Lind, "Gas detection by means of surface plasmon resonance," Sens. Actuators **3**, 79–88 (1982).

[37] B. Liedberg, C. Nylander, and I. Lunström, "Surface plasmon resonance for gas detection and biosensing," Sens. Actuators **4**, 299–304 (1983).

[38] B. Liedberg, C. Nylander, and I. Lunström, "Biosensing with surface plasmon resonance how it all started," Biosens. Bioelectron. **10**, i–ix (1995).

[39] E. Kretschmann and H. Raether, "Radiative Decay of Non Radiative Surface Plasmons Excited by Light," Z. Naturforsch. **23a**, 2135–2136 (1968).

[40] K. S. Johnston, S. R. Karlsen, C. C. Jung, and S. S. Yee, "New analytical technique for characterization of thin films using surface plasmon resonance," Mater. Chem. Phys. **42**, 242–246 (1995).

[41] H. Jussila, H. Yang, N. Granqvist, and Z. Sun, "Surface plasmon resonance for characterization of large-area atomic-layer graphene film," Optica **3**, 151–158 (2016).

[42] K. Matsubara, S. Katawa, and S. Minami, "A Compact Surface Plasmon Resonance Sensor for Measurement of Water in Process," Appl. Spectrosc. **42**, 1375–1379 (1988).

[43] G. Martínez-López, D. Luna-Moreno, D. Monzón-Hernández, and R. Valdivia-Hernández, "Optical method to differentiate tequilas based on angular modulation surface plasmon resonance," Opt. Lasers Eng. **49**, 675–679 (2011).

[44] L. J. Davis and M. Deutsch, "Surface plasmon based thermo-optic and temperature sensor for microfluidic thermometry," Rev. Sci. Instrum. **81**, 114905 (2010).

[45] A. Paliwal, A. Sharma, M. Tomar, and V. Gupta, "Room temperature detection of NO_2 gas using optical sensor based on surface plasmon resonance technique," Sens. Actuators, B **216**, 497–503 (2015).

[46] J. Homola, "Surface plasmon resonance sensors for detection of chemical and biological species," Chem. Rev. **108**, 462–493 (2008).

[47] S. Zeng, D. Baillargeat, H. Ho, and K. Yong, "Nanomaterials enhanced surface plasmon resonance for biological and chemical sensing applications," Chem. Soc. Rev. **43**, 34263452 (2014).

[48] V. N. Konopsky and E. V. Alieva, "Photonic crystal surface waves for optical biosensors," Anal. Chem. **79**, 4729–4735 (2007).

[49] A. A. Rifat, G. A. Mahdiraji, Y. M. Sua, Y. G. Shee, R. Ahmed, D. M. Chow, and F. R. M. Adikan, "Surface plasmon resonance photonic crystal fiber biosensor: A practical sensing approach," IEEE Photonics Technol. Lett. **27**, 1628–1631 (2015).

[50] C. Liu, W. Su, Q. Liu, X. Lu, F. Wang, T. Sun, and P. K. Chu, "Symmetrical dual d-shape photonic crystal fibers for surface plasmon resonance sensing," Opt. Express **26**, 9039–9049 (2018).

[51] A. K. Sharma, R. Jha, and B. D. Gupta, "Fiber-optic sensors based on surface plasmon resonance: A comprehensive review," IEEE Sens. J. **7**, 1118–1129 (2007).

[52] J. A. Kim, T. Hwang, S. R. Dugasani, R. Amin, A. Kulkarni, S. H. Park, and T. Kim, "Graphene based fiber optic surface plasmon resonance for bio-chemical sensor applications," Sens. Actuators, B **187**, 426–433 (2013).

[53] J. Zhao, S. Cao, C. Liao, Y. Wang, G. Wang, X. Xu, C. Fu, G. Xu, J. Lian, and Y. Wang, "Surface plasmon resonance refractive sensor based on silver-coated side-polished fiber," Sens. Actuators, B **230**, 206–211 (2016).

[54] K. Bremer and B. Roth, "Fibre optic surface plasmon resonance sensor system designed for smartphones," Opt. Express **23**, 17179–17184 (2015).

[55] Y. Liu, Q. Liu, S. Chen, F. Cheng, H. Wang, and W. Peng, "Surface plasmon resonance biosensor based on smart phone platforms," Sci. Rep. **5**, 12864 (2015).

[56] M. Piliarik and J. Homola, "Surface plasmon resonance (spr) sensors: approaching their limits?" Opt. Express **17**, 16505–16517 (2009).

[57] A. N. Grigorenko, P. I. Nikitin, and A. V. Kabashin, "Phase jumps and interferometric surface plasmon resonance imaging," Appl. Phys. Lett. **75**, 3917–3919 (1999).

[58] S. Y. Wu, H. P. Ho, W. C. Law, C. Lin, and S. K. Kong, "Highly sensitive differential phase-sensitive surface plasmon resonance biosensor based on the mach–zehnder configuration," Opt. Lett. **29**, 2378–2380 (2004).

[59] A. V. Kabashin, S. Patskovsky, and A. N. Grigorenko, "Phase and amplitude sensitivities in surface plasmon resonance bio and chemical sensing," Opt. Express **17**, 21191 (2009).

[60] B. Ran and S. G. Lipson, "Comparison between sensitivities of phase and intensity detection in surface plasmon resonance," Opt. express **14**, 5641–50 (2006).

[61] A. Lahav, M. Auslender, and I. Abdulhalim, "Sensitivity enhancement of guided-wave surface-plasmon resonance sensors," Opt. Lett. **33**, 2539–2541 (2008).

[62] H. Grotewohl and M. Deutsch, "Tunable geometric fano resonances in a metal/insulator stack," J. Opt. **17**, 085003 (2015).

[63] S. Hayashi, D. V. Nesterenko, and Z. Sekkat, "Waveguide-coupled surface plasmon resonance sensor structures: Fano lineshape engineering for ultrahigh-resolution sensing," J. Phys. D: Appl. Phys. **48**, 325303 (2015).

[64] H. Grotewohl, B. Hake, and M. Deutsch, "Intensity and phase sensitivities in metal/dielectric thin film systems exhibiting the coupling of surface plasmon and waveguide modes," Appl. Opt. **55**, 8564–8570 (2016).

[65] E. D. Palik, *Handbook of Optical Constants of Solids* (Academic Press, 1985).

[66] H. E. Bennett, R. L. Peck, D. K. Burge, and J. M. Bennett, "Formation and growth of tarnish on evaporated silver films," J. Appl. Phys. **40**, 3351–3360 (1969).

[67] A. A. Schmidt, J. Offermann, and R. Anton, "The role of neutral oxygen radicals in the oxidation of ag films," Thin Solid Films **281**, 105–107 (1996).

[68] H. Sahm, C. Charton, and R. Thielsch, "Oxidation behaviour of thin silver films deposited on plastic web characterized by spectroscopic ellipsometry (se)," Thin Solid Films **455**, 819–823 (2004).

[69] T. T. Ehler and L. J. Noe, "Surface plasmon studies of thin silver/gold bimetallic films," Langmuir **11**, 4177–4179 (1995).

[70] S. A. Zynio, A. V. Samoylov, E. R. Surovtseva, V. Mirsky, and Y. M. Shirshov, "Bimetallic layers increase sensitivity of affinity sensors based on surface plasmon resonance," Sensors **2**, 62–70 (2002).

[71] X.-M. Zhu, P.-H. Lin, P. Ao, and L. B. Sorensen, "Surface treatment for surface plasmon resonance biosensors," Sens. Actuators, B **84**, 106–112 (2002).

[72] W. L. Barnes, "Surface plasmon–polariton length scales: a route to sub-wavelength optics," J. Opt. A: Pure Appl. Opt. **8**, S87–S93 (2006).

[73] H. Raether, "Surface Plasmons on Smooth and Rough Surfaces and on Gratings," Springer Tracts in Modern Physics **111** (1988).

[74] S. Herminghaus, M. Klopfleisch, and H. J. Schmidt, "Attenuated total reflectance as a quantum interference phenomenon," Opt. Lett. **19**, 293–295 (1994).

[75] K. M. McPeak, S. V. Jayanti, S. J. P. Kress, S. Meyer, S. Iotti, A. Rossinelli, and D. J. Norris, "Plasmonic films can easily be better: Rules and recipes," ACS Photonics **2**, 326–333 (2015).

[76] P. Yeh, *Optical Waves in Layered Media* (Wiley, 2004).

[77] P. B. Johnson and R. W. Christy, "Optical constants of the noble metals," Phys. Rev. B: Condens. Matter **6**, 4370–4379 (1972).

[78] W. M. Macek, J. R. Schneider, and R. M. Salamon, "Measurement of Fresnel Drag with the Ring Laser," J. Appl. Phys. **35**, 2556 (1964).

[79] A. Tselikov and J. Blake, "Sagnac-interferometer-based fresnel flow probe," Appl. Opt. **37**, 6690–6694 (1998).

[80] A. J. Fresnel, "Lettre d'augustin fresnel à françois arago sur l'influence du mouvement terrestre dans quelques phénomènes d'optique," Ann. Chim. Phys. **9**, 57–66 (1818).

[81] H. Fizeau, "Sur les hypothèses relatives à l'éther lumineux, et sur une expérience qui parâit démontrer que le mouvement des corps change la vitesse à laquelle la lumière se propage dans leur intérieur," C.R. Hebd. Seances Acad. Sci. **33**, 349–355 (1851).

[82] J. H. Park, P. Ambwani, M. Manno, N. C. Lindquist, P. Nagpal, S. Oh, C. Leighton, and D. J. Norris, "Single-crystalline silver films for plasmonics," Adv. Mater. **24**, 3988–3992 (2012).

[83] Y. Wu, C. Zhang, N. M. Estakhri, Y. Zhao, J. Kim, M. Zhang, X. Liu, G. K. Pribil, A. Alù, C. Shih, and X. Li, "Intrinsic optical properties and enhanced plasmonic response of epitaxial silver," Adv. Mater. **26**, 6106–6110 (2014).

[84] M. Durach and N. Noginova, "On the nature of the plasmon drag effect," Phys. Rev. B: Condens. Matter **93**, 161406 (2016).

[85] K. P. Birch and M. J. Downs, "An updated edlén equation for the refractive index of air," Metrologia **30**, 155–162 (1993).

[86] A. S. Vengurlekar and T. Ishihara, "Surface plasmon enhanced photon drag in metal films," Appl. Phys. Lett. **87**, 091118 (2005).

[87] H. Kurosawa and T. Ishihara, "Surface plasmon drag effect in a dielectrically modulated metallic thin film," Opt. Express **20**, 1561–1574 (2012).

[88] N. Noginova, V. Rono, F. J. Bezares, and J. D. Caldwell, "Plasmon drag effect in metal nanostructures," New J. Phys. **15**, 113061 (2013).

[89] N. Noginova, A. V. Yakim, J. Soimo, L. Gu, and M. A. Noginov, "Light-to-current and current-to-light coupling in plasmonic systems," Phys. Rev. B: Condens. Matter **84**, 035447 (2011).

[90] M. L. Brongersma and V. M. Shalaev, "The case for plasmonics," Science **328**, 440–441 (2010).

[91] T. J. Davis, D. E. Gómez, and A. Roberts, "Plasmonic circuits for manipulating optical information," Nanophotonics **6**, 543–559 (2016).